UNIVERSITY OF OTTAWA

Integration of High Efficiency Solar Cells on Carriers for Concentrating System Applications

---

by

Simon Ka Ming Chow

Thesis submitted to the Faculty of Graduate and Postdoctoral Studies in partial fulfillment of the requirements for the M.Sc degree in Systems Science

June 2011

Systems Science Program

School of Information Technology and Engineering

University of Ottawa

Abstract

High efficiency multi-junction (MJ) solar cells were packaged onto receiver systems. The efficiency change of concentrator cells under continuous high intensity illumination was done. Also, assessment of the receiver design on the overall performance of a Fresnel-type concentration system was investigated.

We present on receiver designs including simulation results of their three-dimensional thermal operation and experimental results of tested packaged receivers to understand their efficiency in real world operation. Thermal measurements from solar simulators were obtained and used to calibrate the model in simulations. The best tested efficiency of 36.5% is obtained on a sample A receiver under 260 suns concentration by the XT-30 solar simulator and the corresponding cell operating temperature is ~30.5°C. The optimum copper thickness of a 5 cm by 5 cm simulated alumina receiver design was determined to be 6 mm and the corresponding cell temperature under 1000 suns concentration is ~36°C during operation.

Statement of Originality

Except where stated otherwise, the results presented in this thesis were obtained by the author during the period of his M. Sc research project under the supervision of Dr. Karin Hinzer. They are to the best of his knowledge original.

This project was developed through the SUNRISE project (Semiconductor Using Nanostructures for Record Increases in Solar-cell Efficiency). The ultimate goal of this project was to enhance the current state of the art for triple junction solar cells. This was achieved through simulation, characterization and integration of these high efficiency cells into solar concentrators.

The simulation used in Figure 23 was performed by Aaron Muron. Figure 33 was provided by Olivier Theriault, PhD student, University of Ottawa.

- The above work has led to the following papers and publications:

1. S. Chow, C. E. Valdivia, J. F. Wheeldon, R. Ares, O. J. Arenas, V. Aimez, D. McMeekin, S. Fafard and K. Hinzer, "Thermal test and simulation of alumina receiver with high efficiency multi-junction solar cell for concentrator systems", *SPIE Proceedings of Photonics North,* vol. 7750, pp. 775035-7750035-8, 2010.

2. S. Chow, "COMSOL Multiphysis Design and Thermal Simulation of a Chip on Carrier Solar Receiver", *CMC Microsystems, Application Note*, CMC-00200-01385, Dec., 2010.

3. O. Arenas, S. Chow, J. F. Wheeldon, L.M. Collin, C. E Valdivia, K. Hinzer, L. Frechette, V. Aimez, R. Ares, "Comparative thermal analysis of solar cells mounted

on Ceramic and metallic carriers and their optimization for CPV applications", *35th Photovoltaic Specialist Conference,* Proc IEEE, Honolulu, USA, pp. 2998 – 3002, June 2010.

4. C. E. Valdivia, S. Chow, S. Fafard, O. Thériault, M. Yandt, J. F. Wheeldon, A. J. Springthorpe, D. McMeekin, D. Masson, B. Riel, V. Aimez, R. Arès, J. Cook, T. J. Hall, F. Shepherd, K. Hinzer, "Measurement of high efficiency 1 cm^2 AlGaInP/InGaAs/Ge solar cells with embedded InAs quantum dots at up to 1000 suns continuous concentration*", 35th Photovoltaic Specialists Conference 2010*, Proc. IEEE, Honolulu, USA, pp. 1253, June 2010.

5. O. Arenas, V. Aimez, S. Chow, C. E. Valdivia, J. E. Wheeldon, K. Hinzer, A. Turula, R. Arès, "Advances in cell carriers for CPV applications", *International Conference on Concentrating Photovoltaic Systems (CPV-6), Proc. AIP*, vol. 1277, pp. 66-69, Freiburg, Germany, Apr 2010.

6. J. F. Wheeldon, C. E. Valdivia, S. Chow, O. Theriault, A. Walker, M. Yandt, D. Masson, B. Riel, D. McMeekin, N. Puetz, S. G. Wallace, T. J. Hall, S. Fafard, K. Hinzer, "Effiency measurements of GaInP/InGaAs/Ge quantum dot enchanced solar cells at up to 1000-suns under flash and continuous concentration", *to be appear in International Conference on Concentrating Photovoltaic Systems (CPV-7)*, 2011.

7. O. Arenas, L.M. Collin, S. Chow, F. Proulx, K. Hinzer, V. Aimez, L. Frechette, R. Arès, "High performance CPV carrier development using temperature sensors", *to be appear in International Conference on Concentrating Photovoltaic Systems (CPV-7)*, 2011.

8. O. Arenas, L. M. Collin, V. Aimez, S. Chow, C. E. Valdivia, J. F. Wheeldon, K. Hinzer, R. Arès, "Investigation of electrical and thermal characteristics of cell carriers for high concentration photovoltaic applications", *Photonics North 2010, Proc. SPIE*, Niagara Falls, Canada, Jun 2010.

Acknowledgements

I would like to sincerely thank my supervisor, Dr. Karin Hinzer, for her unwavering guidance and support during my studies. She has given me a large degree of freedom while maintaining the integrity of my research project. I would also like to thank Dr. Chris Valdivia and Dr. Jeff Wheeldon for their supervision and academic advice, and SUNLab members for their moral support.

Last but not least, I am grateful to my family members, especially mom and dad for my creation and a lifetime of unconditional love.

"Success is not final, failure is not fatal: It is the courage to continue that counts."

- *Winston Churchill*

Table of Contents

List of Figures

Number *Page*

List of Tables

Number *Page*

List of Abbreviations

AM: Air mass
CPV: Concentrator photovoltaic
DNI: Direct normal irradiance
DUT: Device under test
FF: Fill Factor
IV: Current-Voltage
MJ: Multi-junction
PV: Photovoltaic
TEC: Thermal electric cooler

List of Symbols

A: area (m^2)
A_b: Area of heat sink (m^2)
a, b: Half-lengths of source area (m)
$\propto_i$: aspheric coefficient
C: Curvature at the vertex (unit)
c: Speed of light (m/s)
D: Diameter of the lens (m)
E_λ: Energy of a photon (eV)
Eg: Energy gap (eV)
e: Emissivity (%)
FF: Fill factor (%)
H: Power density (W/m^3)
h: Heat transfer coefficient ($W/(m^2*K)$
h_g: Ground height (m)
$\hbar$: Plank's constant (J*s)
η: Efficiency of a solar cell (%)
I_{sc}: Short circuit current (A)
I_{mp}: Maximum power current (A)
i, j: Half-lengths of flux channel (m)
k: Boltzmann's constant (J/K)
k_c: conic constant
k_i: Thermal conductivity of i^{th} layer (W/(m*K))
L_i: Thickness for i^{th} layer (m)
l_s: Length of the shadow
λ: Wavelength (m)
m, n: Summation indices (unit)
n: Electron concentration (cm^{-3})
η: Efficiency (%)
P_{in}: Incident light power (W)
p: Holes concentration (cm^{-3})
Φ: Photon flux (photons/(area*m))
Q: Thermal energy (W)
R_{total}: Total thermal resistance (K*m/W)
R_{1D}: One dimensional thermal resistance (K*m/W)
$R_{spreading}$: Lateral spreading resistance (K*m/W)
r: radial distance (m)
σ: Stefan-Boltzmann's constant ($J/(s*m^2K^4)$)
T: Temperature (K)
T_1: Temperature at the top of an element (K)
T_2: Temperature at the bottom of element (K)
T_{env}: Ambient temperature (K)
t: time (s)

u^2: Unit area (m^2)
V_{oc}: Open circuit voltage (V)
V_{mp}: Maximum power voltage (V)
x: Cartesian horizontal coordinates (m)
y: Cartesian vertical coordinates (m)
Z: Height of the aspheric surface (m)

Chapter 1 Introduction

Solar energy is one of the technologies leading the way to a new and exciting future of renewable energy sources. Central to solar energy is the photovoltaic (PV) cell that converts energy from the sun into electrical energy and it can be harnessed by any number of space and terrestrial applications. The current state-of-the-art in high-efficiency PV cells is the triple-junction, III-V semiconductor solar cell. The most common type of solar cell is the silicon solar cell, which utilizes a relatively limited range of the spectrum from solar radiation. In contrast, MJ solar cells capture a larger range of the solar spectrum, (Figure 1 and Figure 2) but require more expensive materials and fabrication procedures. Concentrating optics allows light collected over a large area to be focused onto a small PV cell, providing significant material and fabrication cost savings.

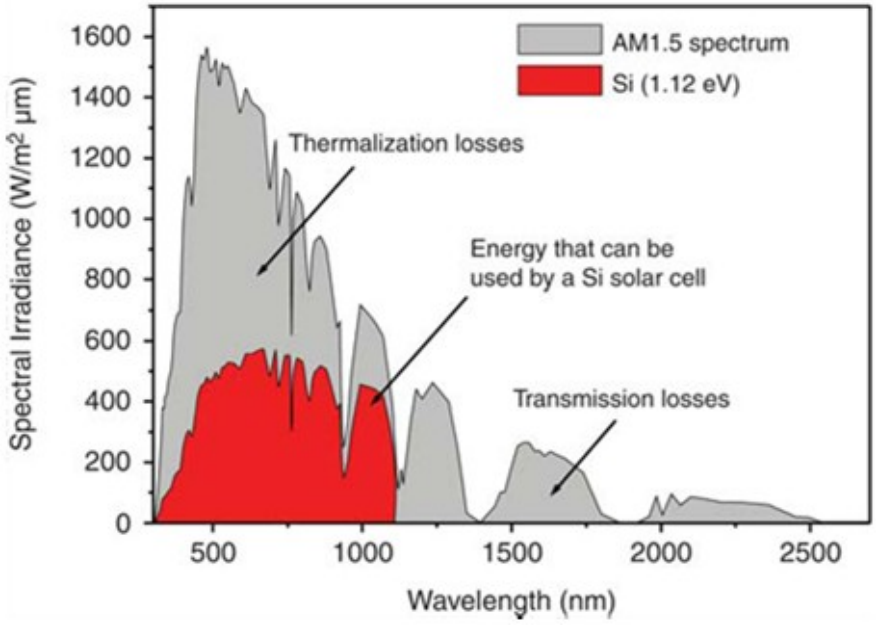

Figure 1 The spectral irradiance as a function of wavelength of a Si solar cells [1].

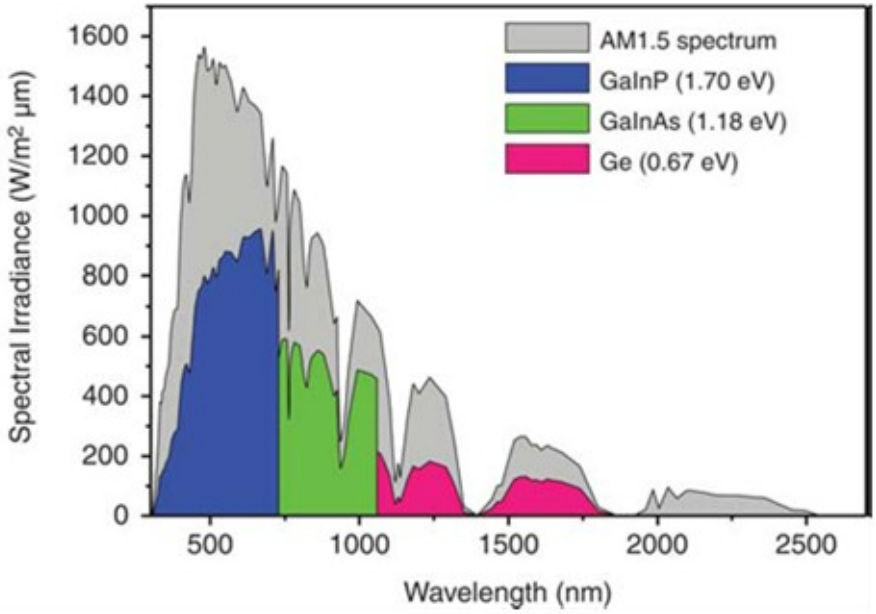

Figure 2 The spectral irradiance as a function of wavelength of triple junction $Ga_{0.35}In_{0.65}P/Ga_{0.83}In_{0.17}As$/Ge solar cells [1].

Power generation using concentrated sunlight can be dated back to 1866 when Auguste Mouchout used a parabolic trough to produce steam from the first solar steam engine [2]. Studies conducted by the Department of Energy (DOE), Electrical Power Research Institute (EPRI) and others [3], [4], [5] concluded that focusing light onto solar cells using optical devices like mirrors or lenses reduces the overhead of the expensive solar cells and increases the cell efficiency. However, concentrating photovoltaic (CPV) have low acceptance angles and require direct normal irradiance (DNI) for power generation. This condition is satisfied by the introduction of a two-axis tracker to follow the sun across the sky.

Development of concentrator technology started effectively in 1976 at the Sandia National Laboratories with 1 kW peak CPV arrays named Sandia I and Sandia II [6]. The world's first concentration plant built and deployed by Martin Marietta using Sandia National Laboratory technologies in Saudi Arabia, is a 350 kWp SOLERAS project shown in Figure 3. The concentration plant employed 20% efficient Si concentrator cells with 40X concentration. Concentration is the spatial focus of light onto a spot using either refractive

lenses or reflective dishes. Direct solar radiation on a solar cell is around 1 kW/m^2 at sea level.

Figure 3 The 350kWp SOLERAS project in Saudi Arabia [4].

The III-V semiconductor single junction concentrator cells are known to operate reliably up to 5800X concentration under forced liquid cooling [7]. Currently available commercial concentration ratios are typically around 500X with the potential to go to several thousand times concentration in the future. Semiconductor device performance is typically temperature-dependent and increasing the light concentration on the solar cell results in a rise in temperature. Inevitably, there is a performance impact on the solar cell with higher temperature. Cell efficiencies decrease as temperatures increase, and higher temperatures also threaten the long-term reliability of PV cells. Therefore, concentrator cells must be kept cool, either by conduction (passive cooling) or by active convection (circulating coolant).

Past research on CPV technology has focused largely on the optics and the PV cells. The remaining barriers are the thermal and electrical management when packaging solar cells which requires more effort.

This thesis aims to understand all elements of solar cell integration and to ensure the best packaging possible for a triple junction solar cell in a concentrator. Triple junction solar cells absorb a wide range of the solar spectrum. Material and fabrication costs used to be the main barriers to world wide deployment of CPV systems containing MJ cells but these technologies have now matured and lowering the cost of other parts of the system must be performed. Using a concentrator to focus a large area of light onto the solar cell significantly lowers the total cost. The triple junction solar cell is rather small, typically 1 cm^2 or less, and must be packaged on a receiver before mounting the receiver on a concentrator. Packaging involves thermal, electrical and material investigation of the receiver in order to optimize the PV module efficiency.

The objectives of the thesis are:

- To demonstrate a detailed understanding of the thermal management elements and electrical transport components within a concentrated MJ solar cell receiver.
- To understand indoor solar simulators, their setup and concentration calibrations.
- To test and analyse packaged solar cell receivers that have various thermal and electrical properties under concentrated sunlight.
- To provide thermal simulations of the various receivers using numerical methods. Results will be compared to the experimental data.
- To provide a solar concentrator model by state of the art software for module efficiency.

The expected outcome is to discover the optimal thermal receiver design through numerical simulation calibrated by experimental result of the designed receiver. Experimental efficiencies obtained on packaged solar receivers can be referenced for future research purposes.

Chapter 2 presents the necessary background knowledge regarding the sun and its characteristic, III-V semiconductors, the *p-n* junction and the behaviour and parameters of a solar cell. In addition, the concentrator system and its components including optics,

homogenizer and receiver are described and discussed. Finally the thermal behaviour of a receiver can be approximated and explained by an analytical solution used in microchip packaging technology.

Chapter 3 illustrates the experimental setup, equipment and methods used for characterizing solar cells and receivers. The lower power continuous solar simulator, manufactured by Oriel, is briefly described and the higher power, XT-20 and XT-30, solar simulators are explained in detail for both electrical and fluid connections. The temporal stability of the lamp, emission spectrum and illumination mask are also discussed. Finally, two concentration calibration methods used for the experiments are introduced and explained.

Chapter 4 presents the experimental results obtained from the characterisation of the MJ solar cells and the solar receivers. Three different types of packaged receiver, using research-grade multi-junction solar cells, were characterised under pulsed and continuous solar concentrators. Photovoltaic efficiencies, open circuit voltages and solar cell temperatures of the tested devices using both calibration methods are detailed and discussed. The surface temperatures of the receivers were also investigated by probing and the results are compared between each receiver. The chapter finishes with a discussion of devices that failed during testing and the common failure mechanisms that were observed.

Chapter 5 presents the thermal simulations, using COMSOL Multiphysics and MATLAB, of the three packaged receivers tested in Chapter 4. The COMSOL simulation models were calibrated using experimental results from Chapter 4. Simulated results of cell temperatures and receiver surface heating are presented and discussed. A general model of the receiver cell temperature with thermal transfer coefficient and concentration variation is developed and explained. In addition, a three dimensional temperature model is presented, which allows for various receiver sizes and conductive layer thicknesses. Finally, a

convergence study based on the COMSOL meshing and elements approximation is investigated.

Chapter 6 presents the modelling of a typical Fresnel type solar concentrator by ZEMAX. Two emitting spectrums, uniform and weighted, were investigated within the concentrator model. The spatial distribution imaging results of each sub cell from a concentrated spectrum and concentrator optical efficiencies are presented and compared.

Chapter 7 presents the overall general conclusions of this thesis and discussions on possible future work.

Chapter 2 Background

2.1. Introduction

This chapter begins by presenting the fundamental properties of solar radiation, the emission spectrum from the sun and the absorption spectrum on the Earth. The properties of III-V semiconductor devices and their *p-n* junction characteristics are described. The characteristics of a solar cell and its operation are then reviewed. The later part of the chapter presents the concentrator optic and focuses on the Fresnel optic design. The homogenizer and the receiver inside a solar concentrator are also introduced and discussed in terms of their electrical performance, geometry design and material of construction. The last part of the chapter investigates, analytically, the thermal properties of a receiver in the context of high concentration.

2.2. Properties of light

Light is a synonym for electromagnetic radiation and sunlight refers to the total range of electromagnetic radiation emitted by the sun. Visible light, which covers the wavelength range from 390 to 750 nm, is a small subset of the sunlight spectrum which is a subset of the electromagnetic spectrum. Electromagnetic radiation is composed of elementary particles name photons. Photons are tiny packets of light that possess both wave and particle properties.

Photons are not electrically charged and photon energies are determined by the properties of the photon, which are determined by the properties of the source. Photon energy, E_λ, can be determined by:

$$E_\lambda = \frac{\hbar \cdot c}{\lambda} \qquad 2\text{-}1$$

where h is the Plank's constant, c is the speed of light and λ is the wavelength.

There is an inverse proportional relationship between the energy and the wavelength of a photon. The photon flux ϕ is defined as the number of photons passing through a unit area per second:

$$\phi = \frac{\#\ of\ photons}{t \cdot u^2} \qquad 2\text{-}2$$

where t is time in seconds and u^2 is the unit area in meter squares.

The photon flux does not contain details regarding the wavelength or energy of each individual photon. If the wavelength is not specified then the flux could be composed of various wavelengths. The power density H can be obtained from a wavelength specific photon flux according to:

$$H = \phi \frac{\hbar \cdot c}{\lambda} \qquad 2\text{-}3$$

where $\hbar$ is Plank's constant, c is the speed of light and ϕ is the photon flux.

2.3. Solar radiation

Our sun is a class G star. It is composed of mainly hydrogen and helium. The core temperature is estimated at 15.7 million degrees Kelvin and is constantly performing nuclear fusion which converts hydrogen to helium [8]. The surface temperature of the sun is approximately 5780K. The Stefan-Boltzmann law dictates that for a given temperature T, a blackbody radiates energy proportional to the fourth power of its temperature T. The result is given by:

$$Q = e\sigma A T^4 \mathrm{t} \qquad 2\text{-}4$$

where Q is the thermal energy emitted by the body; A is the surface area of the radiating body; T is the temperature of the body; t is the time; e is the emissivity of the body (ranging from 0 to 1); σ is the Stefan-Boltzmann constant and is given by:

$$\sigma = 5.67 * 10^{-8} \left[\frac{\mathrm{J}}{\mathrm{s\ m^2 K^4}}\right] \quad 2\text{-}5$$

Plank's radiation law gives the energy distribution over emitted wavelengths of a radiating body. The energy distribution per unit area per unit time per wavelength is:

$$\frac{Q}{At\Delta\lambda} = \frac{2\pi\hbar c^2}{\lambda^5}\left(\frac{1}{e^{\hbar c/\lambda kT} - 1}\right) \quad 2\text{-}6$$

where c is the speed of light; λ is the wavelength; k is the Boltzmann constant; $\hbar$ is the Plank's constant.

The intensity of a blackbody's radiation changes with respect to different wavelengths for a fixed radiating temperature. The intensity of the blackbody radiation for different temperatures is shown in Figure 4. For a specific temperature of a black body there is a wavelength (λ_{max}) which has the highest intensity. λ_{max} is given by the Wien displacement law:

$$\lambda_{max} T = 2.898 * 10^{-3}\ (m * K) \quad 2\text{-}7$$

For the sun's blackbody temperature of 5780K, λ_{max} is 501 nm.

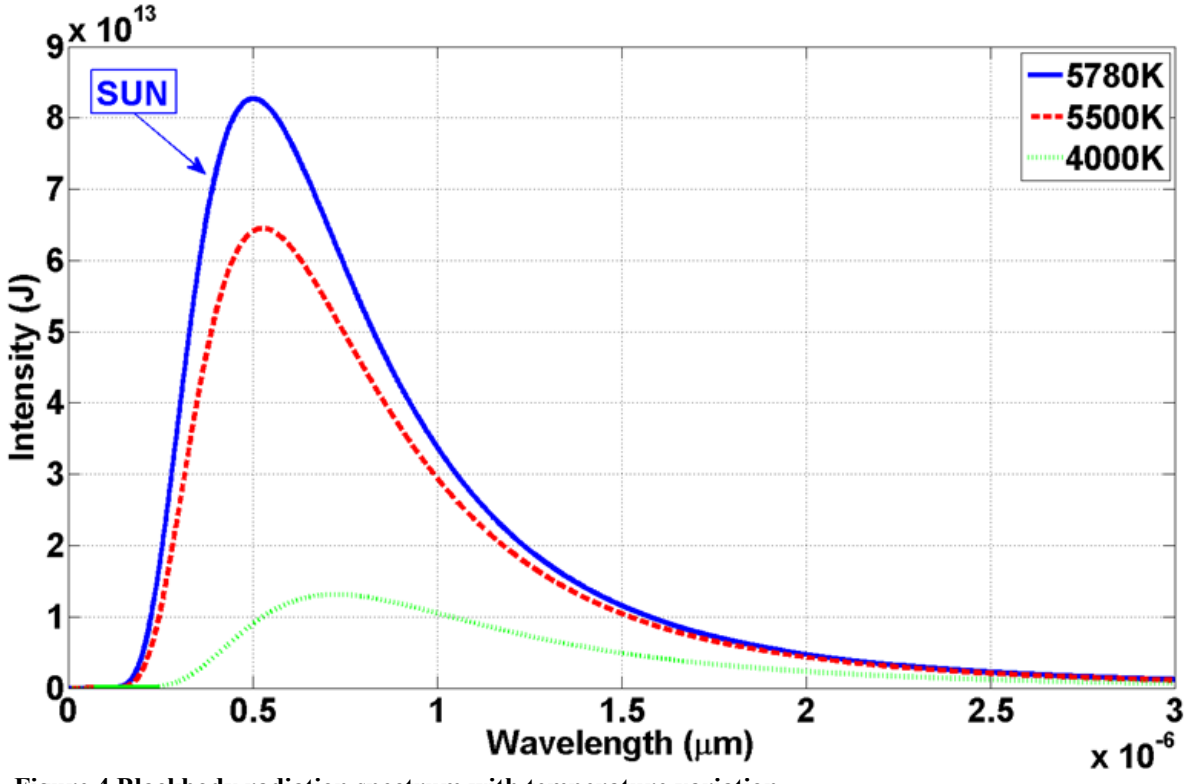

Figure 4 Blackbody radiation spectrum with temperature variation.

2.4. Atmosphere effects

The solar radiation incident on the Earth's atmosphere is constant but radiation on the Earth's surface varies due to the attenuating effects of the Earth's atmospheric effects include absorption, scattering and reflection. They ultimately alter and decrease the solar irradiance reaching the Earth's surface. Only 70% of the solar radiation reaches the Earth's sea level since 18% is absorbed by the atmosphere, 5% is scattered toward space and 7% is scattered by the Earth's atmosphere [9].

2.5. Air mass

The Air Mass (AM) represents the ratio of atmosphere that light travels from celestial to Earth relative to its path length. As light pass through the atmosphere composed with air and dust, the intensity is attenuated by scattering and absorption. The AM refers to the depth of the atmosphere that light has passed through. The AM number is given by:

$$Air\ Mass = \frac{1}{cos\theta} \qquad 2\text{-}8$$

where θ is the angle of incidence from zenith angle.

The spectrum, where the sun light is normal to the surface (θ = 0) and at sea level, is referred to as AM1.0. A special case for extraterrestrial application is Air Mass zero (AM 0) where the radiation spectrum is measured above the Earth's atmosphere [10]. The standard spectrum used for terrestrial characterization is AM 1.5 where θ = 48.19°. The AM1.5G spectrum with "G" stands for global and its spectrum includes direct and diffuse light while the AM1.5D (direct) spectrum, contains only direct light. The total irradiance of AM0, AM1.5G, AM1.5D is 1.353 kW/m^2, 1 kW/m^2 and 850 W/m^2 [11],[12]. Atmospheric spectra for various distances are shown in Figure 5.

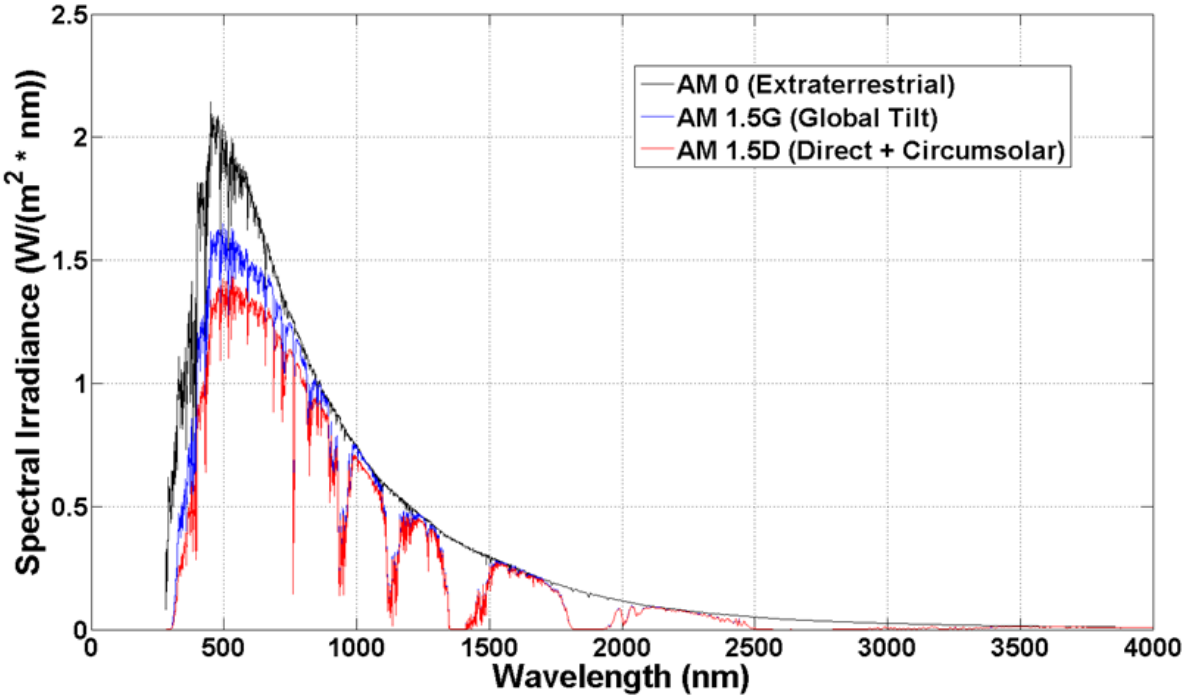

Figure 5 Irradiance spectrum plot with respect to various AM solar radiations [11], [12].

AM can also be easily estimated at any location from the shadow of a vertical pole given the following formula:

$$AM = \sqrt{1 + \left(\frac{l_s}{h_g}\right)^2} \qquad 2\text{-}9$$

where l_s is the length of the shadow cast by a pole normal to the ground with height of h_g. The above equation assumes the atmosphere is flat but in reality both the atmosphere layer and the Earth is curved. The AM does not exactly predict the atmospheric path length when the sun is close to the horizon.

2.6. Semiconductor materials (III-V)

Semiconductors are made up of atoms bonded together in a lattice structure where atoms are arranged in a periodic fashion [13]. Crystal materials must normally be lattice matched and have the same type of crystalline orientation [14]. Materials for semiconductors can be found within group II to group VI of the element table. Semiconductor materials can be a combination of compound II with compound VI, compound III with compound V or compound IV by itself. Elements from compound III-V are commonly used in the semiconductor industry. The bond structure of silicon, the most widely used semiconductor, is shown in Figure 6.

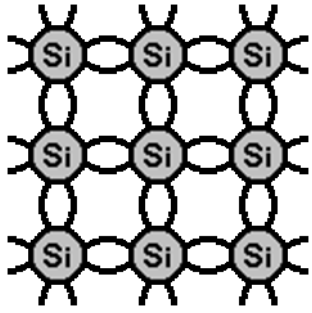

Figure 6 Schematic representation of covalent bond of a silicon crystal lattice.

2.7. The band gap of a semiconductor

The band gap energy of a semiconductor is the minimum amount of energy required to promote an electron from a bound state within the valence band to a mobile state within the conduction band. The concept of the band gap energy is illustrated in Figure 7, where the lower energy level of the semiconductor is the valence band and the energy level where the electron is mobile is the conduction band. Once an electron is promoted, it is no longer bound to a specific nucleus and can travel through the semiconductor. There are three forms of solid state materials: metals, semiconductors and insulators. Their electrical

conductivities vary from each other. Metals consist of positive ions surrounded by delocalized electrons which require a small amount of electrical energy to produce a large amount of electrons in a close circuit [15]. The band gap energies of metals are small and therefore they are highly conductive. Materials considered to be insulators normally have a large band-gap from 4-12 eV [16]. Therefore a large amount of energy is needed to free electrons from insulators. In most cases the material is destroyed before the liberation of an electron. The electrical conductivity of a semiconductor is between that of a metal and an insulator. The energy band gap of a semiconductor varies with temperature, material and geometry. The band gap energy, Eg, has units of electron volts, eV.

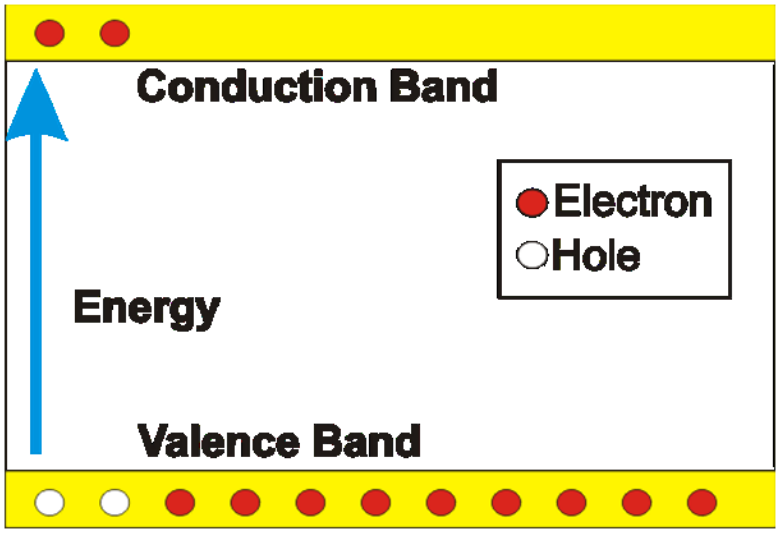

Figure 7 Energy band diagram where the difference between electrons in the conduction band and the valence band is the band-gap energy.

2.8. Doping

Doping in semiconductor refers to the introduction of impurities into intrinsic semiconductor for the purpose of altering its electrical properties. For example, doping a group IV element with a group V element gives an extra valence electron which is unbounded from the atom and doping a group IV element with a group III element leaves a

hole where the fourth valence electron is missing. Semiconductors with excess holes are named *p*-type and those with excess electron are named *n*-type [17]. The *p*-type and *n*-type semiconductor carries both majority and minority carrier. Majority carrier corresponds to higher concentration between holes and electrons of the doped semiconductor.

2.9. Electron hole pairs, carrier generation and recombination

Electron hole pairs are created by promotion of the electron from the valence band to the conduction band by the absorption of energy, typically in the form of a photon. The energy input must be at least equal to the band gap energy in order for an electron to be excited into the conduction band. As a result, the electron leaves behind it a hole in the valence band. Both holes and electrons are called carriers and can carry electrical current. The generation process in open circuit is followed by recombination where upon the electron decays from the conduction to the valence band. Energy released from the recombination of an electron hole pair can be radiative or non-radiative. Radiative (band-to-band) recombination is the emission of photons while the electron decays from the conduction to the valence band. Band-to-band recombination dominates in direct band gap semiconductors and the emitted photon wavelength has the value of the semiconductor band gap energy. Shockley-Read-Hall (SRH) recombination occurs when a material defect takes is the semiconductor. Such defects can be intentionally introduced impurities i.e. by doping. The material defect inside the semiconductor creates an extra energy level between the conduction and valence band. The decaying electron in the SRH recombination moves to the extra energy level and releases the energy either as a radiative photon or non-radiative phonons. Auger recombination involves three particles with two electrons in the conduction band and one hole in the valence band. One of the decaying electrons in the conduction band gives its energy to the second electron and pushes it further into the conduction band. The second electron in turn releases phonons through relaxation to the conduction band edge.

2.10. *p-n* junction

A *p-n* junction refers to an area of semiconductor material where *p*-type material is arranged adjacent to *n*-type material shown in Figure 8. Excess electrons from the *n*-type region seek to lose energy by filling the holes in the *p*-type region and holes in the *p*-type region gain energy by taking electrons from the *n*-type region. This creates an ionized region between the *p-n* junction, named the depletion region. The imbalanced ionization inside the depletion region produces an electric field which extends from the *n* side to the *p* side [18]. In an equilibrium state the force of the electric field is neutralized by the opposing diffusion force of the electrons and holes. The net current of the *p-n* junction, in equilibrium, is zero.

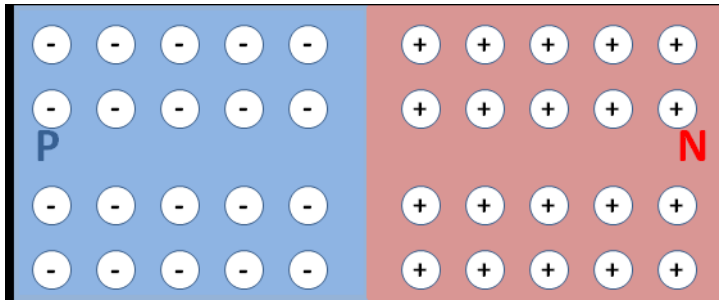

Figure 8 A p-n junction diagram.

Electrical connections can be made to a *p-n* crystal in either forward or reverse bias. Forward bias is defined as applying positive voltage to the *p*-type material and vice versa for reverse bias. In a forward bias connection, holes in the *p*-type and electrons in the *n*-type are pushed towards each other. If the applied voltage exceeds the force of the electric field in the depletion region, holes and electrons are pushed towards the opposite end of the crystal. Electrons from the end of the *p*-type material are attracted to the positive connection and holes from the end of the *n*-type material are attracted to the negative connection. This is the basic operation of a *p-n* junction diode. In a reverse bias connection, the positive terminal is connected to the end of the *n*-type material and vice verse. Electrons from the *n*-

type material are attracted to the positive terminal while holes from *p*-type are attracted to negative terminal. The result is a widening of the depletion region and available current carriers are driven away from the depletion junction to the ends.

2.11. Solar cell structure and operation

A solar cell is a device which converts photons into electrical energy in the form of current and voltage. The most commonly known configuration of the solar cell is a *p*-*n* junction made with III-V semiconductor. The cross section of a basic solar cell is shown in Figure 9. The *n* and *p* junctions are also called emitter and base junctions. The top of the *p*-*n* junction is covered by both a metal contact and anti-reflective (AR) coating while the bottom is covered by a metal contact only. An operating solar cell requires external leads connecting to the top and bottom cell contact and a load between the leads. Photovoltaic operation begins when a photon excites the *p*-*n* junction and creates an electron hole pair. The electron is pushed by the depletion region to the *n*-type while the hole is forced to the *p*-type. In order to complete the circuit, the electron then travels through the external load and recombines with the hole in the *p*-type.

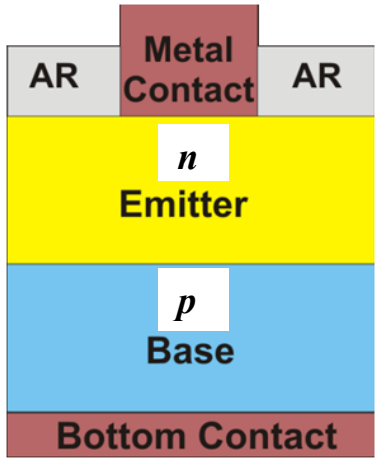

Figure 9 Basic solar cell structure.

2.12. Parameters and effects (resistance: series, shunt, temperature, concentration)

The performance of a solar cell is demonstrated by its efficiency. The efficiency of a solar cell can be determined by its operating characteristics where they includes the short circuit current (I_{sc}), open circuit voltage (V_{oc}), fill factor (FF) and maximum measured power. The efficiency of a solar cell is the ratio of cell produced power with incident photon power. It is defined as [19]:

$$\eta = \frac{V_{oc} I_{sc} FF}{P_{in}} \qquad 2\text{-}10$$

where I_{sc} is the short circuit current, V_{oc} is the open circuit voltage, FF is the fill factor and P_{in} is the input power.

I_{sc} is dependent on the light concentration, input spectrum, internal quantum efficiency and optical properties of the solar cell (absorption and reflection). The V_{oc} of a *p-n* junction solar cell is the level of bias required to reduce the photocurrent to the point where it is equal to the dark current, such that the net current through the device is zero. Both I_{sc} and V_{oc} are the maximum current and voltage a solar cell could produce. The FF is determined at the point of maximum measured power (MMP) and is the ratio of measured power and product of I_{sc} and V_{oc} shown in Figure 10.

$$FF = \frac{V_{mp} I_{mp}}{V_{oc} I_{sc}} \qquad 2\text{-}11$$

where V_{mp} is the voltage at the maximum power, I_{mp} is the current at the maximum power.

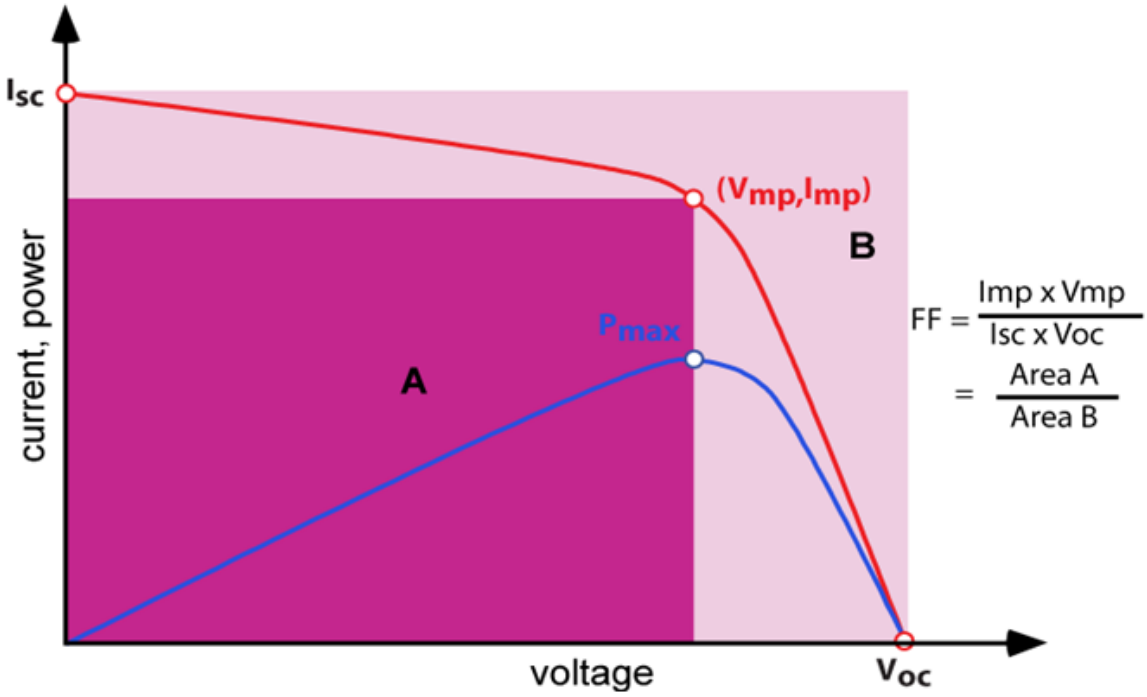

Figure 10 Current-Voltage of an ideal solar cell with low FF [20].

In a practical case the *FF* is always less than one due to the parasitic resistance effects of shunt and series resistance. Such effects exist in all electronic devices. An equivalent circuit diagram is shown in Figure 11. Solar cells are *p-n* junction devices and all single *p-n* junction devices have diode characteristics. Hence a solar cell without light illumination has the same electrical characteristics as a diode. When light shines on a solar cell, it is considered to be a current source connected to a diode in parallel. A portion of light generated current goes to the diode,I_D, and the rest of the generated current, I, is exported. The voltage, V, generated from the solar cell is the combination of I_D with the internal resistance of the diode.

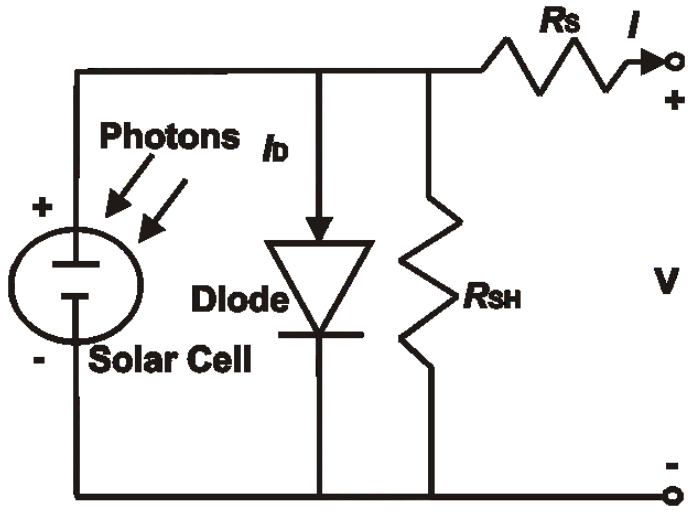

Figure 11 Equivalent circuit diagram for a solar cell where R_S is the series resistance, $R_{SH}$is the shunt resistance, $I_D$is the diode current, $I$is the operating current and $V$is the operating voltage.

Both series and shunt resistance of a solar cell can be approximated from the slope of the IV curve near the V_{oc} and the I_{sc} points. Solar cell efficiency can be optimized by increasing the shunt resistance and reducing the series resistance. Sources of series resistance within a solar cell include internal resistance, contact resistance between the metal contact at the top and the bottom of the semiconductor. Series resistance does not affect the V_{oc} of a solar cell but does influence the $fill\ factor$ by lowering the electrical cell current. Shunt resistance normally appears from fabrication defects rather than bad designs. Solar cells with low shunt resistance allow current to be diverted through alternative pathways and results in a lower V_{oc} and FF. Solar cells are made with semiconductors and therefore possess the thermal characteristic of a semiconductor device. In a semiconductor device, an increase in temperature reduces the band-gap energy of the material. The reduction of the band-gap energy is caused by excess energy in the electrons. The existence of this excess energy means that less energy is required to excite an electron to the conduction band. Hence more electrons are available for electrical conduction. In general, solar cells with higher temperatures produce a slightly larger short circuit current density with a lower open circuit voltage shown in Figure 12.

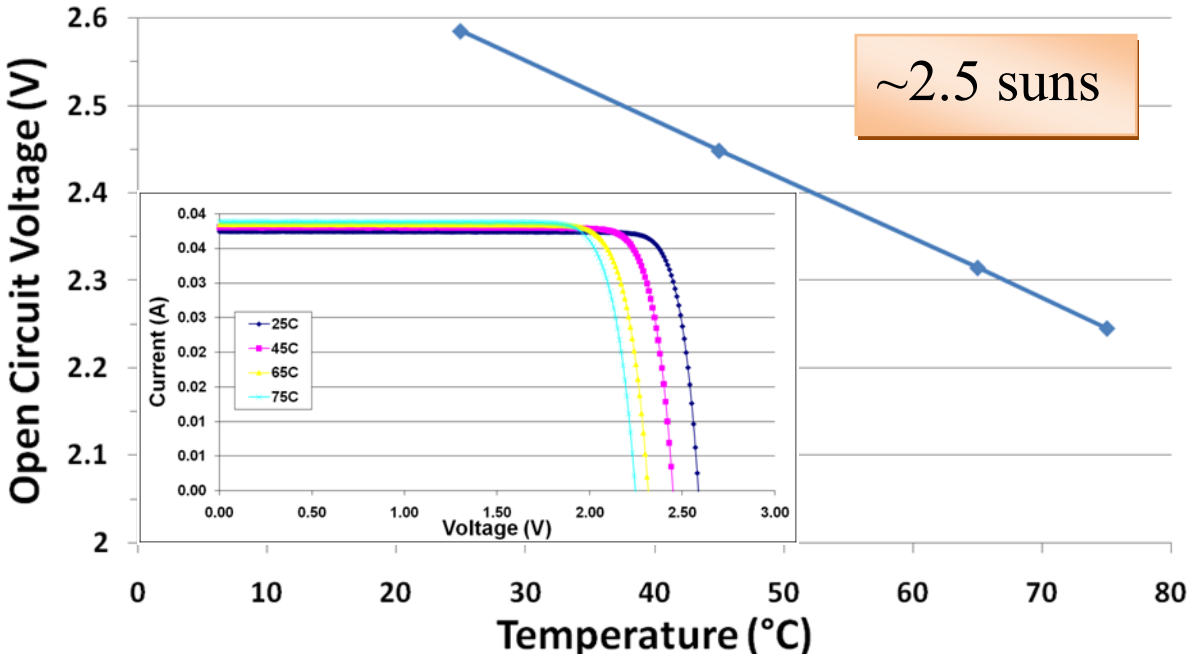

Figure 12. 1 cm^2 bare cell under constant illumination of 2-3 suns. The current-voltage behavior of the multi-junction solar cell with temperature varies from 25°C to 75°C and shows a decrease of 6.8 mV/°C using a class A simulator.

2.13. Multi junction cell structure

The theoretical efficiency of a single *p-n* junction solar cell is governed by the Shockley-Queisser limited and the theoretical limit for a single junction silicon solar cell is 33.7% [21]. The multi-junction cell (or tandem cell) was a conceptual way of overcoming the fundamental limitation of the Shockley-Queisser solar cell. The efficiency of a solar cell plays a vital role in determining the cost of generating electricity. Tandem cells overcome the limitations of a single junction cell by converting the broad solar spectrum more efficiently. It allows broader absorption while reducing thermalization losses by splitting the absorbed spectrum between various band-gaps. The concept of the multi-junction was first developed more than 50 years ago [23] and two technological approaches have been studied. They are the mechanically stacked approach and the monolithic approach. In a mechanically stacked approach, different band-gap cells are fabricated individually on individual substrates and then brought together, as shown in Figure 13b. Each solar cell has its own positive and negative metal contact and can be connected separately.

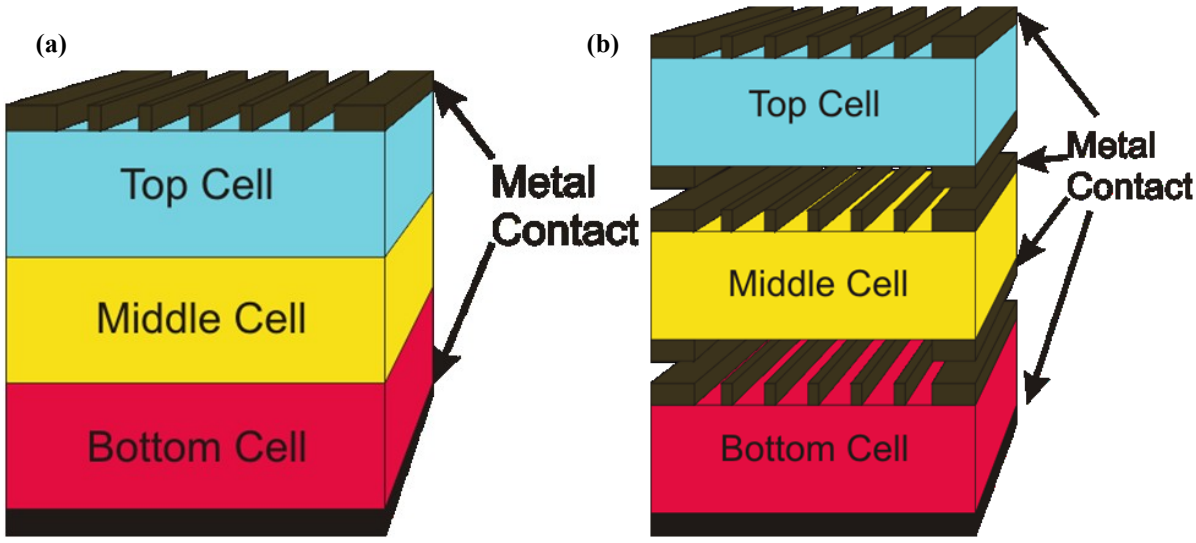

Figure 13 (a) Cells integrated monolithically (b) tandem cells stacked mechanically.

In the monolithic approach shown in Figure 13a, all cells are grown on the same substrate and connected by tunnel junctions. With this approach, the fabricated device only has one positive and one negative metal contact like a single junction solar cell. The open circuit voltage of a monolithic stack is the sum of the open circuit voltages of each layer and the total short circuit current is equal to the lowest short circuit current of the individual sub-cells. Recent developments of high-efficiency, III-V material, multi-junction solar cells are based on monolithic triple-junction stacks made of GaInP/GaAs/Ge [22].

2.14. Optics for concentration (refraction, reflection)

The concept of concentrating optics is to gather as much light as efficiently as possible onto the solar cell. The concentration can be achieved by reflection or refraction or a combination of both. The goal is to reduce the cost of electricity generated by reducing the solar cell area and utilizing the lower cost optic to enable large area light collection [24]. Furthermore it is preferable to illuminate the solar cell uniformly rather than focusing on a

single spot, in order to avoid the creation of hot spots and unwanted lateral currents in the cell. It is also desirable to have a large acceptance angle for the incident light. In optics the angle of light reflection is simply the angle of the incidence relative to the normal of the optical interface. The angle of refraction is governed by Snell's law and its relationship regarding the refraction angle is:

$$\frac{\sin\theta_1}{\sin\theta_2} = \frac{n_2}{n_1} \qquad 2\text{-}12$$

where θ_1 is the angle of incidence between the two isotropic media, θ_2 is the angle exiting between the two isotropic media, n is the refractive indice of the respective media.

2.15. Concentrator types (Fresnel, Dish)

Commercial concentrators use either refractive lenses, Figure 14a, or reflective dishes, Figure 14b, or a combination of both. In the case of the refractive lens, larger lenses are required to focus more light to a given spot for higher concentration. In practice this requires a very thick and costly lens. The Fresnel lens has been explored as an alternative to these traditional lenses. A Fresnel lens may be used for line focus, or point focus, depending on the application.

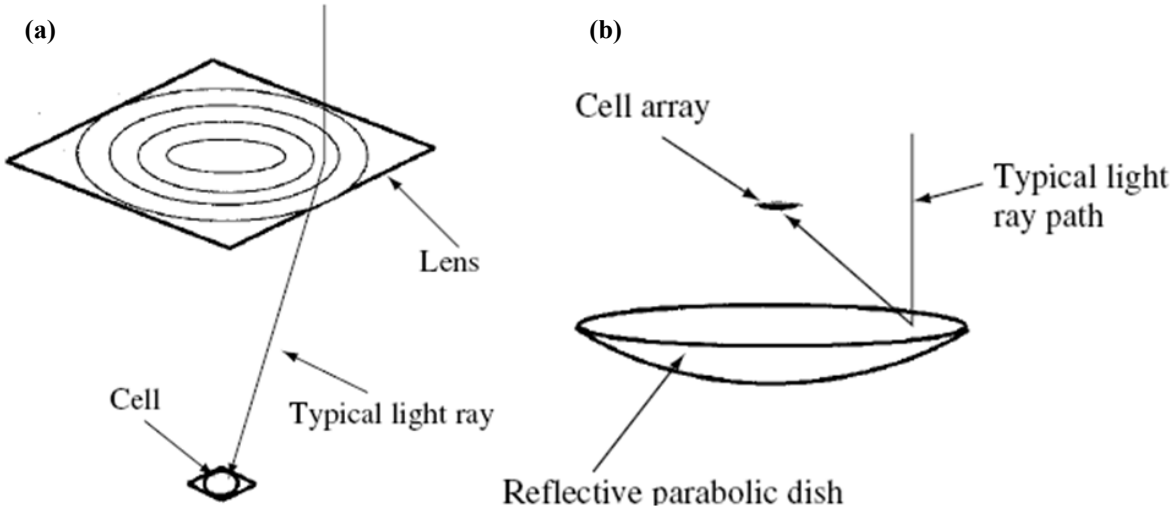

Figure 14 (a) Fresnel lens system (b) parabolic dish system [24].

2.16. Fresnel optics

In general, the Fresnel lens is governed by Snell's law for refraction. Refractive lenses used in PV concentrators are aspheric. Traditional spherical lens encounters the challenges of both spherical and chromatic aberrations. Spherical aberration refers to light striking the edge of the lens having a closer focal point relative to the lens than light striking the center of the lens. Chromatic aberration is the light dispersion of lens material due to the variation of its refractive index with light. Different wavelengths of light passing through a lens will have different focal point. An aspheric lens is capable of correcting the spherical aberration by bending the spherical surface to an elliptical shape. The aspheric lens formula is given by:

$$Z = \frac{Cr^2}{\left(1+\sqrt{1-(k_c+1)C^2r^2}\right)} + \sum_{i=1}^{q} \propto_i |r^{2i}| \qquad 2\text{-}13$$

where Z is the height of the aspheric surface, r is the radial distance, C is the curvature at the vertex, k is the conic constant and $\propto$ is the aspheric coefficient. The Fresnel design provides a cost saving solution by removing slabs of lens material in an aspheric lens that do not contribute to the bending of light rays to a focal point. The surface profile of the lens which is responsible for the optics is preserved but the volume and weight of the lens is reduced. The geometry of an aspheric lens is shown in Figure 15.

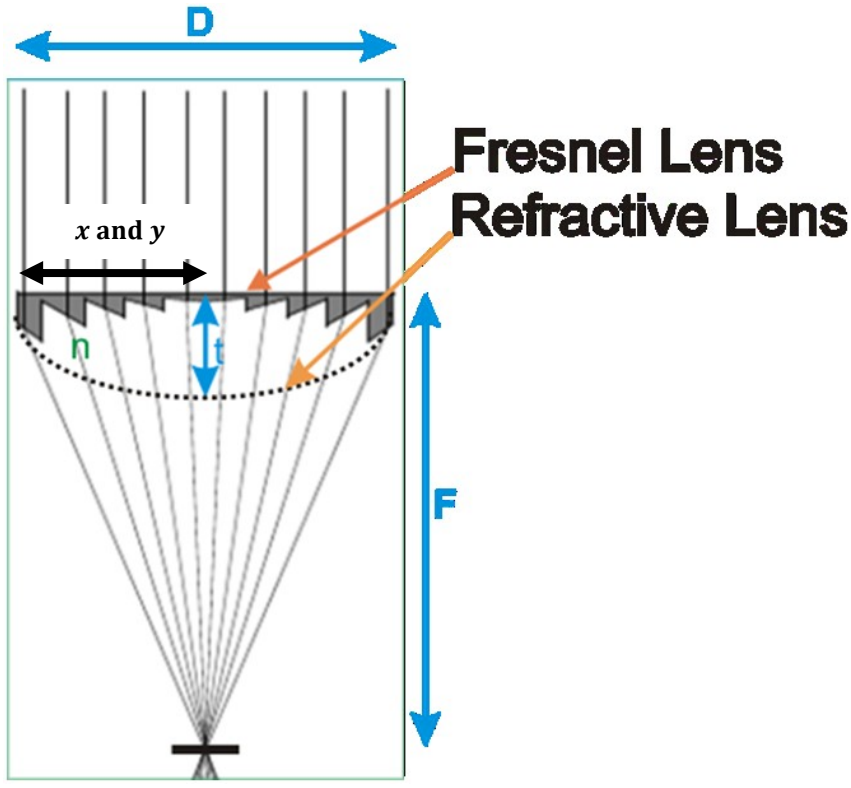

Figure 15 Aspheric Fresnel grooves in lens optical geometry.

Fresnel lenses like other refractive lenses, have optical losses. Most of the optical losses come from the interface reflection and material absorption [24], [25]. With the application of an anti-reflection coating the interface losses can potentially be reduced [26]. There is a draft angle incorporated when manufacturing Fresnel lens. The draft angle is the vertical normal to the Fresnel lens. It is normal practice for manufacturers to add a few degrees to the draft angle for easier extraction of the moulded part with the actual lens.

When light strikes the drafted surface, originally vertical, it is deflected and contributes to the transmission loss of the Fresnel lens.

2.17. Homogenizer

MJ solar cells under concentration require a uniform flux incident on the cell active area. A mismatch caused by flux intensity inhomogeneity results in a loss of $\boldsymbol{FF}$ and efficiency due to creations of hot spots within the cell. The use of refractive optics to achieve concentration suffers from the drawback of chromatic aberration where the lens has a different refractive index for different wavelengths of light [27]. One of the solutions is to add a secondary optic, a homogenizer, to the concentrator system for color mixing and double imaging [28], [29]. There are two main types of homogenizer, the hollow metallic type and the prism type, as shown in Figure 16. Both types reflect light inside the structure. The effectiveness of the homogenizers to correct chromatic aberration has been studied through ray tracing simulations with results showing a 25% improvement in cell operation [30].

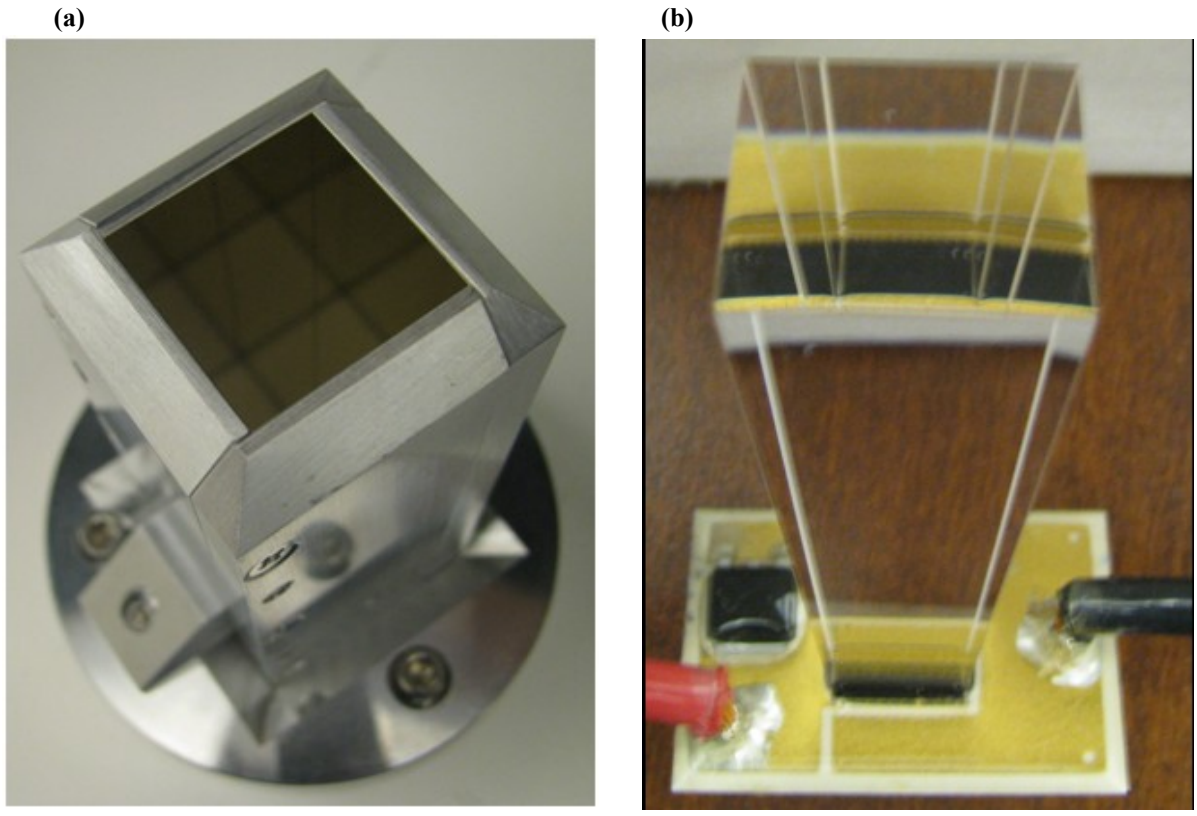

Figure 16 Homogenizer (a) metallic hollow (b) prism.

2.18. Carrier receiver structure (material, size and connections)

Triple junction solar cells are grown on brittle Ge substrates with a thickness of around 170 µm. As a result, they are required to be packaged on a carrier for structural support, heat dissipation and electrical interconnection. The carrier is a direct bonded copper (DBC) substrate and is commonly used in power electronic modules. DBC substrates are sheets of copper thermally bonded with an insulated metal substrate at high temperature [31]. The copper layer is bonded on top of the insulated substrate and the material for the insulated substrate can be alumina, aluminum nitride and beryllia. For the devices tested within this thesis, carrier mounting was performed by CMC Microsystems, Cyrium Technologies and Sherbrooke University using a range of receiver designs having material or geometry differences.

2.19. Receiver geometry

The overall size of a solar cell is 1 cm by 1.2 cm with a 1 cm^2 acceptance aperture area as shown in Figure 17. A solar cell receiver is composed of a base board, a solar cell mounted on the board and a bypass diode. The function of the base board is to provide electrical conduction from the solar cell to external connections and to transfer heat produced from the solar cell to the cooling unit. A typical receiver module is shown in Figure 18.

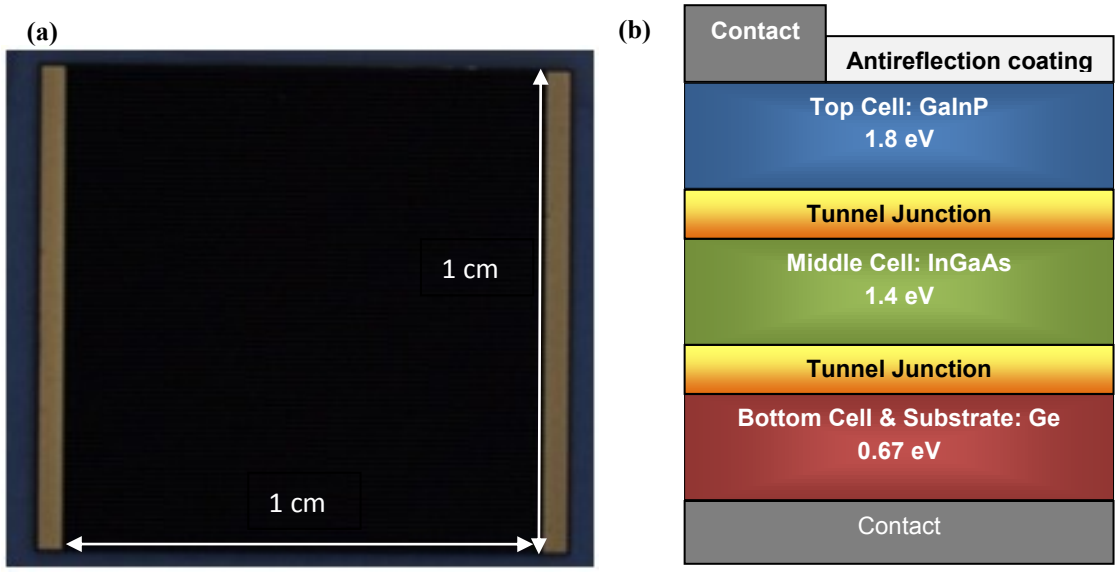

Figure 17 Bare III-V triple junction solar cell (a) Overview, (b) Schematic with sub-cells connected in series by tunnel junctions.

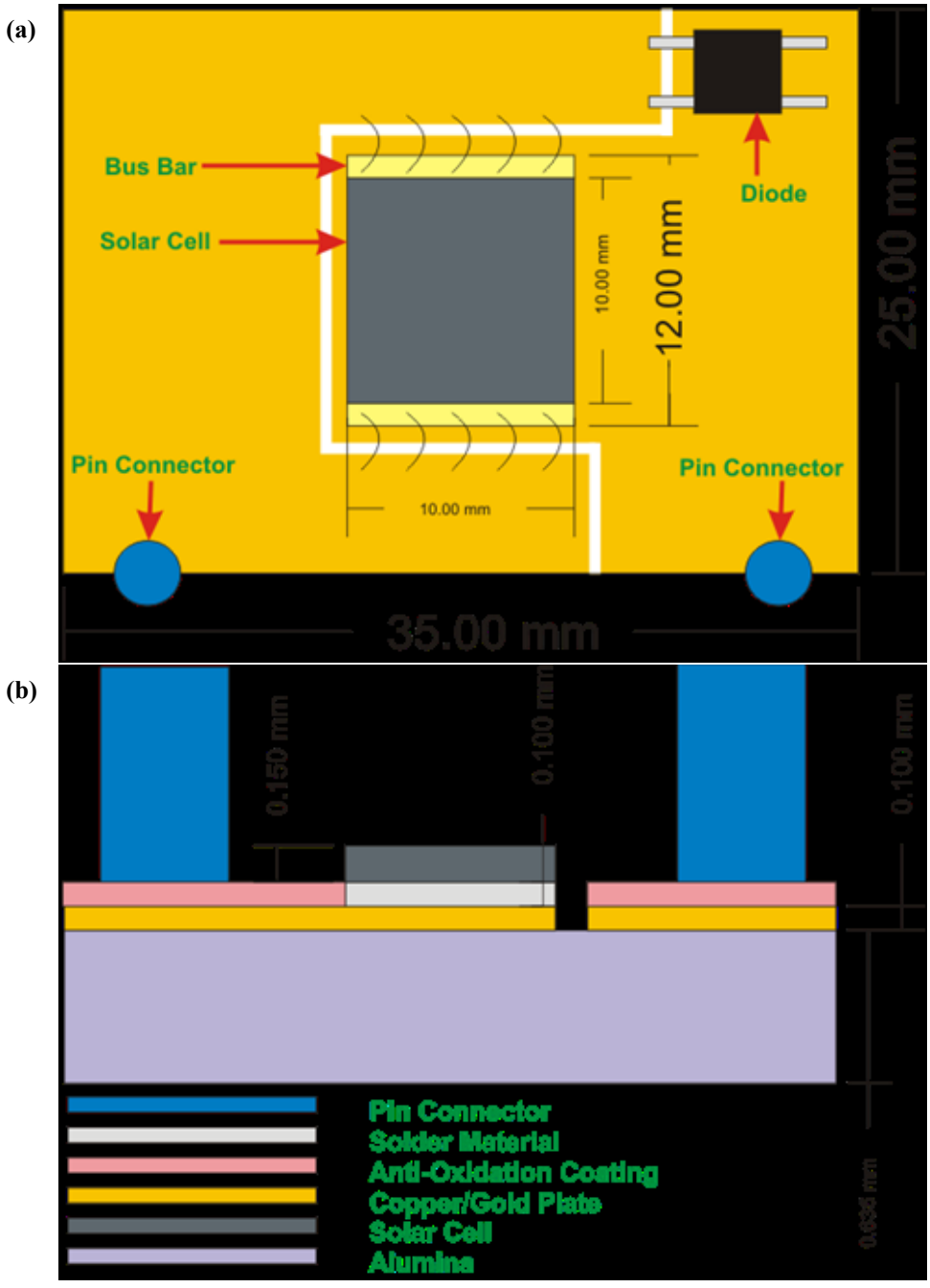

Figure 18 Schematic of a general receiver design with (a) top view and (b) cross section.

The carriers under the investigation in this thesis are composed of three basic layers. The top layer serves as an electrical conductor and facilitates heat spreading. The middle

layer, made with either alumina or polytetrafluoroethylene material, provides structural support and the bottom layer provides heat transport and lateral spreading.

2.20. Receiver electrical resistance and power consumption

One of the main functionalities of the receiver is to provide an electrical connection from the solar cell to the external circuit. A general electrical model of a receiver is shown in Figure 19.

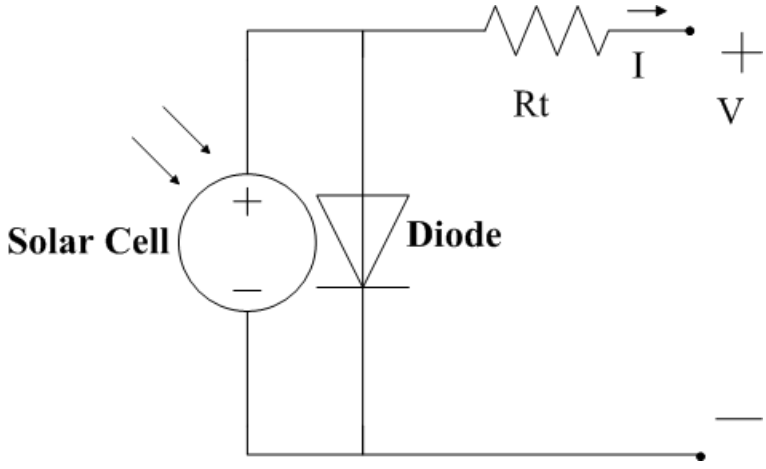

Figure 19 Electrical model of a receiver. R_t represents the total resistance of the receiver.

The solar cell is coupled in parallel with a diode and operates in forward bias. Solar cells under high concentration can achieve high current densities. For example, at a concentration of 1000-suns with one sun equivalent to 1 kW/m^2 the current produced by a 1 cm^2 triple junction solar cell is 14 A/cm^2 shown in section 3.12. The electrical conductive layer, top copper layer, largely contributes to the total resistance of the receiver. The relationship between conductive layer thickness and the receiver resistance is shown in Figure 20, and Figure 21 demonstrates the total power consumption of a receiver (Length/Width ratio = 1) with various electrical currents applied.

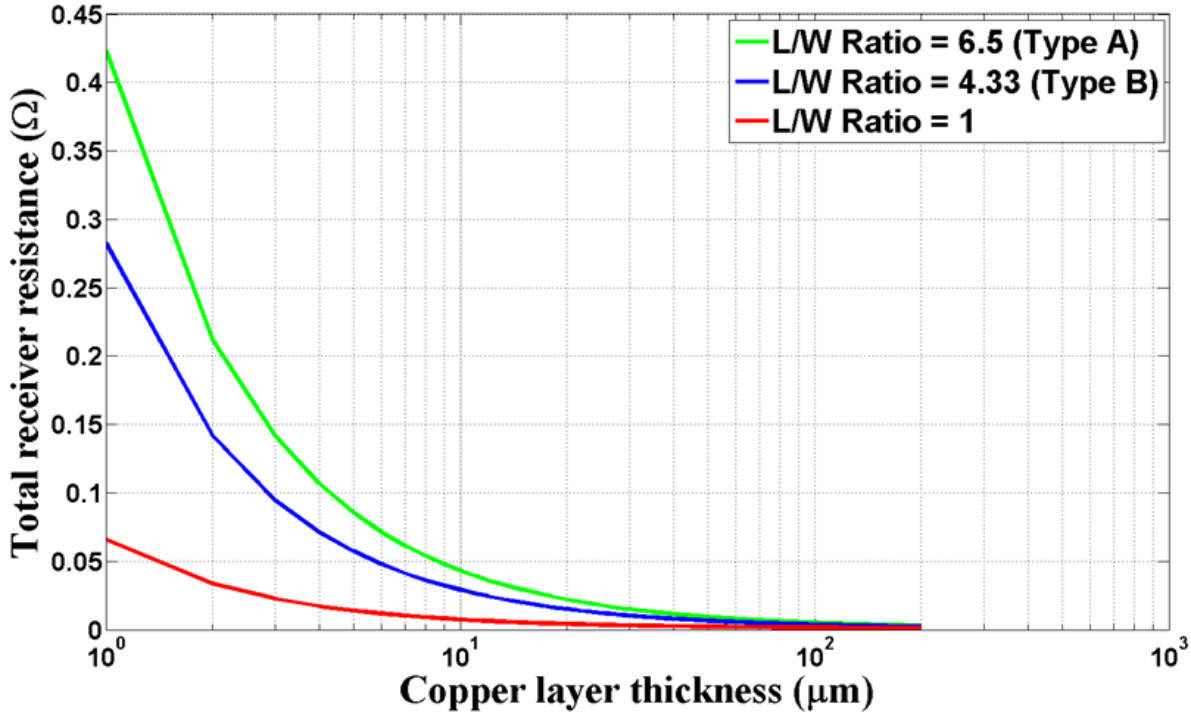

Figure 20 Total receiver resistance as a function of copper layer thickness for various receiver length/width ratios.

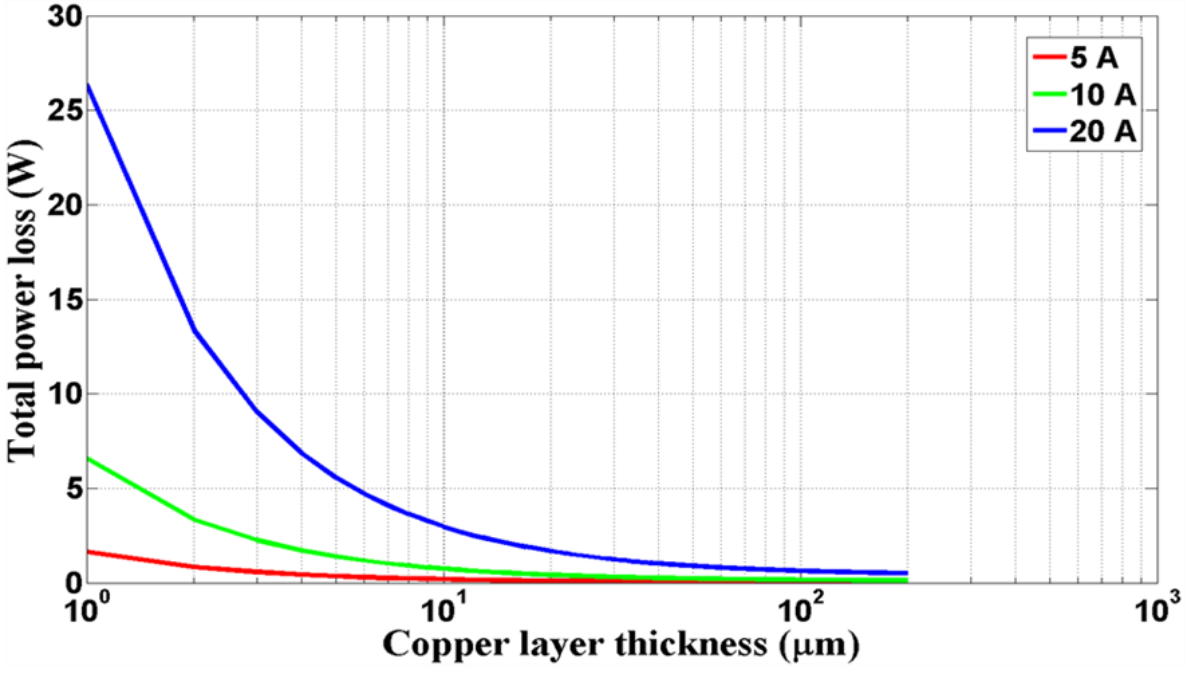

Figure 21. Total power loss as a function of copper layer thickness for various current inputs.

2.21. Receiver material

High efficiency triple junction solar cells can achieve photovoltaic efficiencies above 40% [32]. A solar cell with 40% efficiency is able to convert 40% of incident solar radiation into electrical energy. The remaining 60% of solar radiation energy is converted into thermalisation (energy above band-gap) losses [33], sub-band-gap losses (energy below band-gap) and emission radiation losses [34]. Most of the heat produced by the cell is transported from the solar cell through the receiver to the cooling device. Materials chosen for the receiver are required to have high thermal conductivity. Common materials such as silver and copper possess high thermal conductivity and are suitable materials as a top layer of the receiver. The middle layer of the receiver is an electrical insulator which prevents electrical grounding between the solar cell and the heat sink. Hence, material for the middle layer should possess low electrical conductivity and high heat conductivity. Available receiver materials, such as alumina, aluminum nitride, copper and beryllium oxide are listed in Table 1 along with their thermal conductivities and thermal resistance values.

Substrate and thickness (μm)	Thermal Conductivity (W/cm/K)	Thermal resistance in one dimension for 1 cm^2 (K/W)
Al_2O_3 (635)	0.24	0.26
Al_2O_3 (250)	0.24	0.11
AlN (635)	1.8	0.035
BeO (635)	2.8	0.023
Cu (30)	4	< 0.001
Cu (100)	4	0.0025
Cu (300)	4	0.0075
Ag (100)	4.3	0.0023
SnAg (100)	0.5	0.02
SnAg (250)	0.5	0.05
Ge (175)	0.58	0.052

Table 1 Thermal conductivity, thermal expansion and thermal resistance for various materials at various thicknesses

2.22. Thermal stack

Cooling of the solar cell typically takes place at the bottom of the solar cell where the cell is attached to the heat sink. In a concentrator module there is a receiver between the solar cell and the heat sink. Thermal energy from the solar cell passes through the receiver before the heat sink. Each layer within the receiver contributes thermal resistance individually and total resistance can be seen as a thermal stack. The global thermal resistance of the stack, excluding the lateral diffusion, is the sum of the thermal resistances of each separate layer. In a one dimensional model, where all receiver layers have the same length and width dimension as the solar cell, the global thermal resistance can be described as a thermal circuit [35]:

$$R_{1D} = \sum_{i=1}^{n} \frac{L_i}{k_i A} \qquad 2\text{-}15$$

where k_i is the thermal conductivity of an i^{th} layer, A is the cross section area of the heat flow, L_i is thickness of i^{th}layer. In a steady state case where heat transfer occurs through one-dimensional layers by conduction the heat flow Q equation is:

$$Q = \frac{T_1 - T_2}{R_{1D}} \qquad 2\text{-}16$$

where T_1-T_2 is the temperature difference between the top and bottom layer.

In a one dimension thermal calculation, the material properties and layer thicknesses are independent variables. An increase in material thickness or a lowering of the thermal conductivity shall increase the difference in temperature between the edges of the material.

2.22. Thermal spreading

When studying thermal diffusion in a two or three dimensional application, thermal spreading takes place when a heat source is coupled to a larger area. Figure 22 demonstrates the heat flux pattern of a receiver (blue), with a rectangular heat source (solar cell), red, sitting on top. The thermal flux spreads throughout the sink and diffuses to the bottom, coolest part of the receiver.

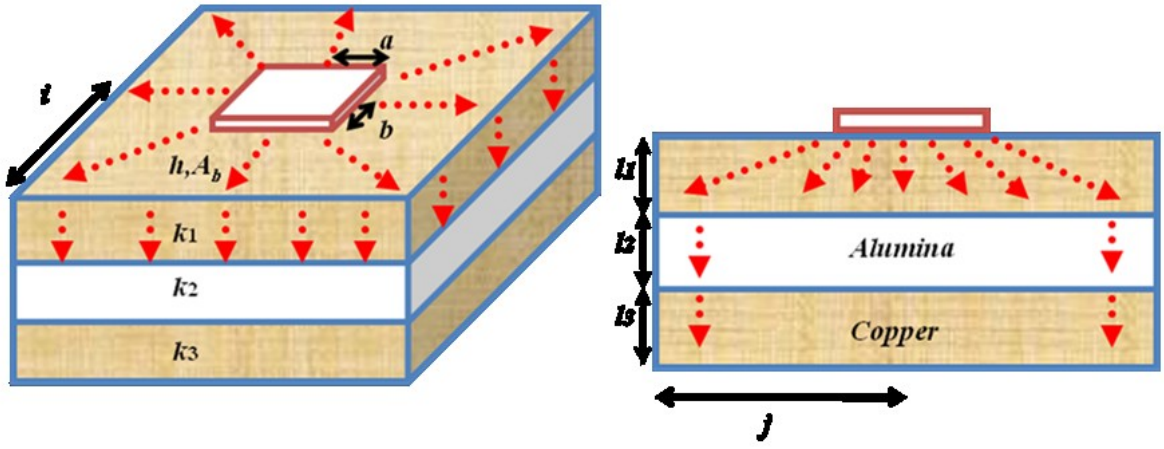

Figure 22 Heat flux travelling paths on the heat sink (a) overview (b) cross section view. The flux patterns are represented by read arrows. The dimensions for the receiver are 5 cm by 5 cm or 2 cm by 2 cm. The initial temperature at the bottom of the receiver is 0°C.

Thermal spreading has been largely studied in the 1990 for high power electronics (ie. central processor cooling). Several analytical models have been developed for electronic packaging where an electronic device is depicted as a heat source on top of a sheet heat sink with convective heat transfer [36], [37]. The study of thermal spreading is normally not a trivial issue and the key to the solution is to correctly determine the thermal resistances. Consider the sample configuration in Figure 22 where a square source of zero thickness is located on a triple layer receiver where there is no explicit thermal solution. The thermal resistance changes with various receiver geometry design.

The total thermal resistance, R_{total}, of an object in three dimensions, like the one in Figure 22, can be approximated by the sum of two independent terms according to:

$$R_{total} = R_{1D} + R_{spreading} \quad 2\text{-}17$$

where R_{1D} is the uniform flow from the square source to the bottom of the receiver without lateral spreading and $R_{spreading}$ is the multi-dimensional spreading resistance.

The uniform flow is given by [38]:

$$R_{1D=} = \sum_{i=1}^{N} \frac{l_i}{k_i A_i} \quad 2\text{-}18$$

where l_i is the thickness of the each layer, k_i is the thermal conductivity of each layer in the receiver and $A_i$is the surface area of each layer. The multi-dimensional spreading resistance can be approximated by [39]:

$$R_{spreading} = \frac{1}{a^2 b^2 ijk_1} \sum_{m=1}^{\infty} \sum_{n=1}^{\infty} \frac{\sin^2(a\delta_m)\sin^2(b\lambda_n)}{\delta_m^2 \lambda_n^2 \beta_{m,n}} * \varphi(\beta_{m,n}) + \frac{1}{2b^2 ijk_1} \sum_{n=1}^{\infty} \frac{\sin^2(b\lambda_n)}{\lambda_n^3} * \varphi(\lambda_n) + \frac{1}{2a^2 ijk_1} \sum_{m=1}^{\infty} \frac{\sin^2(a\delta_m)}{\delta_m^3} * \varphi(\delta_m) \quad 2\text{-}19$$

where

$$\varphi(\zeta) = \frac{(\alpha e^{4\zeta l_1} + e^{4\zeta l_1}) + \gamma\left(e^{2\zeta(2l_1+l_2)} + \alpha e^{2\zeta(l_1+l_2)}\right)}{(\alpha e^{4\zeta l_1} - e^{4\zeta l_1}) + \gamma(e^{2\zeta(2l_1+l_2)} - \alpha e^{2\zeta(l_1+l_2)})} \quad 2\text{-}20$$

and

$$\gamma = \frac{\zeta + h/k_2}{\zeta - h/k_2}, \qquad \alpha = \frac{1 - \omega}{1 + \omega}, \qquad \omega = k_2/k_1 \qquad \text{2-21, 22, 23}$$

and [40]

$$k_2 = \sqrt{k_p * k_s}, \; k_s = \sum_{i=1}^{N} l_i \Big/ \sum_{i=1}^{N} \frac{l_i}{k_i}, \; k_p = \sum_{i=1}^{N} \frac{l_i}{k_i} \Big/ \sum_{i=1}^{N} l_i \qquad \text{2-24, 25, 26}$$

with a, b are the half-lengths of the source area, i, j are the half-lengths of the flux channel (receiver). The eigenvalues for these solutions are $\beta_{m,n} = \sqrt{\delta_m^2 + \lambda_n^2}$, $\delta_m = m\pi/i$ and $\lambda_n = n\pi/j$, and they are denoted by ζ in equations (2-20, 2-21).

Using equations (2-17) to (2-26), the temperature of the square source in Figure 22 with either a 2 or 5 cm triple layer receiver side length and various copper thicknesses on the receiver is shown in Figure 23. The input thermal power is 1000 kW/m^2 and the cooling power at the bottom of the receiver is 15000 W/m^2/K. The boundary conditions for all faces except the bottom are considered to be insulators where no heat travels through the boundary. The ambient temperature is zero degree and the bottom is the receiver is fixed at zero degree. Initial analytical results demonstrate both a 5 cm by 5 cm and a 2 cm by 2 cm receiver have an optimum top copper thickness. A 5 cm by 5 cm receiver have both lower cell temperatures and optimum copper thickness than a 2 cm by 2 cm receiver. The thickness of the top copper determines both the amount of lateral thermal spreading and total thermal resistance. As copper thickness decreases on the receiver before the optimum design point, it is reducing the thermal spreading capability of the receiver. Therefore the cell temperature increases. As copper thickness increases on the receiver after the optimum design point, it is increasing the thermal resistance of the receiver. Hence, the cell temperature increases. The optimum point is the equilibrium of both thermal spreading and thermal resistance of a receiver.

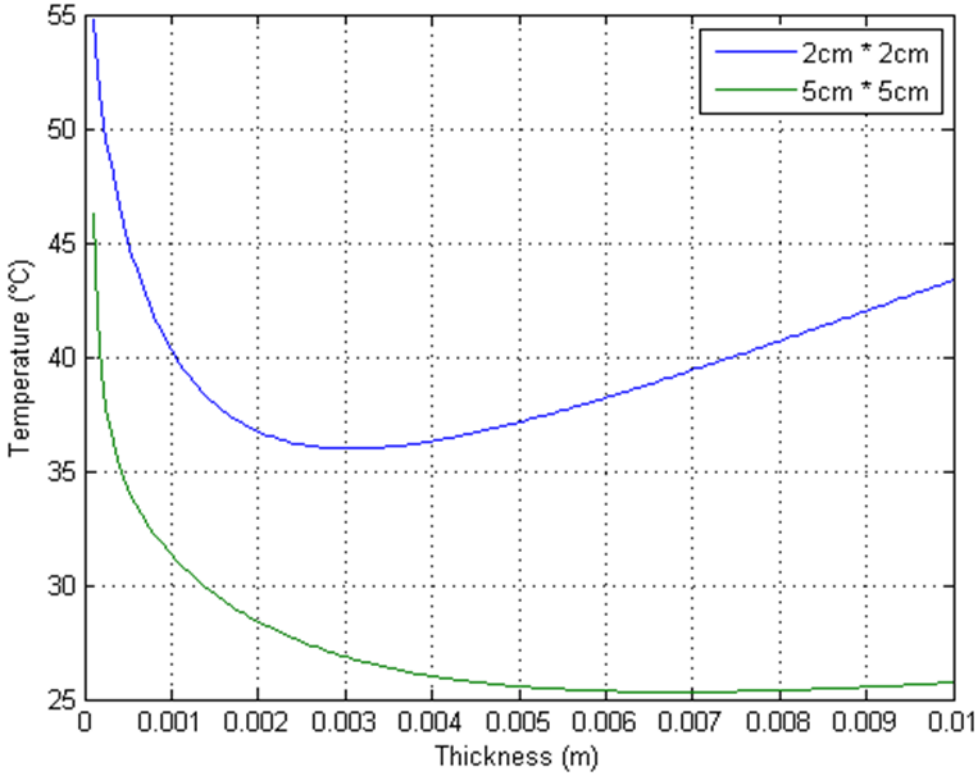

Figure 23 Averaged cell temperatures as a function of top copper layer thickness for both 5 cm by 5 cm (green line) and 2 cm by 2 cm (blue line) size triple layer receiver. (data courtesy of Aaron Muron, uOttawa SUNLab).

Chapter 3 Experimental method

3.1. Introduction

Experimentation and characterization of solar devices on both low and high power solar simulators is conducted in the University of Ottawa, School of Information Technology and Engineering's SUNLab. This chapter will examine and analyse the thermal effect of a concentrator triple junction solar cell under continuous illumination using indoor controlled solar simulator. Beginning with a description of both the low and high power solar simulator setup, instruments and simulator calibration methodologies will then be explored, followed by an explanation of methodology used in the characterization process.

3.2. Oriel solar simulator overall setup

Devices subject to low concentration sunlight are illuminated by the Newport Oriel solar simulator. The Oriel employs a 1500 W lamp and it delivers concentrations up to 20X. For lower than 20X solar concentration, a neutral density having 15% calibrated transmission filter is added. Additional optics allow further concentration up to 100 suns. Test devices are placed on a custom gold plated chuck with a device vacuum hold for stabilisation. A Peltier element, powered by an Alpha Omega Series 800 temperature controller, is inserted between the chuck and the stage to facilitate temperature control of the chuck. A thermistor extends from the chuck to the temperature controller providing real time feedback of thermal readings. Current-voltage characterization of the device is performed by a Keithley 2601A system source meter, which is capable of four point sensing and is used on all measurements by this Oriel setup. Four point sensing allows the elimination of wire and contact resistance in the measurements. This technique is commonly used in the electronics industry. Electronic equipment used in the Oriel solar simulator setup, shown in Figure 24, is hardware connected to a central computer and

remotely controlled via Labview software for the chuck temperature, the lamp intensity and the current-voltage characterization.

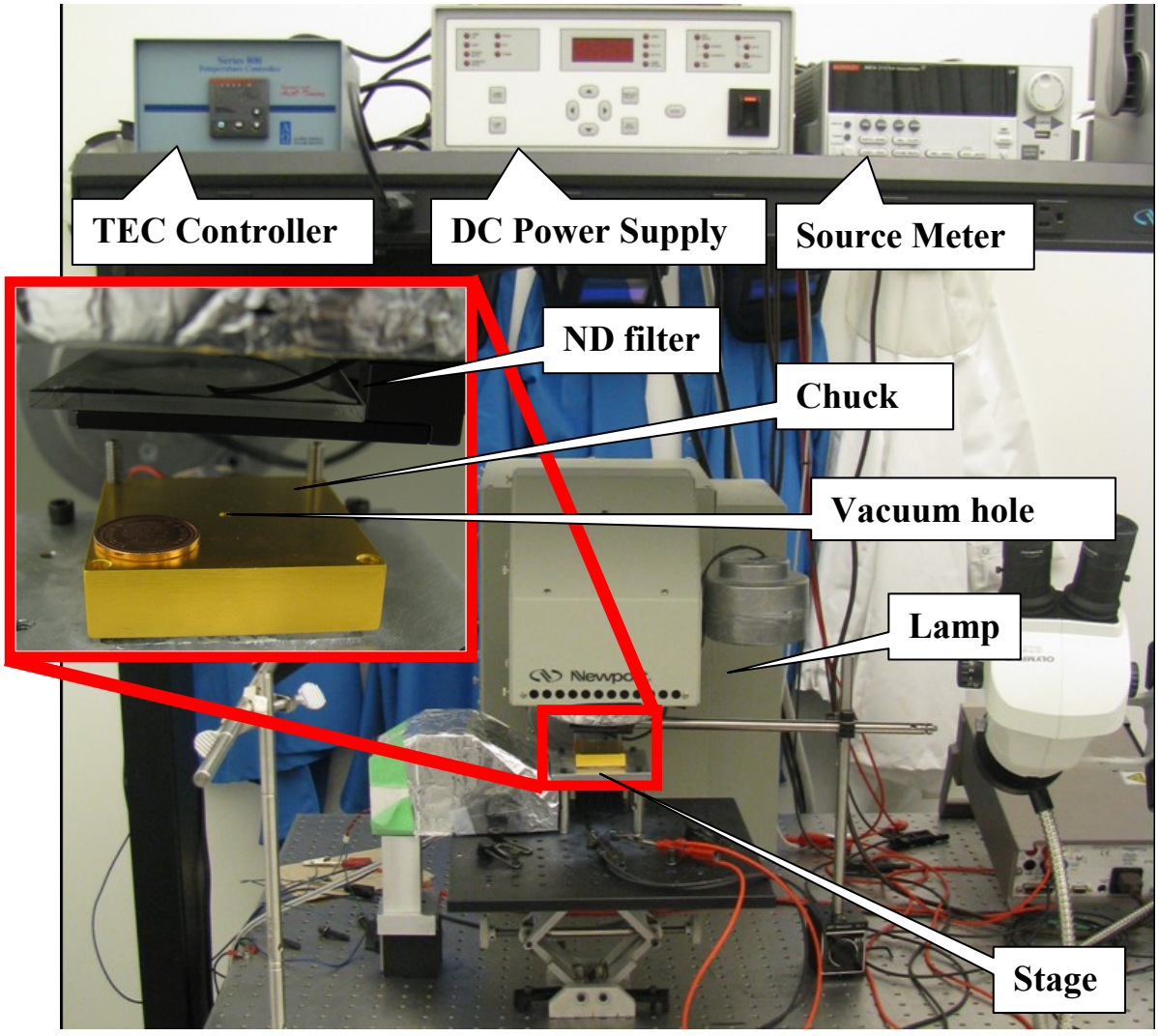

Figure 24 Picture of the Newport Oriel solar simulator system

3.3. XT-20 and XT-30 solar simulator overall setup

Device subject to high concentration (100X – 1000X) are illuminated by the Spectrolab XT-20 and XT-30 simulators from Spectrolab. The XT-20 is an early loan unit from the simulator manufacturer to the SUNLab where the XT-30 is the final production model.

Both simulators consist of a light source unit, a test platform, a water-chiller for cooling, a servo system for controlling the lamp movement, a power station for controlling power to the lamp and an current-voltage station for data collection from output of the solar cell. A pictorial setup of the XT-30 is shown in Figure 25. The light source of the XT-20 and XT-30 is a 1600 W and 3000 W Xeon arc lamp with a metallic homogenizer attached to the bottom of the cone respectively. In addition an AM1.5D filter was installed to ensure low AM1.5 atmospheric direct solar radiation. The test platform where the solar cells are located consists of five test locations. Each location is linearly connected to each other by water tubes, which are in turn connected to the water chiller. A NESLAB ThermoFlex 900 is used for the XT-20 and a ThermoFlex 2500 for the XT-30 to cool both the source lamp and the stage platform where the solar cells are placed. This is designed to provide continuous cooling at a constant set temperature throughout an experiment.

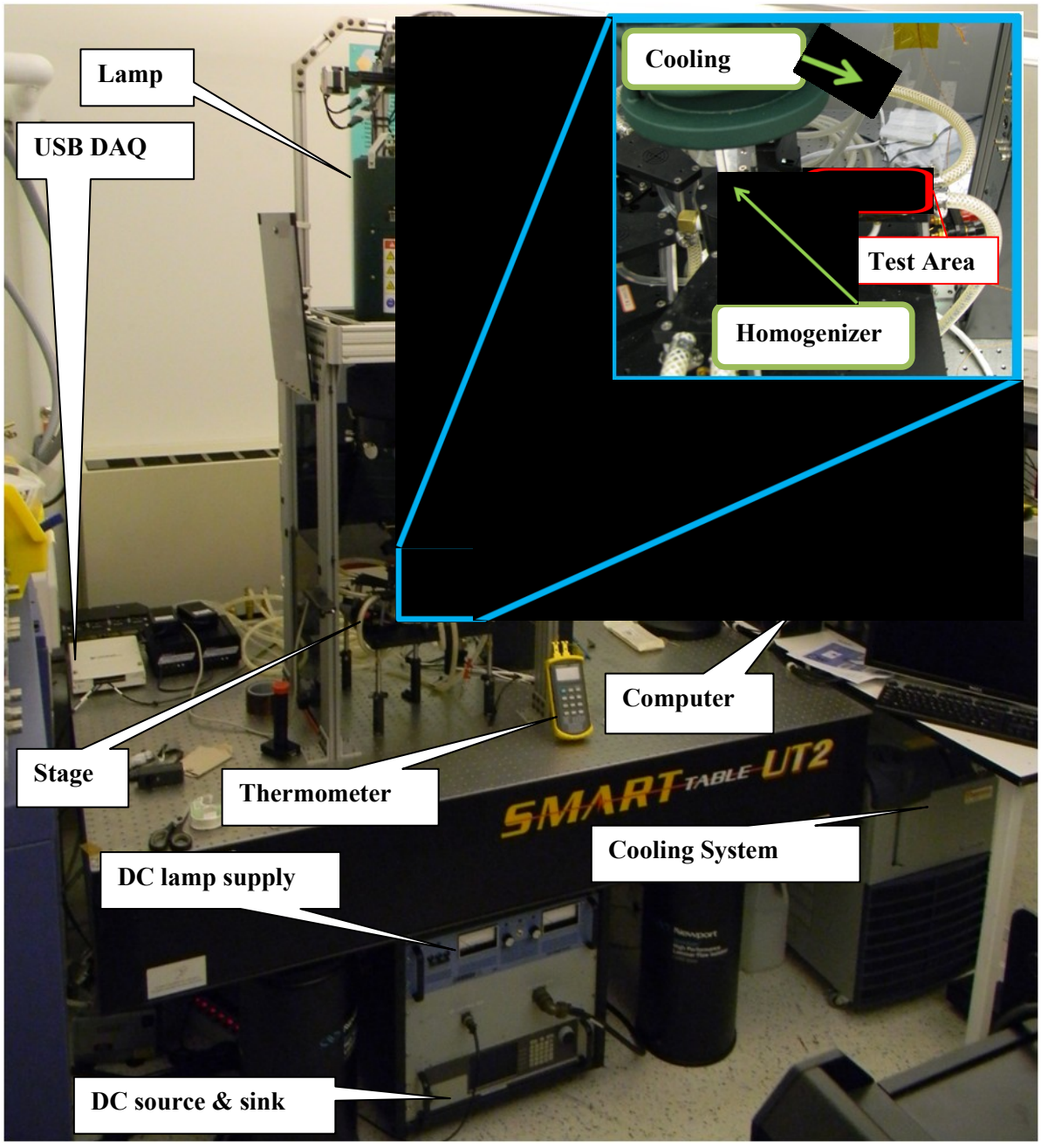

Figure 25 Picture of the XT-30 solar simulator system.

3.3.1. Motion control

The source lamp is physically connected to a motorized slider on top controlled by two servomechanism controllers as shown in Figure 26. The servomechanism controller is

connected to both an analog joystick and a computerized digital controller. Positioning the lamp to properly illuminate the solar cell can be done with the manual joystick or by inputting coordinates via the computer.

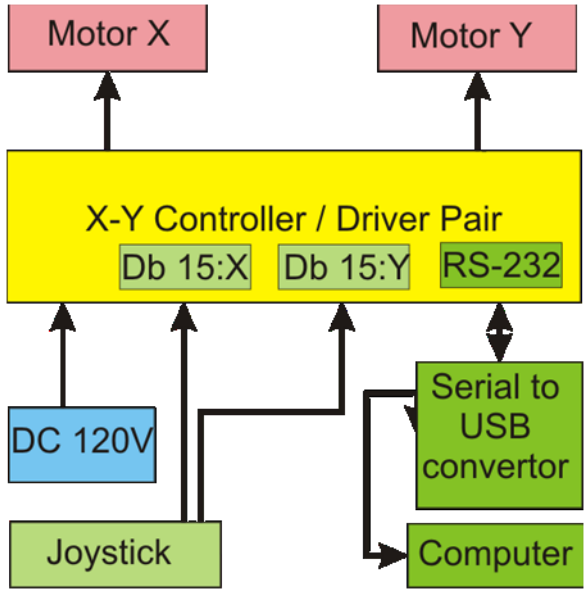

Figure 26 Wiring diagram for lamp motion control of XT-20 and XT-30 solar simulators.

3.3.2. Power station

The power station is composed of two major components, a Sorenson DLM32-95E DC voltage supplier for the XT-20 and a LAMBDA EMS 40-125-2 power supply for the XT-30, a junction box and the lamp as shown in Figure 27. The Sorensen and the LAMBDA provide stable, continuous DC voltage along with adjustable voltage and current output at a given range to the lamp. The input for the voltage supplier is a 3-phase 240 V AC. The output ratings for both voltage and current of the Sorenson are 0-35 V and 0-95 A with accuracy of ±0.3 V and ±0.8 A. The output ratings for the LAMBDA are 0-150 V±0.1% and 0-40 A±0.1 A. The maximum output power is 3040 W for the Sorenson and 5000 W for the LAMBDA. The junction box connects between the lamp and the voltage supplier.

There are two fuses inside the XT-20 junction box which limits the maximum current supplies to 70 A (lamp) and 5 A (fan).

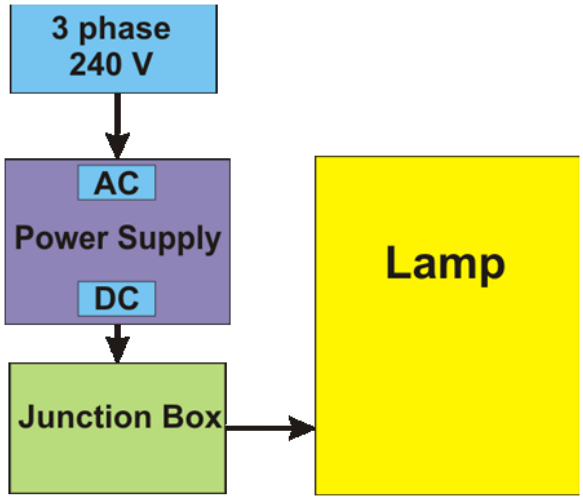

Figure 27 Connection diagram between source and lamp of XT-30.

3.3.3. Characterization

The characterization apparatus of a solar device includes a Kepco DC source and sink unit, a National Instrument (NI) universal serial bus (USB) data acquisition (DAQ) unit, a computer and the device under test (DUT) shown in Figure 28. The Kepco unit is a programmable 4-quadrant voltage and current power supply. 4–quadrant operation represents the capability of both sourcing and sinking power. Given the unique ability of the Kepco power supply it is used in the characterization process. The rating of the Kepco BOP 10-75MG is ±10 V and ±75 A. Both the Kepco and the NI DAQ units are directly connected to all remaining devices. The NI DAQ USB-6259 is capable of both analog and digital input/output. The maximum sampling rate for a single channel input is 1.25 MS/s and each sample has a resolution of 16 bits. A four point measurement setup is used to minimize the contact resistance when characterizing the solar cell. The Kepco source measures the current from the DUT while varying the input voltage using two probe connections and delivers the results to the DAQ unit. The NI DAQ unit measures the voltage of the DUT and redirects the readings to the Kepco for voltage adjustments.

Secondly the NI DAQ unit samples and digitizes both current and voltage measurements from the DUT, and the Kepco relays the digitized data to the computer for display and recording.

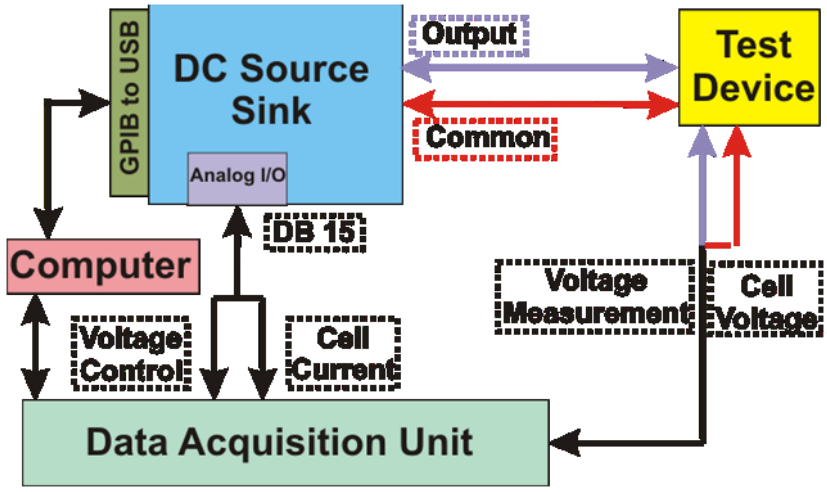

Figure 28 Connection diagram of current-voltage tester of the XT-30 and the XT-20 solar simulator

3.3.4. Cooling

Spectrolab's solar simulator utilizes both air and water cooled refrigeration capabilities as shown in Figure 29. On the top of the lamp module a fan was installed and provides cooling for the lamp bulb, parabolic reflector, AM 1.5D filter and electronics inside the lamp module. The Neslab water cooler was used to transfer heat from the cone module and stages where the DUT is placed on top of a stage during characterization. The rated cooling capacitance for the water chiller is a function of temperature set-points with respect to ambient room temperature as shown in Figure 30. The cooling capacity is the rate of heat removed from a medium. The unit is generally in Watts or British Thermal Units (BTU) and one BTU is based on the amount of energy to raise the temperature of a pound of water by one degree Fahrenheit. The chiller employes a positive displacement pump capable of

operating at 50 or 60 Hz pump frequency and at 60 Hz the pump is able to output 2.1 gallons of water per minute at 60 pounds per square in differential.

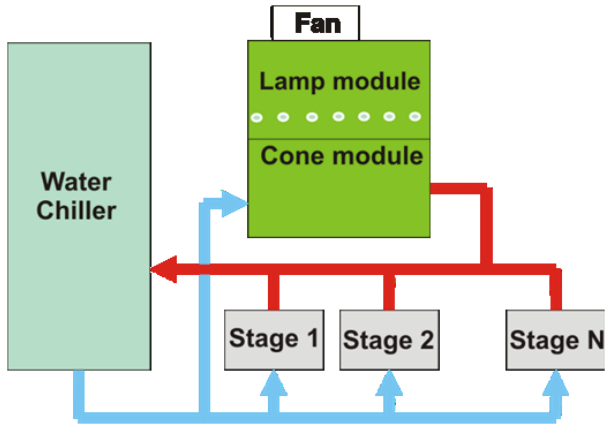

Figure 29 Cooling diagram for the Spectrolab XT-20 and XT-30 solar simulator systems.

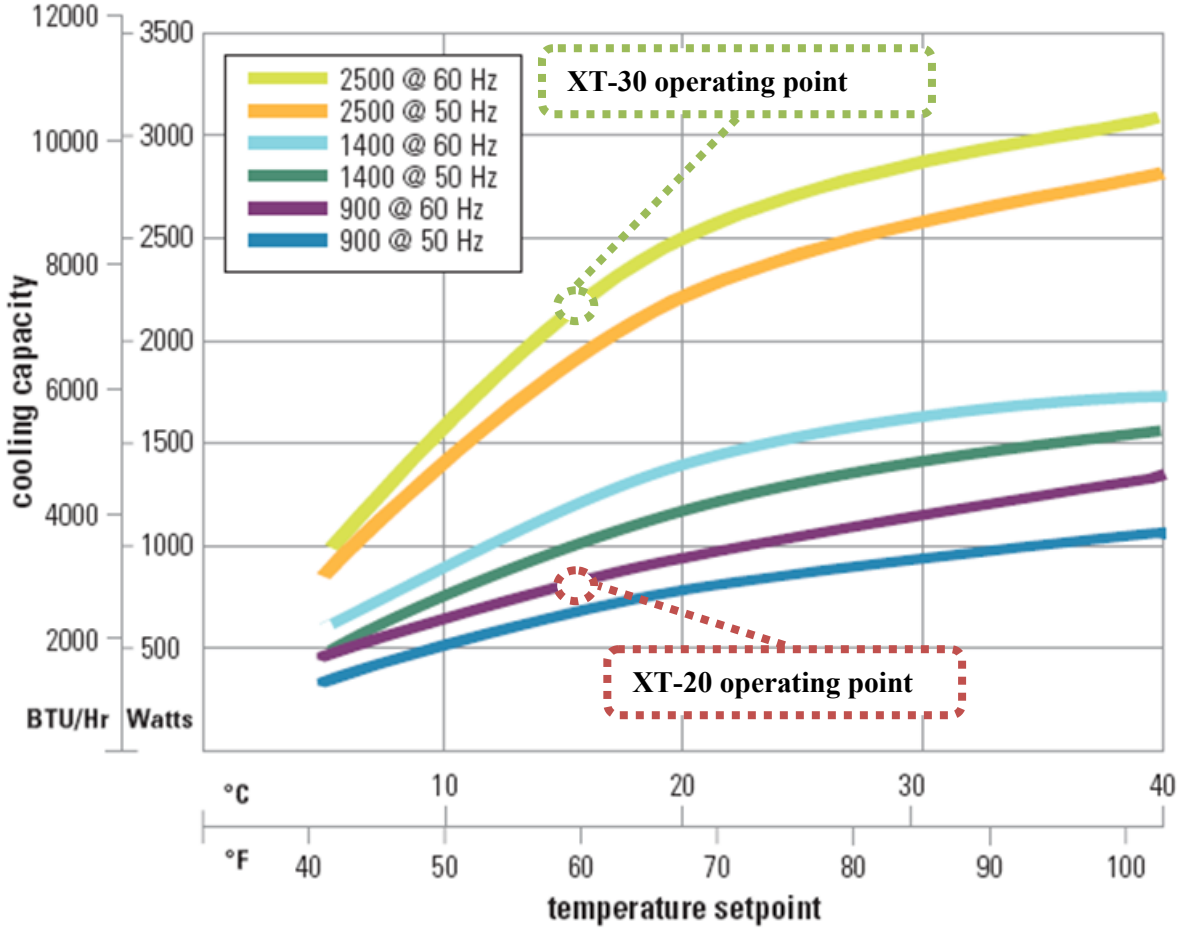

Figure 30 Cooling capacity of the ThermalFlex water chiller employed by the Spectrolab XT-20 and the XT30 solar simulator systems [41].

3.3.5. Test platform

Solar devices (DUT) under characterization are to be placed on the platform stage shown in Figure 31. The platform can scale up to 12 stages for testing. Stages on the platform are linearly connected to the liquid cooler. Stages specified for receiver and solar cell characterization have both a vacuum hole and trenches. Vacuum holes are connected to a central pump. Both holes and trenches contribute on fixing the device position.

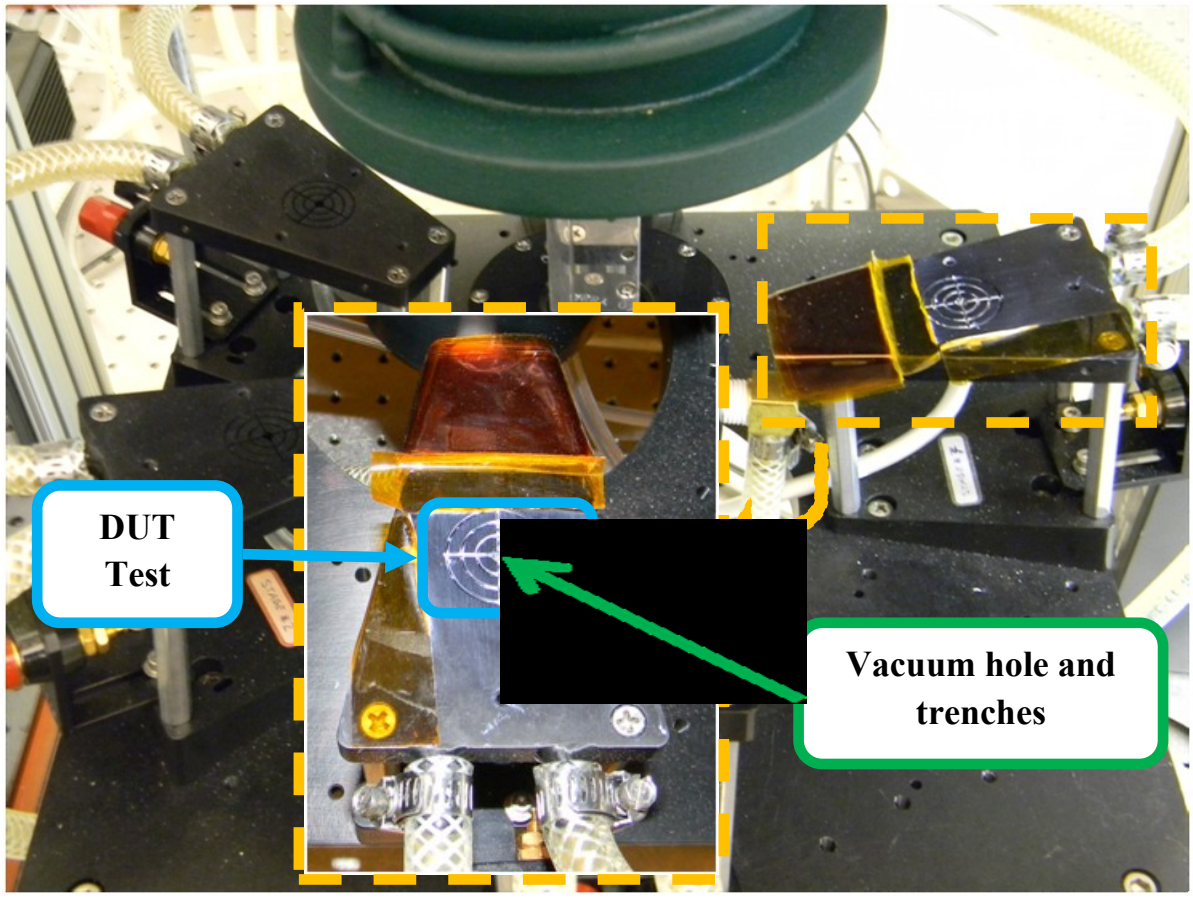

Figure 31 Overhead view of the testing platform of the XT-30 solar simulator system.

3.3.6. Receiver design

In order to test solar cells at concentrations above 20X they must be mounted on carriers to minimized heating issues. Solar devices chosen for characterization are carrier receivers designed and fabricated by both academic and industrial collaborators. Receivers undergoing tests include solar cells, external connectors and protective diodes attached as shown in Figure 32. Carrier geometry, receiver material and diode type for different designs are listed in Table 2.

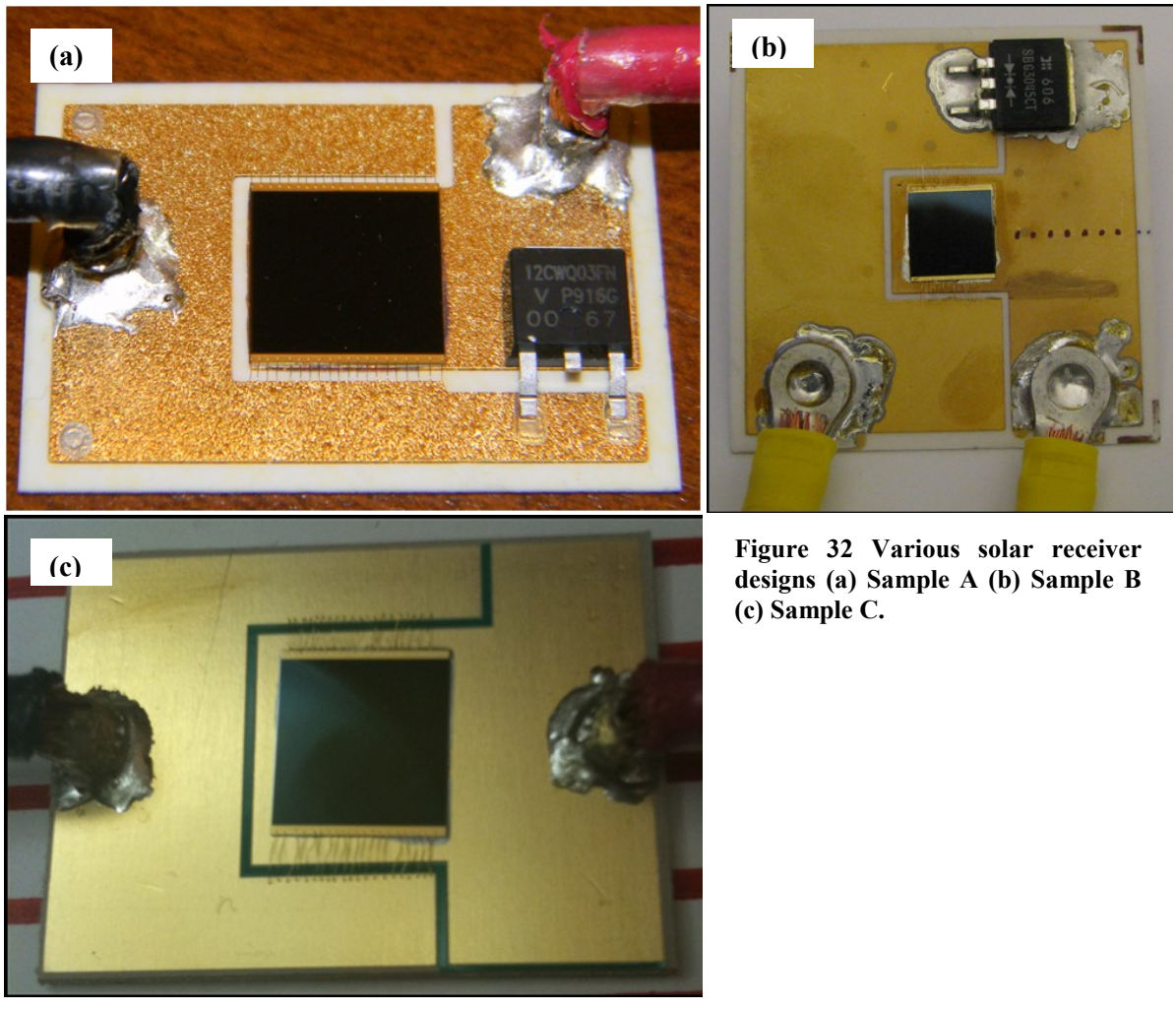

Figure 32 Various solar receiver designs (a) Sample A (b) Sample B (c) Sample C.

Parameters	Sample A	Sample B	Sample C
Overhead (Ceramic)	35 mm*25 mm	50 mm * 50 mm	35 mm * 25 mm
Copper Substrate thickness (µm)	~200	25	35
Diode	12CWQ03FN	3RB20100CT (10A)	STPS41L30CG (20A)
Channel Design	L shape	Hat shape	Hat shape
Thermal Conductivity of the ceramic layer (W/m/K)	24	24	0.78
Ceramic Material	Alumina	Alumina	RT/duroid 6010
Ceramic Thickness (mm)	0.35	0.625	1.27
External Connector	Soldered Cable	Pin Connector	Soldered Cable

Table 2 Receiver design parameters.

Typical solar cells have one metal contact on the top and the opposite contact at the bottom. The bottom of the solar cell must be electrically connected to the other cells' top for series connection or to external circuitry. The solar cell receiver is part of the external circuit which enables series connectivity between solar modules in an array. Each carrier used for tested receiver employs a different fabrication process. Sample A carrier is a DBC substrate and it is widely used in power modules due to its high thermal conductivity. A sheet of copper is bonded to one or two sides of a ceramic sheet by a high temperature oxidation process where both copper and ceramic are heated in a temperature controlled nitrogen atmosphere. When an optimal temperature is reached, a copper-oxygen eutectic forms and bonds the copper to the ceramic. Sample B carrier is fabricated using a highly conductive metallic layer screen printed on a ceramic substrate inside a heat chamber controlled at 1123K. Sample C carrier is an off the shelf component where a thin copper sheet is laminated on both side of the ceramic substrate. Both sample A and C are patterned by chemical etching whereas a mask is implemented on sample B during screen printing. The pattern is specifically designed to separate the anode and cathode electrical connection between the solar cell and the external circuit.

3.3.7. Lamp

The Spectrolab XT-30 is a high concentration continuously illuminated solar simulator. The lamp used by the solar simulator is a 3 kW Xeon arc lamp that provides illumination intensities of up to 1000 suns with high thermal loading. It is well understood that spectral mismatch occurs between actual sun light and a solar simulator [42]. The output of the solar simulator at the tip of the metallic hollow homogenizer has a class rating of AAA (spectrum, uniformity and stability) as defined by the manufacturer. The reference spectral distribution of sunlight in North America is defined in the ASTM G173 standard. For classification of solar simulators, the corresponding standard, ASTM E927, is restricted to wavelengths from 400 to 1100 nm which is generally suitable for testing silicon based solar cells. The ASTM E927 classification for solar simulator is shown in table. The overall absorption range for triple-junction solar cells is from 300 to 1800 nm. The spectral mismatch between the ASTM E927 standard and the absorption range of the triple junction solar cell mainly takes place in the infrared region. Both the lamp module of the XT-30 and the Oriel solar simulator includes an AM1.5D filter specifically designed for concentrator multi-junction PV cell testing which allows a controlled infrared spectrum as shown in Figure 33.

Characteristic	A	B	C
Non-Uniformity	$\pm$<2%	$\pm$<5%	$\pm$<40%
Spectral Mismatch	$\pm$25%	$\pm$<40%	>$\pm$25%
Temporal Stability	<2%	<5%	<10%

Table 3 ASTM E927 classification for solar simulator

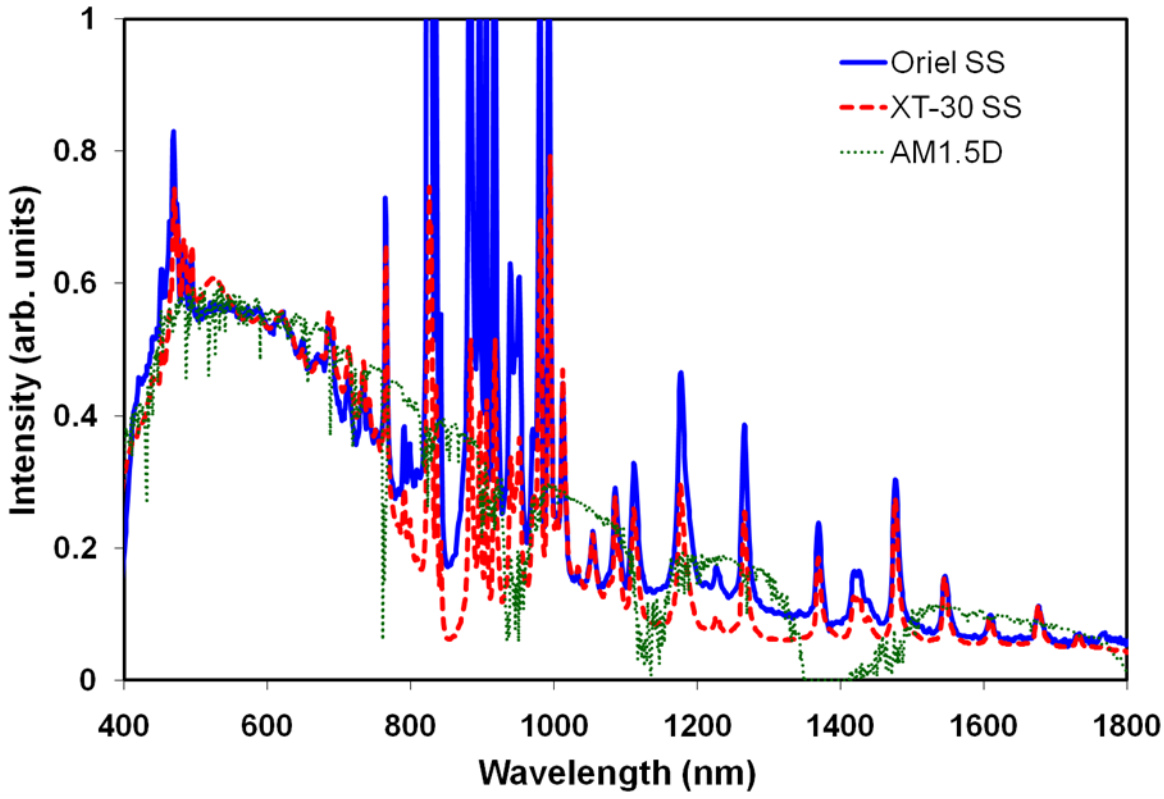

Figure 33 Normalized spectra of the high concentration XT-30 and low concentration Oriel solar simulator compared to the terrestrial AM1.5D standard. (Data courtesy of Olivier Theriault, SUNLab).

The lamp lifetime is closely related to the application and environment in which the lamp is used. Pulse and continuous simulators are generally used in indoor solar cell characterization and a pressurized Xe lamp can be found in most solar simulators. The pros and cons of pulse and continuous simulators have been extensively compared [43]. In addition, the emitting spectrum of a Xe lamp shifts from blue to red during the lamp life. The spectral shift takes place during the first 100 hours of operation [44]. The lifetime for a pulse lamp is normally measured in terms of total number of flashes and the lifetime for a continuous arc lamp is measured by the number of operating hours. The maximum number of flashes or hours is determined by the intensity of the lamp required for particular application. The XT-30 solar simulator powers an OSRAM manufactured XBO 3000W/H XL OFR Xe arc lamp with voltage and DC current ratings of 29 V and 100 A respectively. Current control ranges of the Xe lamp vary from 60 to 110 A with average luminance of

90000 cd/cm^2, and the lamp's expected life is greater than 2200 hrs. The concentration as a function of time of a 1600 W Xe arc lamp is shown in Figure 34. The lamp intensity measurements were taken by a triple junction cell before experiments and the lamp concentration results were recorded. In Figure 34 the lamp intensity has shown a decaying rate of ~0.5 sun/lamp-hour usage. Based on the decaying rate observed, the lamp shall reach zero concentration after 600 hrs which is much shorter than the manufacturer rating of 2200 hrs. The red spectral shifts in lamps maybe the solution to the solar simulator degradation where less ultra violet radiations are produced by the lamp. With lesser ultra violet radiation upon a triple junction cell causing lesser current produced from the top cell, the concentration measurement of the lamp from a calibrated triple junction cell is lower.

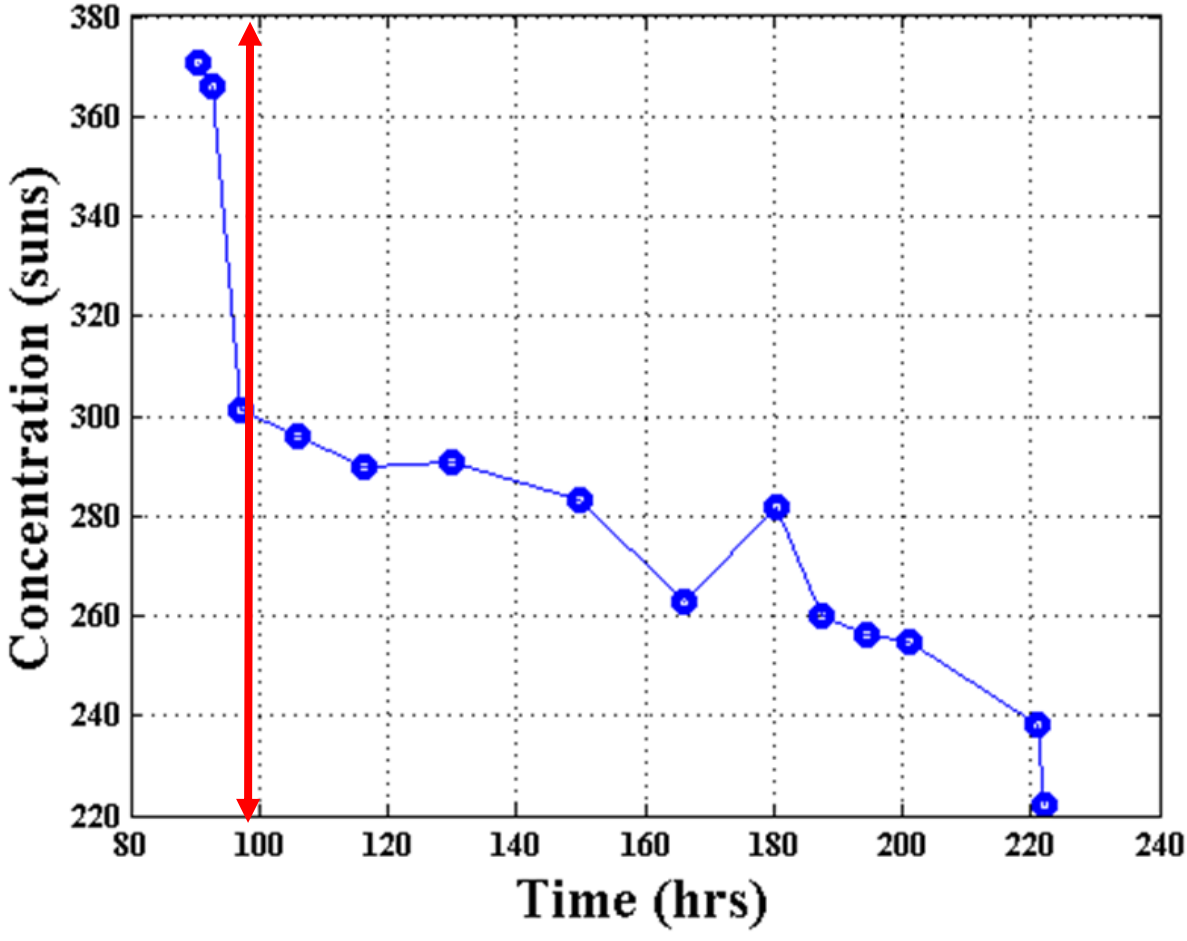

Figure 34 The solar concentration as a function of time of a Xe 1600W arc lamp in a continuous Spectrolab solar simulator. The red line indicates the time of the installation of an AM1.5D filter.

At the lower tip of the lamp module is the metallic hollow homogenizer. The homogenizer takes the light produced by the Xe lamp and releases a uniform square output onto the test device. The concentration of the output relies on the size of the homogenizer which is interchangeable. The simulator system is designed to have a very short working distance and the optimum operating distance is null between the homogenizer and the test device for best spatial uniformity. The spatial uniformity of the 1 cm^2 homogenizer with varying illuminating distance is shown in Figure 35. The maximum non uniformity allowance for a class A solar simulator is less than 2% which is approximately 0.25" spacing between the homogenizer and the chuck.

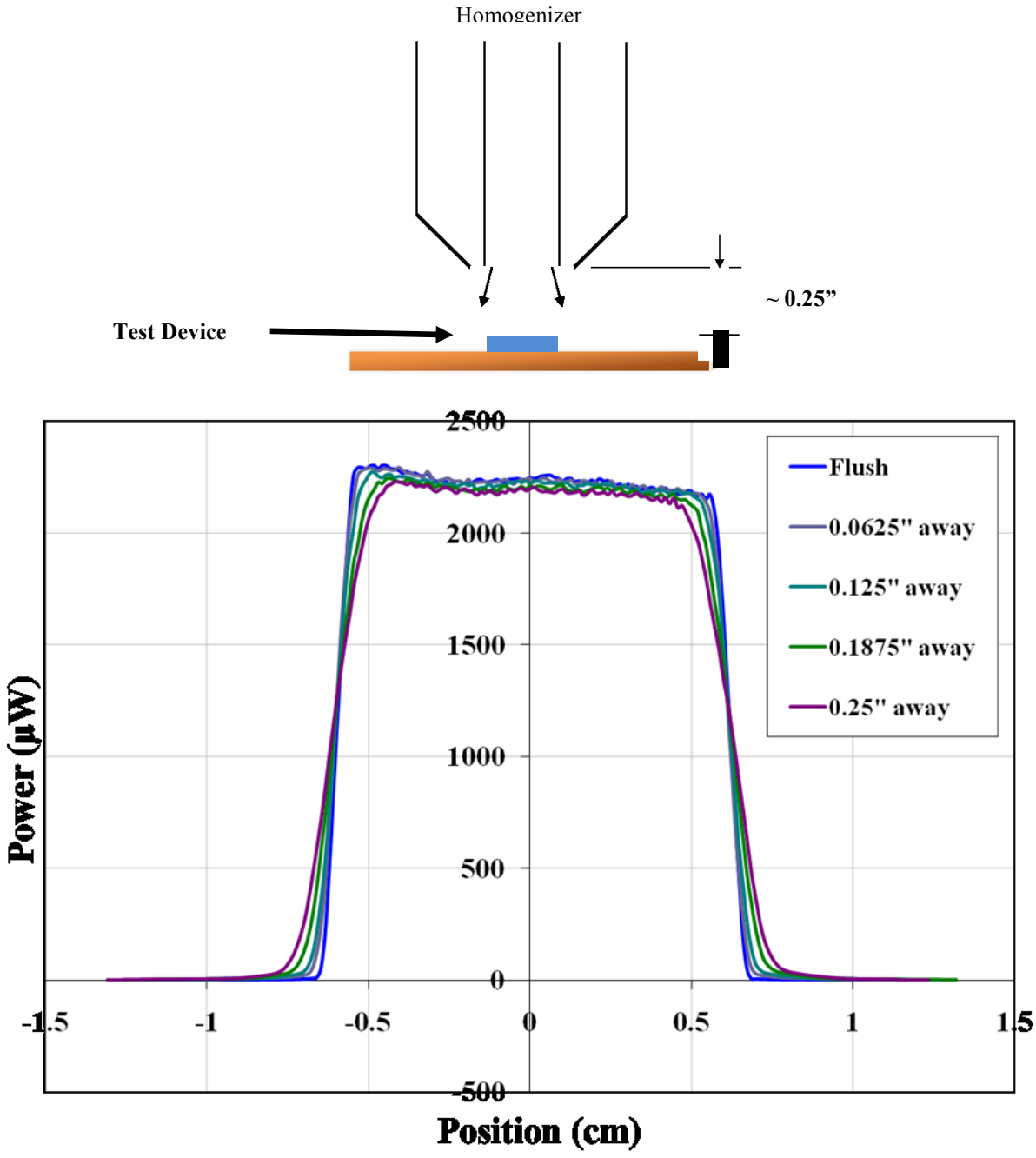

Figure 35 Radiation intensity and beam shape of a 1 cm^2 homogenizer. The light illuminated from the homogenizer on a 1 cm^2 as a function of distance the homogenizer and the test device [45].

3.3.8. Temporal and positional effect

Solar device characterization by a continuous solar simulator is subjected to both temporal and positional effects. Temporal effect refers to the warm up time required for a

solar device under illumination. It is unnecessary to consider the warm up time when the solar cell is illuminated by a flash simulator for a short duration. With less than a second of light exposure the solar cell temperature remains constant. However under continuous illumination by the XT-20, the temperature of the solar cell increases with time until saturation. An increase in temperature reduces the V_{oc} and 10 seconds is the required warm up time for a test device under the XT-20's continuous illumination, as demonstrated in Figure 36.

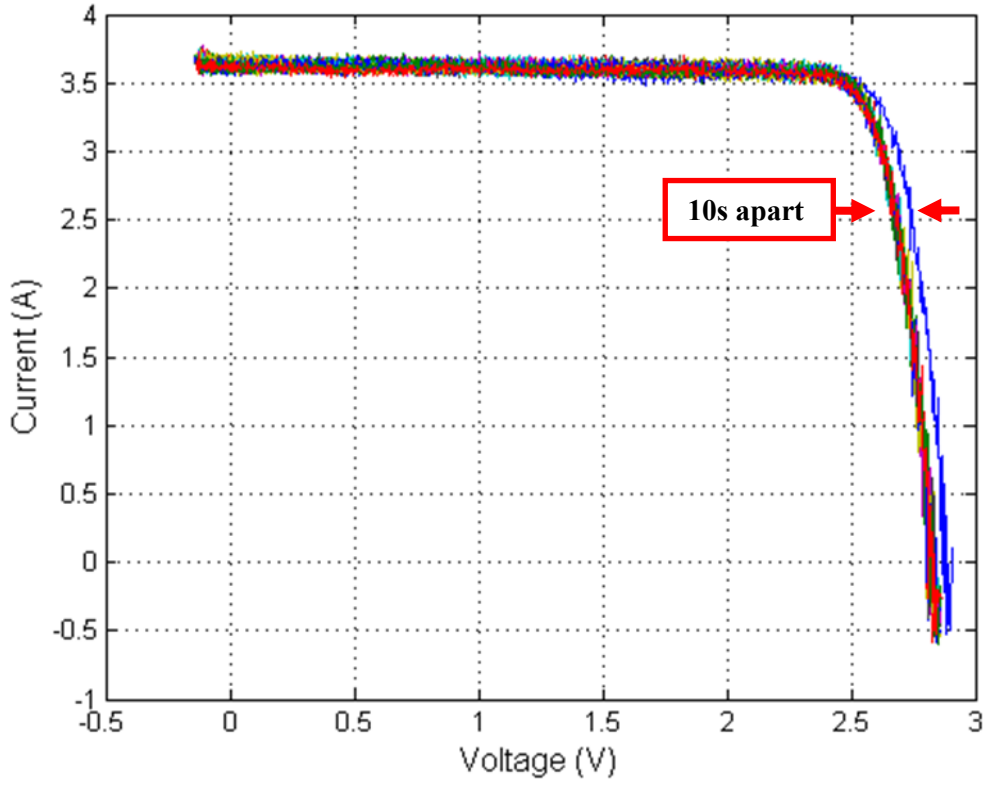

Figure 36 Repeated IV characterisation on a chip on carrier receiver with a period of 10 second separation between each test using the XT-20 solar simulator under 250 suns intensity. The first set of data taken at 0 seconds is denoted the blue line at farthest right.

Positional effects correspond to the cell placement on the chuck. During the process of die attachment between the solar cell and the carrier, the solar cell may vary ± 1 mm away from the center of the carrier. In addition, the positioning of a receiver on the chuck may also be off-centre. Fortunately the lamp positioning from the XT-30 is computerized where

the illumination area is fixed relative to the chuck. To better understand the solar cell positioning and fixed illumination from the lamp, a receiver was placed on the chuck. By varying the receiver ± 1.5 mm away from the center of the light mask, V_{oc}, I_{sc} and FF data are obtained as shown in Figure 37. It seems a small misalignment between the light area and the solar cell of ±1.5 mm has minimal impact on experimental results.

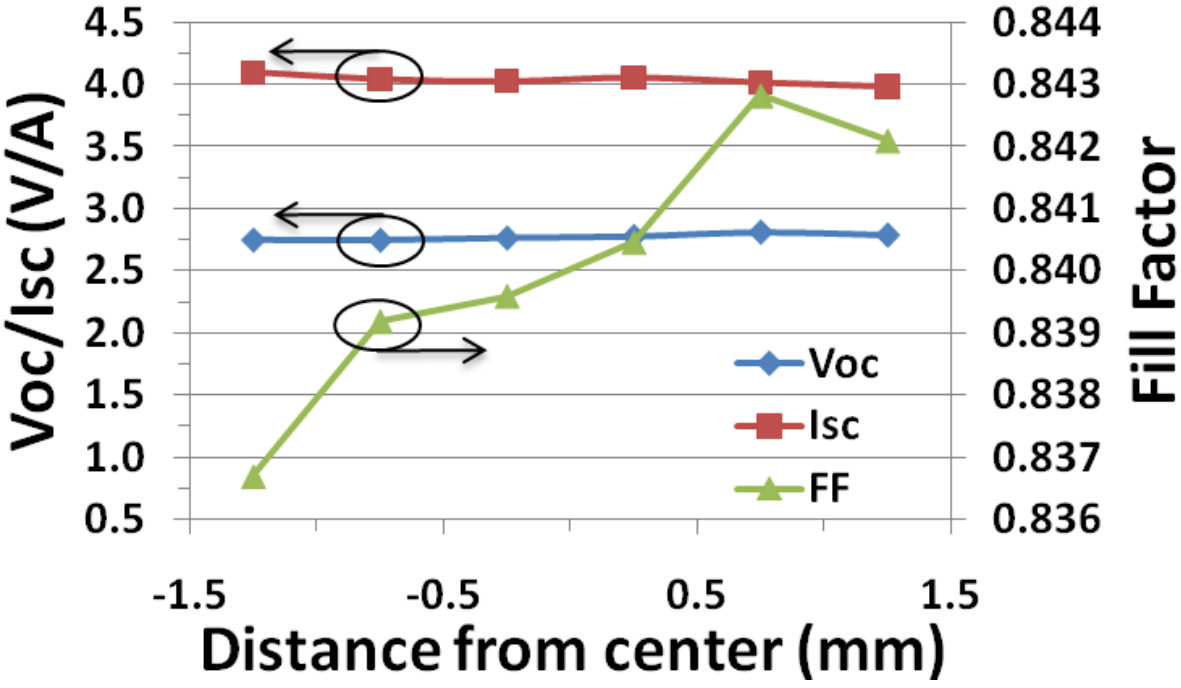

Figure 37 Time averaged plot of a triple junction solar receiver with various illuminating positions centered from the middle of the solar cell. Illumination was calibrated to 250 suns. Lines between data points are guide to the eye.

3.4. Flash testing

Solar cell flash testing was performed at a Cyrium technologies Inc. Packaged cells are tested using the Sinton HCCT flash simulator system as shown in Figure 38. The Sinton system employs a Xe lamp capable of producing 1000 suns output. A homogenizer is

attached to the bottom of the lamp and the output is a class A spectrum (as claimed by the manufacturer). The solar cell or receiver is placed on the top of a temperature controlled chuck. The temperature control is accomplished by resistive heating within the 25 – 40°C range. The variable concentration upon the test device is achieved by adjusting the distance from source to cell through an arm elevation connecting to the lamp. Solar cells are connected to a characterization system and one current value can be obtained from one flash. Multiple flashes are required to construct a current-voltage plot. The pulse duration for each flash is ~2 ms and the recovery time for each flash varies from 2 - 6 s. Device characterized by a flash simulator suffers from minimum heat. Hence the results are thermally independent to concentrations compared to the results from a continuous solar simulator.

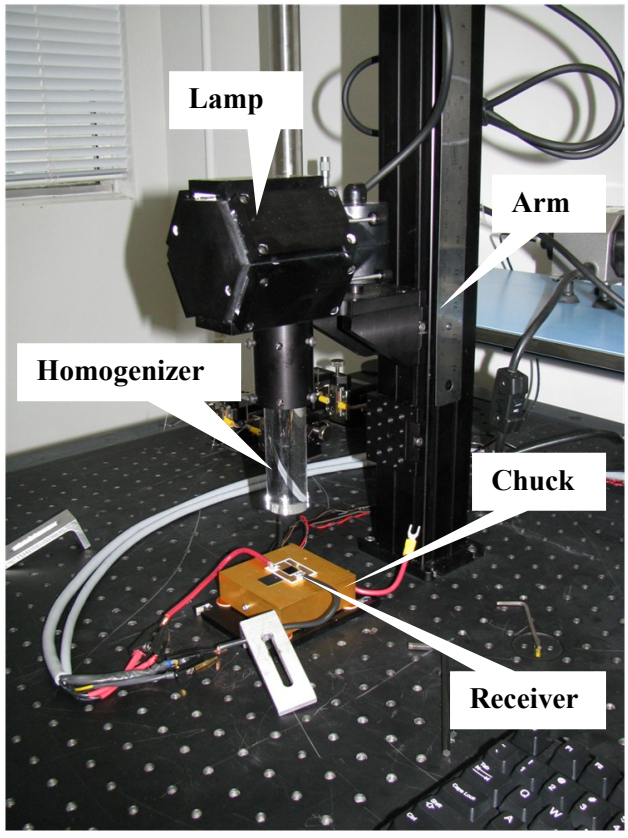

Figure 38 Figure Picture of a Sinton HCCT flash solar simulator system.

3.5. Simulator calibration methodology

The purpose of an indoor solar simulator is to provide an accurate reproducible optical spectrum for characterizing solar cells. The concentration of a solar simulator depends on the total amount of light illuminating the solar cell. The amount of concentration can be determined using the total current produced by the solar cell at the short circuit level. However the current density of a solar cell at one sun, excluding the area proportion, is quantum efficiency dependent. Hence characterizing the intensity must take test cells into consideration. A more accurate approach to characterizing the intensity of a solar simulator is by having a reference cell, of similar quantum efficiency as the test cells, calibrated at an external testing laboratory by universal standards. The externally calibrated solar cell has the same spectral response as the test cell and the concentration alignment between the test and the reference cell under a same solar simulator is then much closer in reality.

Two methods have been investigated for calibrating the simulator concentration, type A and type B respectively. Type A calibration involves a 0.25 cm^2 triple junction solar reference cell, an earlier and similar model relative to the test cells, calibrated by the National Renewable Energy Laboratory (NREL), USA. The current density was determined to be ~14.4 mA/cm^2 at one sun and was cross calibrated with one of the test cell for redundancy. The current density was determined to be 13 mA/ cm^2 and was used throughout the tests on the intensity calibration of the Oriel and the XT-30 solar simulator systems.

Type B calibration uses the current density provided by the multi-junction cell manufacturer where the given current density for one sun from the manufacturer is calibrated by a silicon reference cell. The current density used for the Oriel, Sinton and the XT-30 intensity calibration was ~14.1 mA/cm^2 at one sun given a 1 cm^2 die.

Figure 39 and Figure 40 display the current density calibrated by type A and type B respectively on various level of sun concentration. The measured Oriel, Sinton and XT-30 values methods are shown in blue, red and green. Their fitted projections are in solid lines. Ideally a perfect match should reveal overlapping of the current density between all three models in both Figure 39 and Figure 40. A perfectly matched concentration calibration between solar simulators results in smaller errors when comparing the V_{oc} and the efficiency of solar cells as a function of concentration between solar simulators. The spectral mismatch between the three simulators may be one of the factors responsible for the slight current mismatch observed from both type A and B calibration methods. Type B calibration from Figure 40 shows more current density convergence than type A calibration.

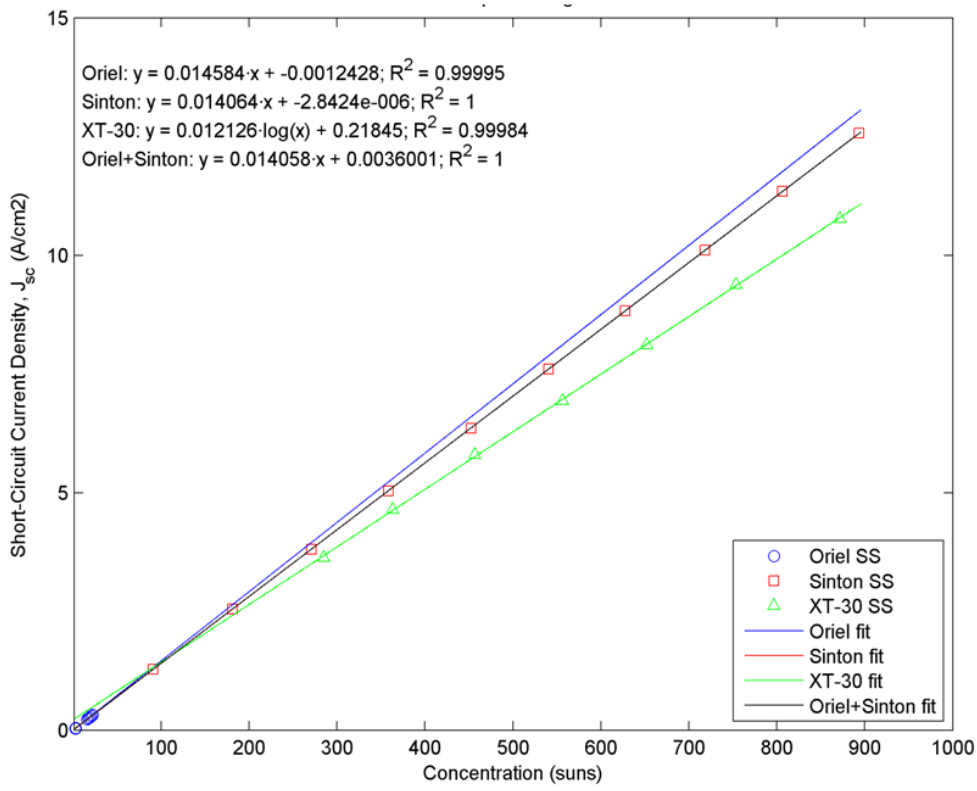

Figure 39 Short circuit current density as a function of concentration using type A calibration.

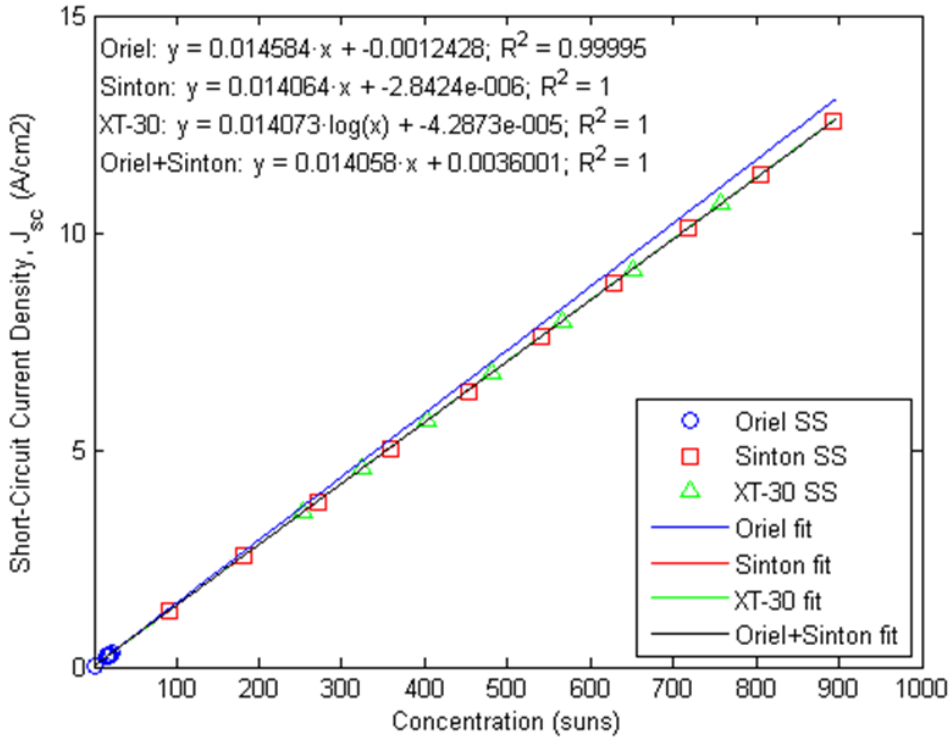

Figure 40 Short circuit current density as a function of concentration using type B calibration.

3.6. Conclusion

This chapter introduced the solar simulators used in determining the experimental results, test device structure and simulator concentration calibration methods.

The Oriel continuous simulator is capable of producing 20X concentration and is only suitable for low concentration solar cell characterization. The XT-30 high power continuous solar simulator with higher focusing ratio is capable of simulating concentration up to 800 suns. Although both pulse and continuous solar simulators have been standardized in the past, one must recognize that the standards are based on silicon devices. In MJ concentrator cells, where the absorption spectrum is greater in the infrared region than silicon cells, the existing standards may not accurately reflect the emitting power and spectrum of a solar simulator. An investigation into the intensity degradation of the high power XT solar simulator with time shows the result of -0.5 sun/hours.

Solar receivers subjected to continuous high concentration require a 10 second warm up time before acquiring any characterization results. Positioning a device on the chuck relative to the light position was studied. The investigation shows a $\pm$1.5 mm variation in device positioning outputs with similar results.

Two methods were used in determining the concentration of solar simulators; the first involved a bare MJ solar cell calibrated by NREL and the second made use of the current density at one sun obtained from the cell manufacturer. Results show the latter method resulted in better matching between Oriel, Sinton and XT-30 in current density and concentration alignment.

Chapter 4 Experimental results

4.1. Introduction

This chapter introduces the characterization of a MJ solar cell receiver under high continuous concentration. Characterization includes the electrical performance of the concentrator cell receivers and the surface thermal behaviour of a receiver. Results presented in this chapter are used in chapter 5 for simulation model calibrations.

Concentrator cell receiver characterization is the resulting performance of a concentrator cell mounted on a carrier. The initial characterization data obtained from chapter 3 is originally a set of current data corresponding to its voltage under continuous concentration. Initial data are then analysed and reviewed in the following sections. Three individual designs are chosen for testing. However as concentration increases during illumination some test devices are rendered inoperable and we are unable to obtain any useable data for the analysis.

4.2. Characterization

Data collected from samples are analysed and important parameters such as open circuit voltages, short circuit currents and receiver efficiencies are extracted in terms of concentrations. Test results show the impact of variables such as the presence or absence of thermal paste, as well as various input intensity calibrations.

The V_{oc} of the receiver is the maximum available voltage when the generated current is zero. The behavior of a concentrator receiver inherits the diode characteristics of a solar cell where the V_{oc} increases with logarithmic behavior as illumination power increases.

However the logarithmic increases in V_{oc} are limited by the metallic top contact designs where the bus-bars and fingers are located. Various contact designs are investigated by Serreze [47]. As the width of grid elements on the top of the cell increases the electrical series resistance decreases. However the optical path shadowing increases causing the photocurrent generated by the cell to decrease. A good top contact design optimises the cell current collections with low internal resistance loss and optical path shadowing. Efficiency of a concentrator cell increases primarily as a result of V_{oc} increases under higher illumination. Concentrator cells used in sample receivers have unique top contact designs with low series resistance (~0.01 Ω), and the optimized efficiency of 41% is ranged from 500 to 700 concentrations when flash tested at room temperature [48].

Solar simulator intensity calibration methods discussed in chapter 3 are used in the following sections. The two methods used are type A and type B. The current density for type A reference cell is cross calibrated by a NREL solar cell whereas type B uses the related current density given by the cell manufacturer.

A solar cell receiver illuminated by a high power continuous simulator undergoes two testing conditions. The first is by placing the receiver on a chuck with vacuum hold only and the second condition is introducing a thermal paste coupled between the receiver and the vacuumed chuck. In real world applications, receivers are typically soldered on a passive heat exchange, using a silicon thermal compound as a replacement during tests to resemble the soldering condition. However the thermal conductivity used in the test has only ~3 W/m/K which is a fraction of a typical $Sn_{96}Ag_4$ solder of 78 W/m/K. Ideally, thermal management should improve with the addition of a thermal compound and results are demonstrated in the following sections.

4.3. Current-voltage characterization

The current-voltage characterization of a solar device reveals the efficiency, FF and maximum power available under fixed illumination. A common laboratory characterization method of a solar device makes use of a parameter analyzer. The analyzer is capable of providing known voltage and measuring the resulting current or vice versa. To measure the current-voltage characteristics of a solar device under illumination, the analyzer is stepped through various voltage input levels and the corresponding output current is measured. The combined current-voltage measurements are drawn into a graphical representation named current-voltage plot.

Figure 41 demonstrates the current-voltage characteristics of a sample A receiver under various illuminations by an XT-30 solar simulator. The current-voltage measurements from ~275 to ~775 suns show increasing I_{sc} from the blue to the black curve. The coupling between the receiver and the heat sink was varied by using a vacuum hold only, as shown in Figure 41a, or both vacuum plus thermal conductive paste between the vacuum chuck and the receiver, as shown in Figure 41b. Without the thermal paste application, the same receiver possesses a lower heat transfer coefficient from the bottom of the receiver to the heat sink. At low concentration (275X), the receiver suffers from a lower initial V_{oc}, ~2.9 V, whereas the V_{oc} of thermal paste used is ~3.0 V. It shows the receiver operating temperature is lower than with the application of thermal paste. At high concentration (775X), the V_{oc} of the receiver without using thermal paste drops by ~0.2 V and under the same concentration the V_{oc} of the receiver using thermal paste drops only by ~0.05 V. Since the cell operating temperature is reflected by the V_{oc}, the cell operating temperature of a receiver without paste is much lower than with paste. In addition, the I_{sc} of using thermal paste is ~0.2 A lower than without using the thermal paste. The power produced by a solar receiver with no thermal paste is lower compared to the use of thermal paste due to due to the temperature increase of solar cell on the receiver.

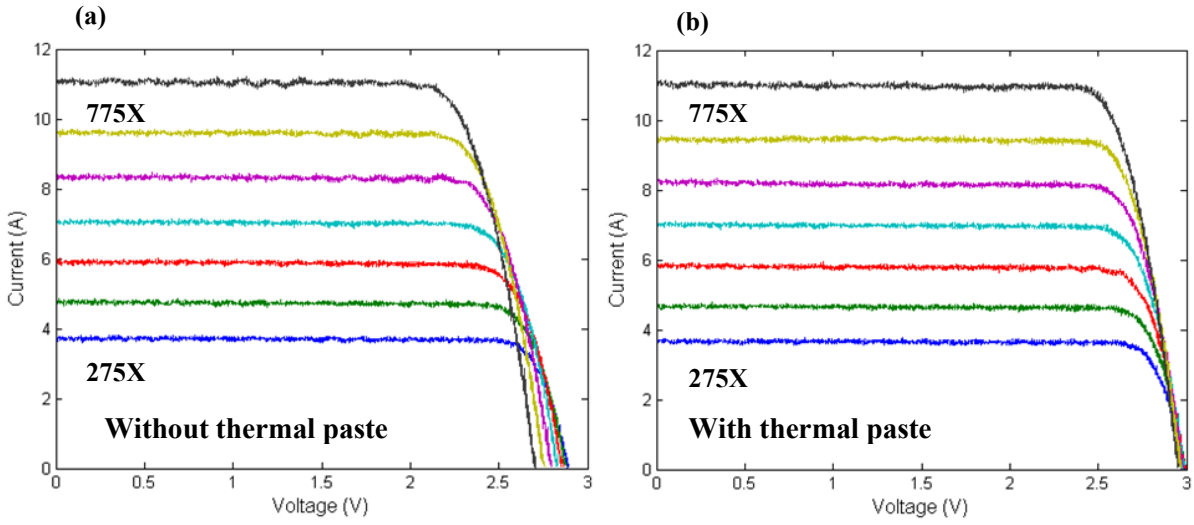

Figure 41 Sample A test device current-voltage behaviour (a) without and (b) with thermal paste coupling between the receiver and the heat sink.

Figure 42 shows the current-voltage characteristics of a sample B receiver. The illumination ranges for without thermal paste is from 261 to 713 suns and with thermal paste is from 261 to 425 suns. Sample B receiver rendered inoperable beyond 425 suns illumination with thermal paste. Hence, no further experimental results recorded beyond 425 suns concentration. At low concentration, 261 suns, the initial V_{oc} without paste and with thermal paste are ~2.7 V and ~2.8 V respectively. From the current-voltage plots of sample B, we again obtain confirmation that the use of thermal paste reduces the rate of reduction of V_{oc} with increasing solar concentration.

The concentrator solar cells mounted on both sample A and sample B receivers are fabricated using a very similar design but come from separate wafers. Both sample A and sample B receiver has various physical geometries and thickness. Sample B has larger overhead size and sample A has thicker copper layer. The V_{oc} and I_{sc} for sample A bare cell under 480 suns flash testing is 3 V and 6 A and for sample B bare cell under 500 suns illumination is 3 V and 6.3 A. Both sample A and B bare cells have similar V_{oc} and I_{sc} value.

Since concentrator cells A and B are mounted on sample A and sample B carriers, the current-voltage performance of the sample A (Figure 41), and B (Figure 42) receivers can be compared based on similar cell design. The decreasing rate of V_{oc} of sample B is greater than sample A on both paste and without paste conditions under similar concentration increments. This implies that the sample B receiver design has a lower thermal conduction cooling rate than sample A.

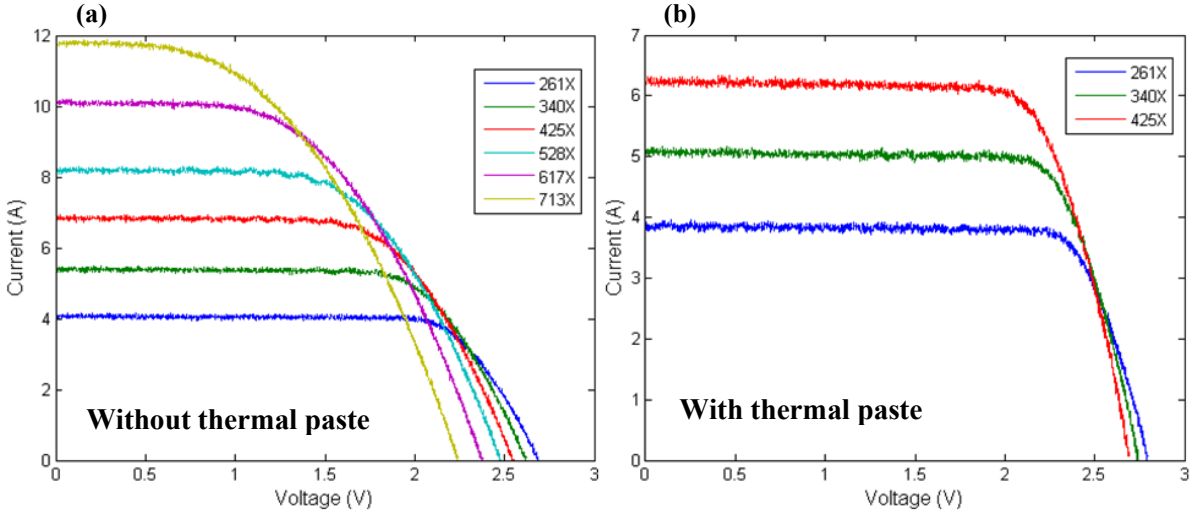

Figure 42 Sample B test device current-voltage behavior (a) sample B1 without and (b) sample B2 with thermal paste coupling between the receiver and the heat exchange.

4.4. Open circuit voltage mapping

The intensity calibration of a solar simulator is performed by aligning the current density of a standardized solar cell, as discussed in section 3.5. Two unique calibration methods, type A and B, are employed in determining the V_{oc} and the efficiency of a solar receiver over a span of illumination concentration. Both methods involve a second receiver aside from the test devices and it is used to measure the concentration of the lamp before experiments. The I_{sc} from the second receiver is divided by the current density at one sun to obtain the concentration. The current density at one sun is different from, type A, current density at one sun cross calibrated with NREL and, type B, current density at one sun given by the cell manufacturer.

Figure 43 shows the V_{oc} under type A calibration of a sample A receiver tested by the low power continuous Oriel, the high power continuous XT-30 and the flash Sinton solar simulators. Two sets of data are obtained by the Oriel where at the lower concentration, 2-3 suns, a neutral density filter of 85% spectral transmittance is inserted between the light source and the DNI. The second set of data by the Oriel is without the neutral density filter where concentration reaches up to 23 suns. Both sets of Oriel data are represented by blue dots in the plot. The Sinton flash test results are demonstrated by red dots in the plot. Both Oriel and Sinton V_{oc} increase logarithmically with linear concentration increment at room temperature, 25°C. Experimental results are considered to be thermally independent and it is demonstrated by a dot line fitted between the Oriel and the Sinton. However the XT-30 is a continuous high power solar simulator. Receivers illuminated by the XT-30 are not thermally independent and the cells operating temperatures are much higher than cells illuminated by a flash, Sinton, solar simulator. The higher cell operating temperature illuminated by the XT-30 is demonstrated by a lower V_{oc} than a cell illuminated by the Sinton under the same concentration. The XT-30 is tested with and without thermal paste coupled between the receiver and the heat sink. The V_{oc} of the 'without paste' condition, shown with green dots, under continuous illumination by the XT-30 is much lower compared to the 'with paste' condition, represented by grey dots. The shift of the V_{oc} indicates a higher device operating temperature without paste applied between the receiver and heat sink.

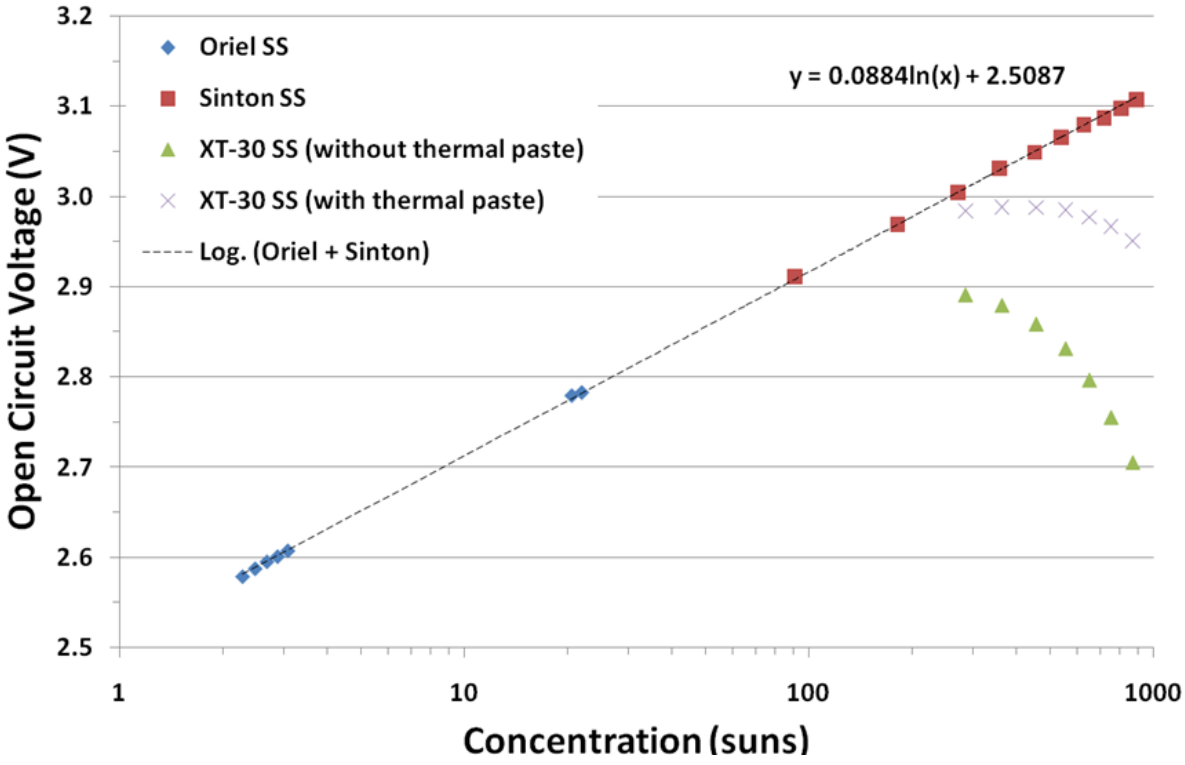

Figure 43 Averaged receiver V_{oc} of sample A by both flash and continuous solar simulator, where the dashed line is a logarithmic fit for the eye using type A calibration.

Figure 44 displays the V_{oc} under type B calibration which is tested by various solar simulators. Again, higher V_{oc} is recorded for the 'with paste' application during the XT-30 illumination. The V_{oc} performance of sample A using type B calibration by both Oriel and Sinton solar simulator system is identical compared to type A calibration. However the V_{oc} values shift towards lower concentration which can be identified by comparing Figure 44 and Figure 43 side by side.

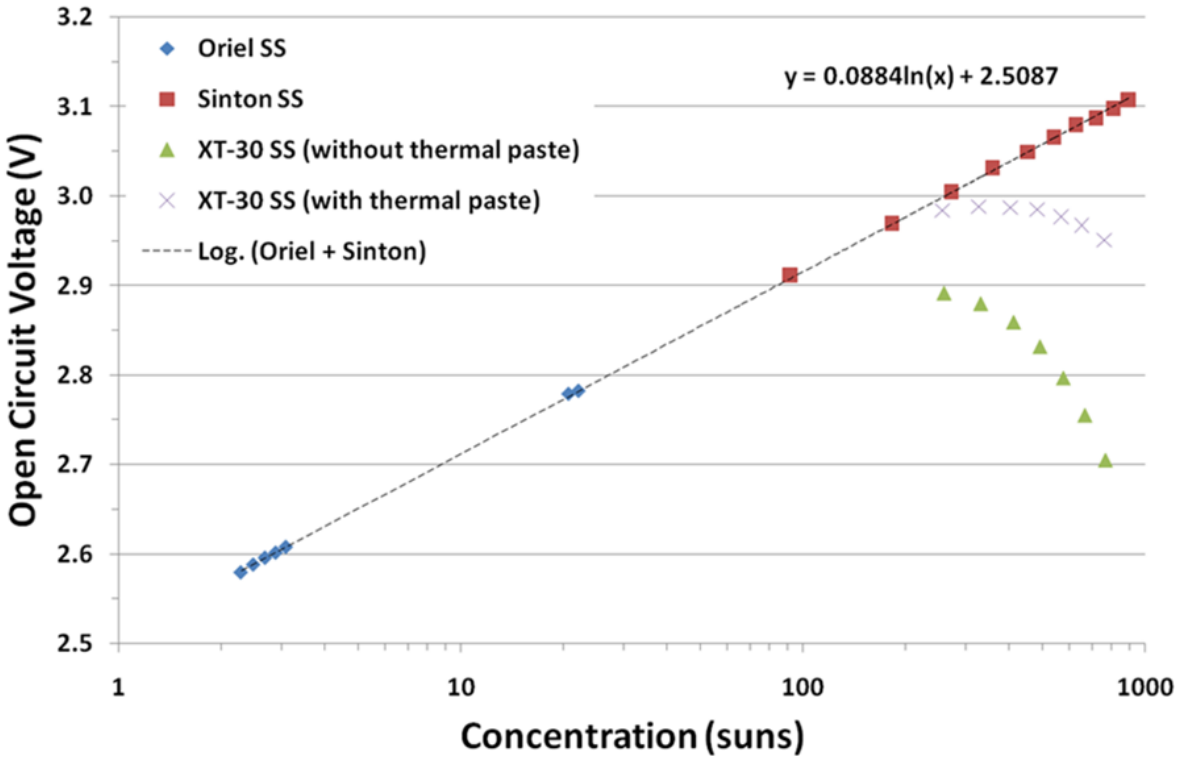

Figure 44 Averaged receiver V_{oc} of sample A by both flash and continuous solar simulator, where the dashed line is a logarithmic fit for the eye using type B calibration.

Figure 45 shows the V_{oc} under type A calibration of a sample B receiver illuminated by various concentrations in a no paste condition. The output performed by the XT-30 simulator shows the V_{oc} decreases from ~2.7 V to ~2.2 V as concentration increases from ~270 to 770 suns. Comparing sample A and sample B on a no paste condition by the same concentration, sample A provides a larger voltage output than sample B. In addition the voltage decreasing rate is greater for sample B which implies lower cell performance.

Figure 46 shows the V_{oc} using type A calibration of a sample B receiver illuminated by the various types of concentrator in a paste condition. The output voltage is improved by ~0.1 V.

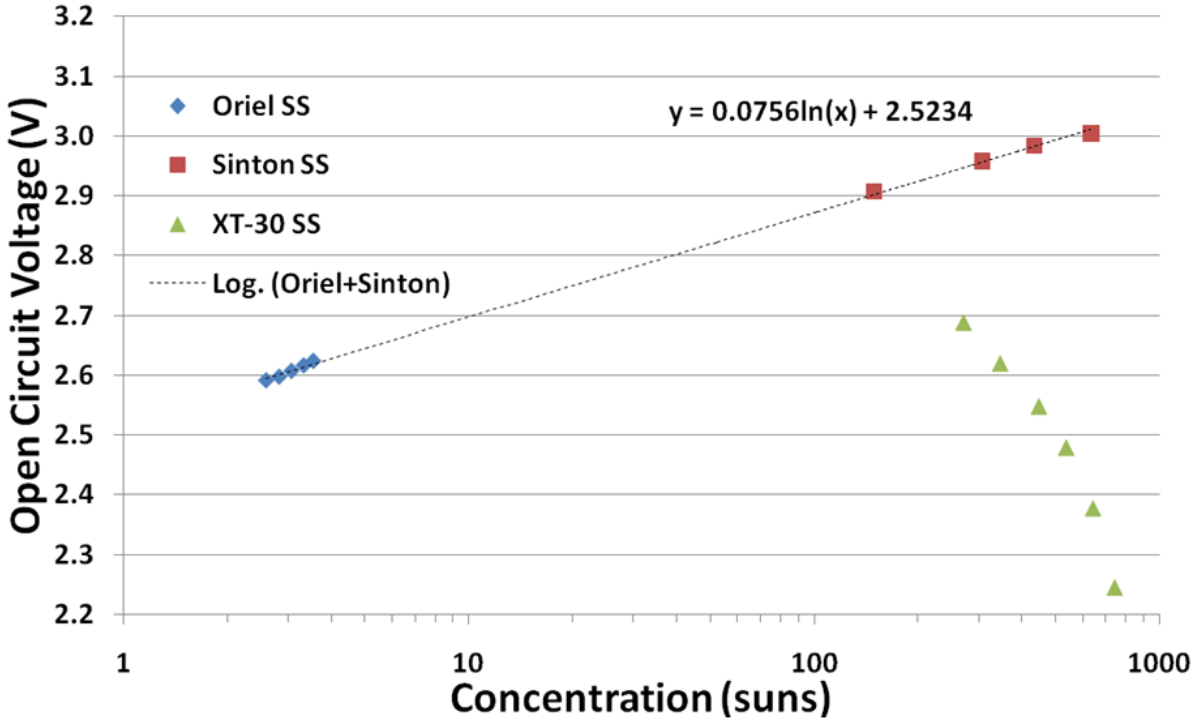

Figure 45 V_{oc} of sample B as a function of concentration without paste.

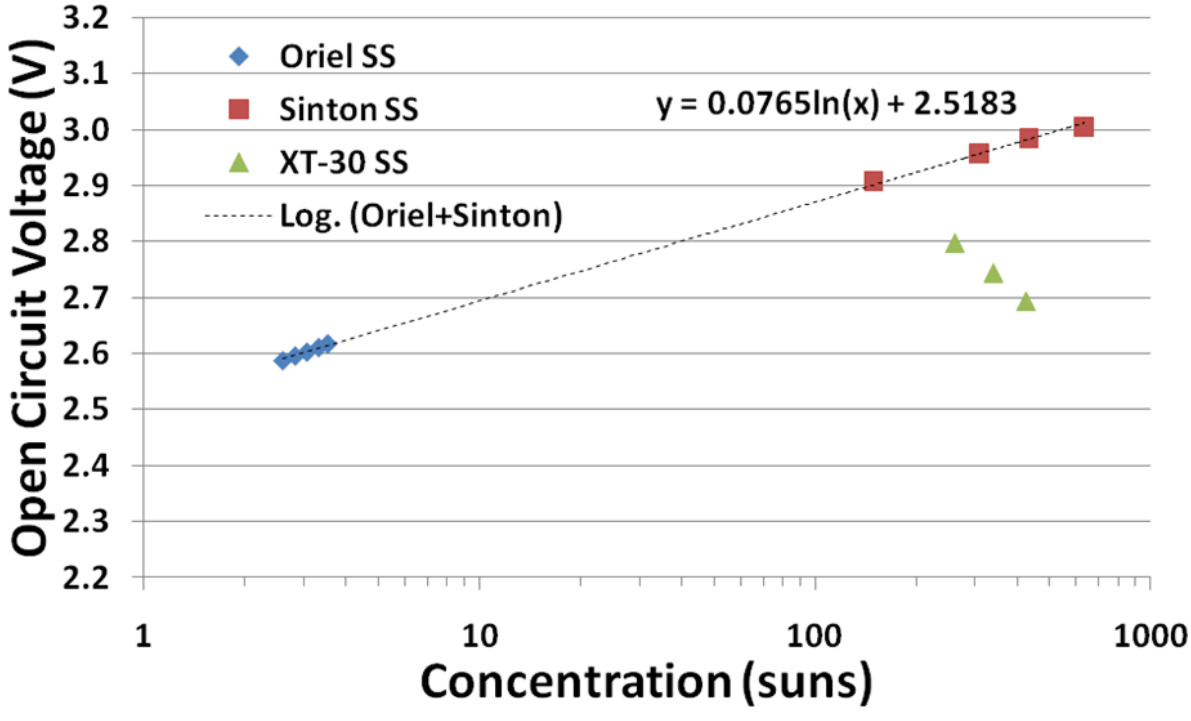

Figure 46 V_{oc} of sample B as a function of concentration with paste.

4.5. Efficiency calculations

The efficiency of a solar cell is the conversion ratio of photon energy to electrical energy as explained in section 2.12. Figure 47 and Figure 48 demonstrate the efficiency of sample A receiver illuminated by various solar simulators and concentrations. Figure 47 results are obtained using type A calibration while Figure 48 displays the efficiencies obtained using type B calibration. Efficiency measurements obtained by Oriel, Sinton, XT-30 with paste and XT-30 solar simulators without paste are shown in blue, red, grey and green, respectively. Concentrator solar cells are specifically designed to operate within a given range of concentrations for optimum conversion performance. In an ideal bare solar cell with a lossless contact grid, the efficiency increases by a log factor with a linear increment of input concentration. A solar cell with a non-lossless front metal grid contributes to both optical shadowing from light onto the cell and a small electrical resistance. An analytical study performed by H.B. Serreze [47] demonstrates the relationship between various front metal contact grid designs and power loss on a solar cell. Both Figure 47 and Figure 48 show the sample A receiver tested by Sinton has the best efficiency performance at 38%, between 500 and 600 sun concentrations at room temperature.

Below 500 concentrations, the efficiency curve follows a logarithmic behaviour as a function of increasing efficiency. Above 700 sun concentrations, the efficiency begins to roll-off due to an increase in series resistance of the solar cell. As concentration increases the operating current increases and the voltage drop in the solar cell becomes larger. Therefore the series resistance limits the high concentration performance [46]. Since the losses increase in proportion to concentration, in order for the efficiency to keep increasing above this point, the series resistances in the device need to be decreased [47].

An increase in the receiver operating temperature reduces the V_{oc}. This is clearly observed in Figure 43 to 44 when comparing equivalent concentration data points for the

cases with and without thermal paste. The application of thermal paste between the heat sink and the receiver contributes to lowering the operating temperature of the receiver and the efficiency increases by 1-3% in Figure 47 and 1.5% - 4% in Figure 48.

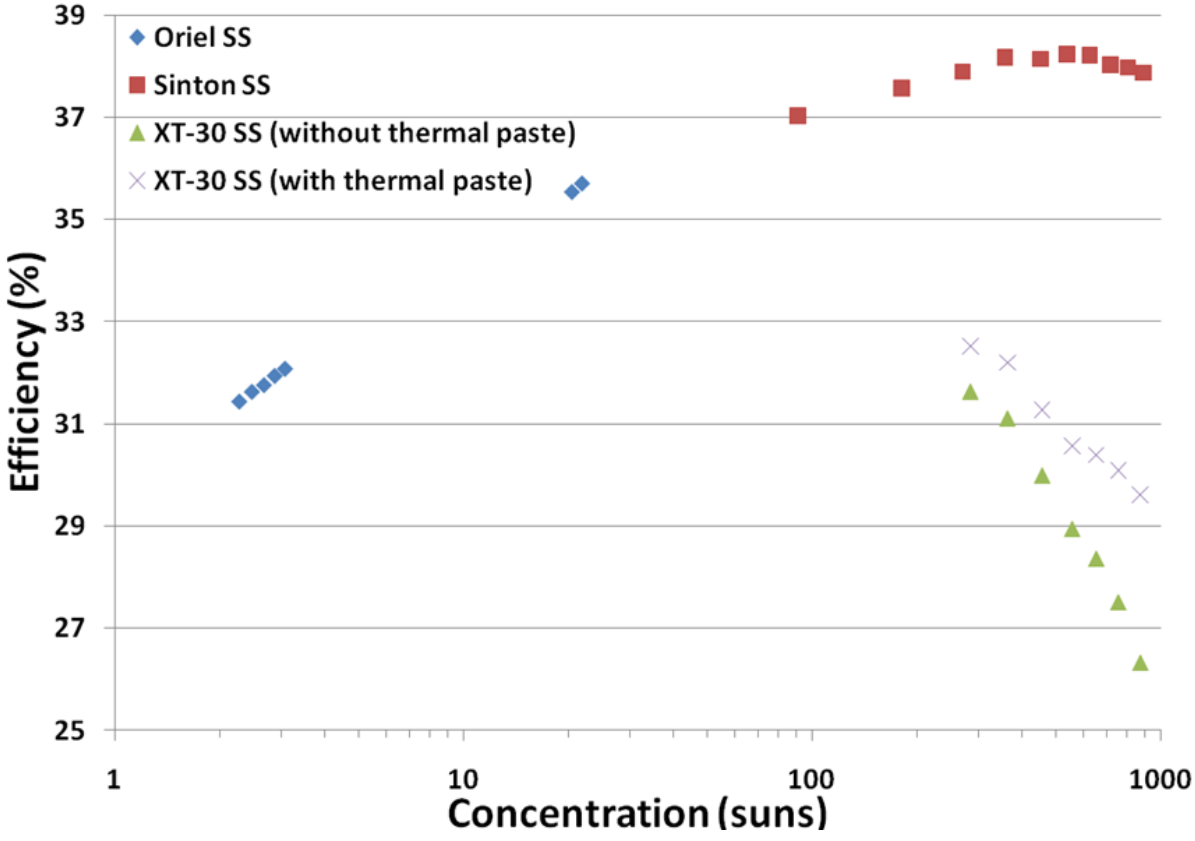

Figure 47 Averaged receiver efficiency by both flash and continuous solar simulator using type A calibration.

Efficiencies obtained from the XT-30 solar simulator by using type A concentration calibration are generally lower compared to type B calibration by 4%±0.5%. Illumination concentration mismatch is possibly due to the different current density at one sun coefficient between type A and type B calibration. Type A coefficient is a triple junction cell cross calibrated with NREL and type B coefficient is given by the cell manufacturer where it is cross calibrated with a NREL calibrated Si solar cell. The triple junction and the Si reference cell have different quantum efficiency. In addition, they have different contact grid design where various shadowing from the illumination contributes to the mismatch in concentration alignment.

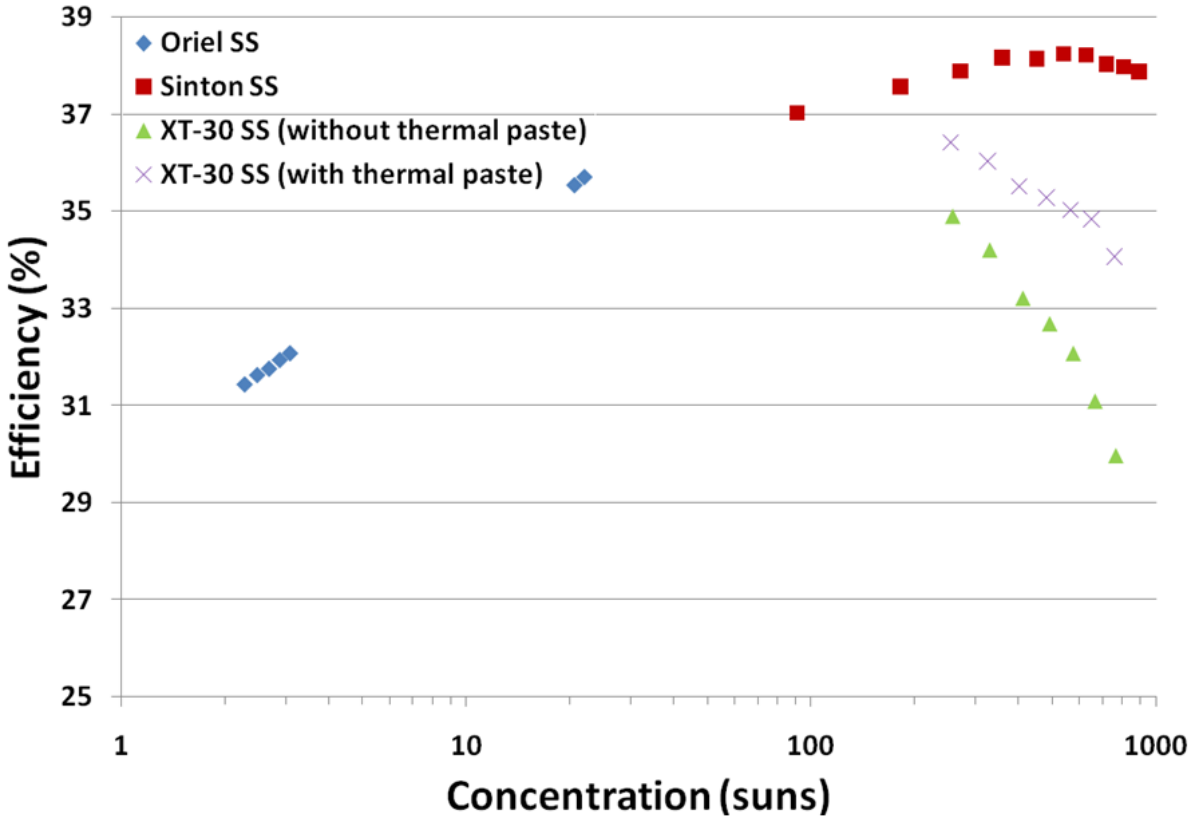

Figure 48 Average receiver efficiency by both flash and continuous solar simulator using type B calibration.

4.6. Cell temperature characterization

It is well known and extensively documented that the operating temperature of a solar cell affects its efficiency by varying the device's V_{oc} [49]. The rate of cell efficiency decrease as a function of the V_{oc} and the operating temperature on a MJ cell has been studied using simulations by Geoffrey S. Kinsey, et al [50], where they showed that at 500 suns concentration the V_{oc} decreases by ~4.3 mV/°C [51].

Figure 49 and Figure 50 demonstrate temperature changes, above the room temperature, on four sample A and two sample B receivers under various concentrations. The changes in temperature results are obtained by taking the differences of the V_{oc} between the Sinton and

the XT-30 solar simulator at the same concentrations and multiply the coefficient of ~4.3 mV/°C. The resulting ΔT's are the temperature difference between the XT-30 and the Sinton under the same concentration. Specific sample results are shown in coloured circles. Sample A and B temperature change results in Figure 49 and Figure 50 include the conditions of with and without thermal paste used during the experiment. A significant improvement is observed on the cell thermal management and the data uncertainty with the use of thermal paste. The uncertainty is reduced from Figure 49a of ±4°C to Figure 49b of ±0.5°C.

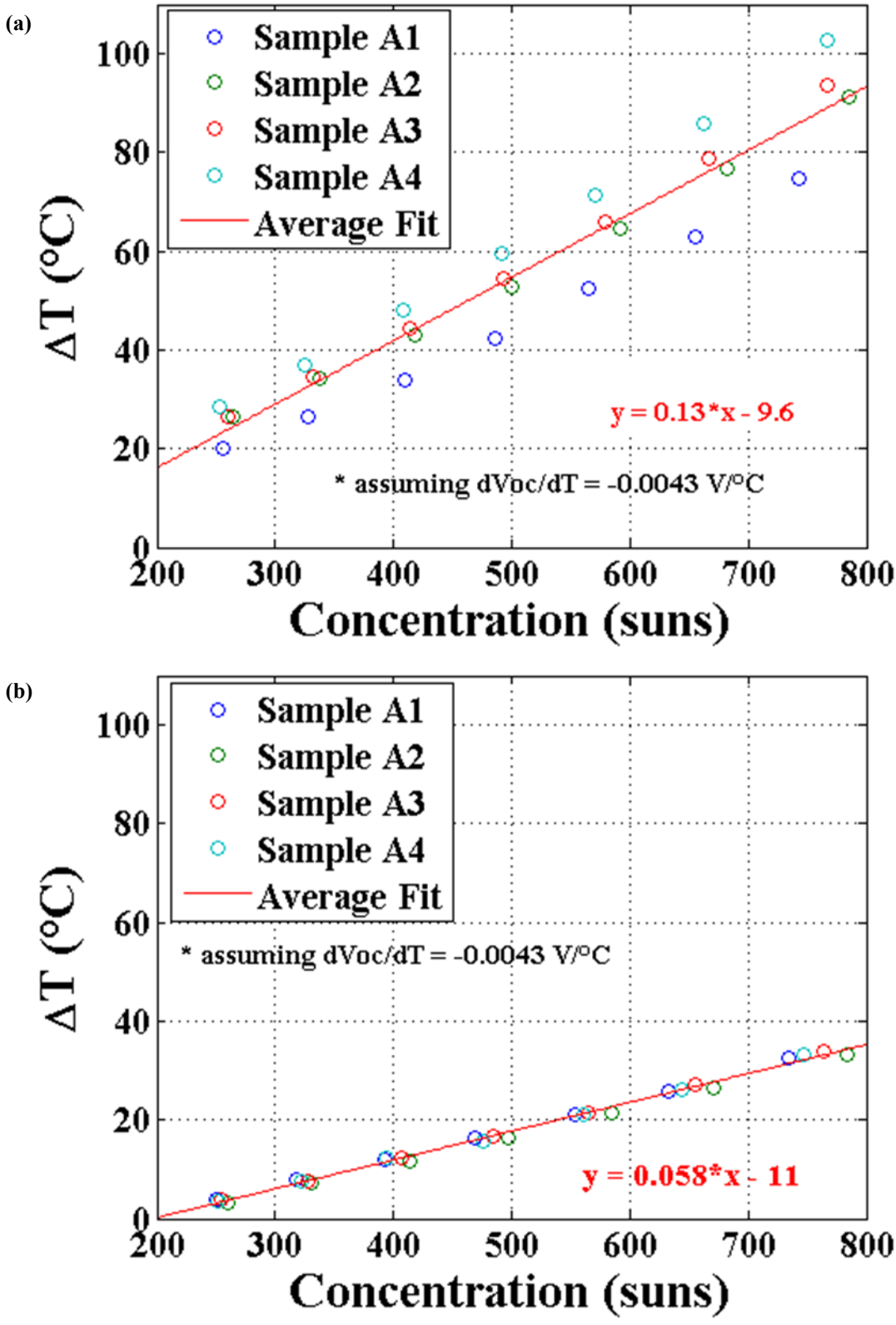

Figure 49 Experimental temperature change relative to room temperature for each tested receiver under various concentrations by the continuous solar simulator for (a) no thermal paste, (b) thermal paste used. The line is an average fit using all data points sample A.

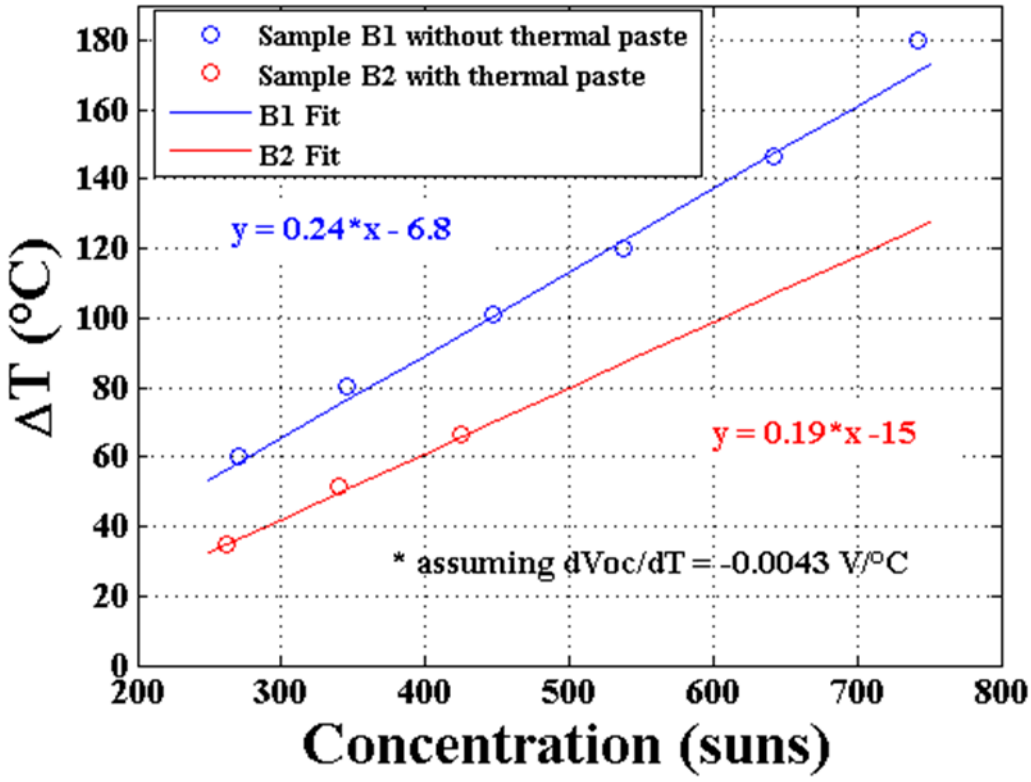

Figure 50 Experimental temperature change relative to room temperature as a function of concentration for sample B. The line is an average fit using all data points sample B.

4.7. Sample C testing

Sample A and sample B where with carriers having the same material with varying geometries, the carrier of sample C is fabricated by a different material, namely PTFE. PTFE carrier is an off-the-shelf component with a copper layer already on the carrier, therefore a far more economical option than alumina. However the thermal conduction of PTFE is approximately an order of magnitude lower than alumina, as shown in Table 2, which could be a significant drawback. When sample C receivers where tested under the XT-30 solar simulator, the high continuous power resulted in them being heated to a level resulted in catastrophic optical damage of the solar cell before any results could be taken. Figure 51 shows the current-voltage plot of the sample C receiver by the Oriel solar simulator at room temperature. The calibrated intensity is ranges from approximately 2.7 to 4.2 suns using type A calibration.

Figure 52 shows the top view of the solar cell on the sample C receiver before and after the XT-30 illumination.

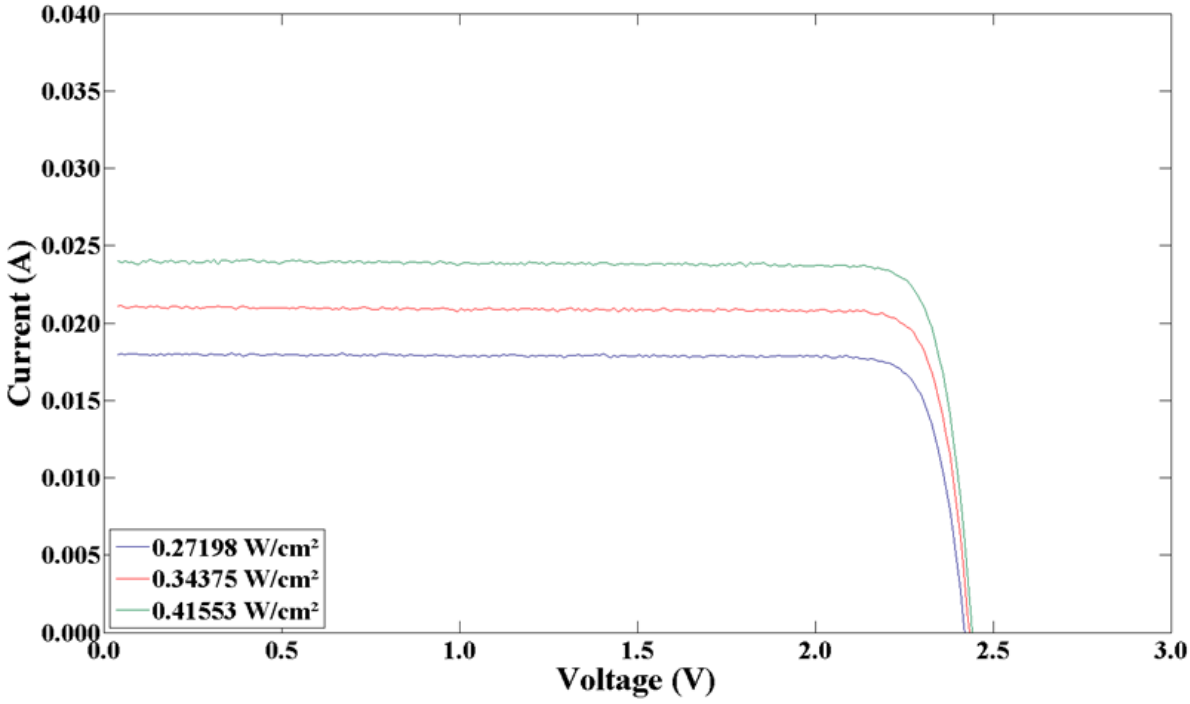

Figure 51 Current as a function of voltage of sample C receiver under the Oriel solar simulator with type A calibration at 25°C.

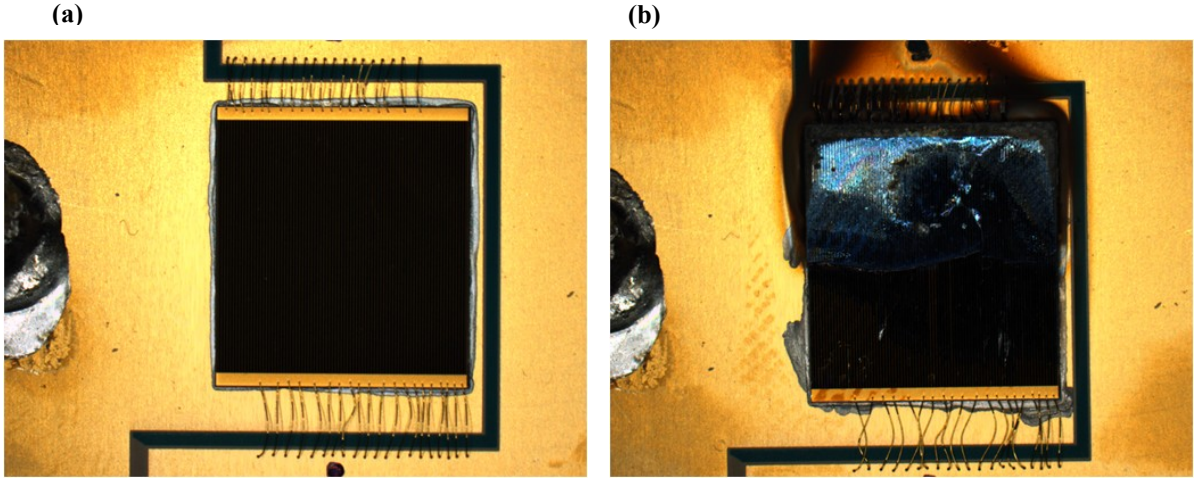

Figure 52 Solar cell on a sample C receiver (a) before XT-30 solar illumination (b) after XT-30 illumination.

4.8. Carrier surface temperature

A solar cell on a carrier under illumination can be viewed as a heat source; the carrier acts like a thermal spreader with heat flux travelling laterally on the carrier before going to the heat sink located below the carrier. In theory, high lateral heat spreading and low vertical thermal resistance of a carrier creates the ideal solution for receiver cooling. The performance of the receiver may also be evaluated by measuring the temperature on the surface of the carrier.

Figure 53 demonstrates the setup and additional tools used during surface temperature measurement. Test receivers are placed on the chuck and illuminated by the continuous XT-30 solar simulation. A K-type thermocouple capable of measuring temperature from -200 to 1250°C ±1.1°C is connected to an Omega HH509R dual channel digital reader. The measuring tip of the K couple is secured on a designated spot for temperature readings using Kapton tape.

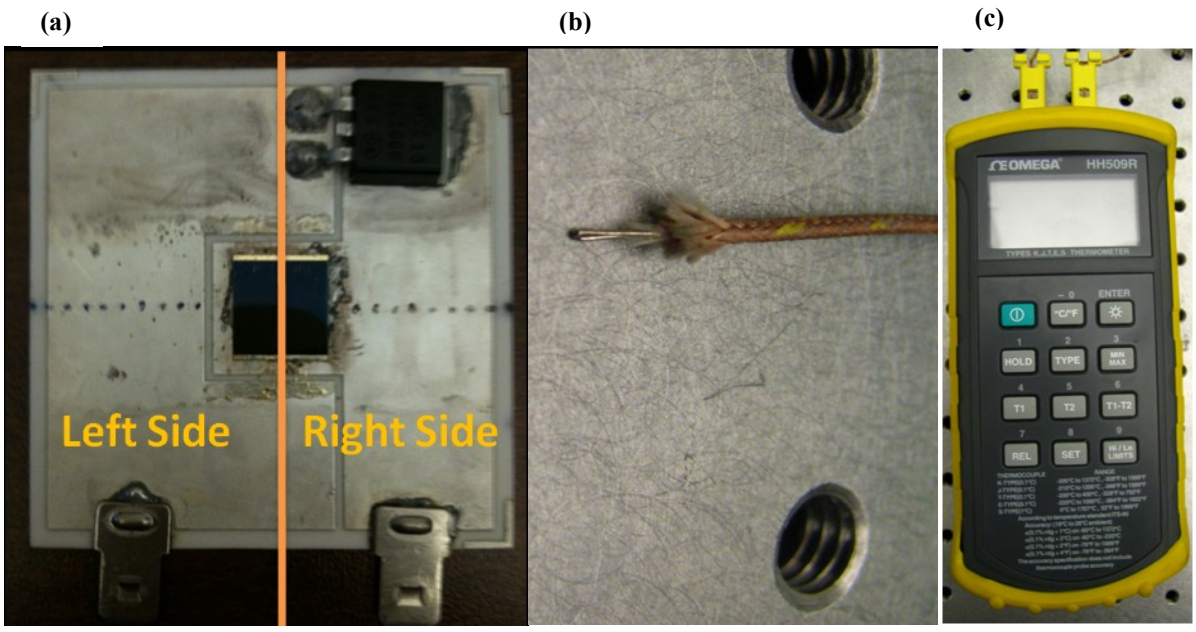

Figure 53 Surface temperature experimental setup (a) Die attached triple-junction solar cell on a silver conductive substrate carrier with marked spot for thermistor probing (b) K-type thermo couple (c) Dual channel Omega thermometer.

Figure 54 displays the surface probing temperature on the carrier corresponding to the center of the receiver. Both left and right sides of the receiver are probed while the solar cell is illuminated at 337±10 suns. The surface heat profile shows temperatures from the edge of the receiver rising exponentially towards the center as expected. The average surface temperature between the left, shown in red, and the right, shown in blue, indicates higher temperature on the right side when closer to the center, indicating the uncertainty on our measurements (±1°C).

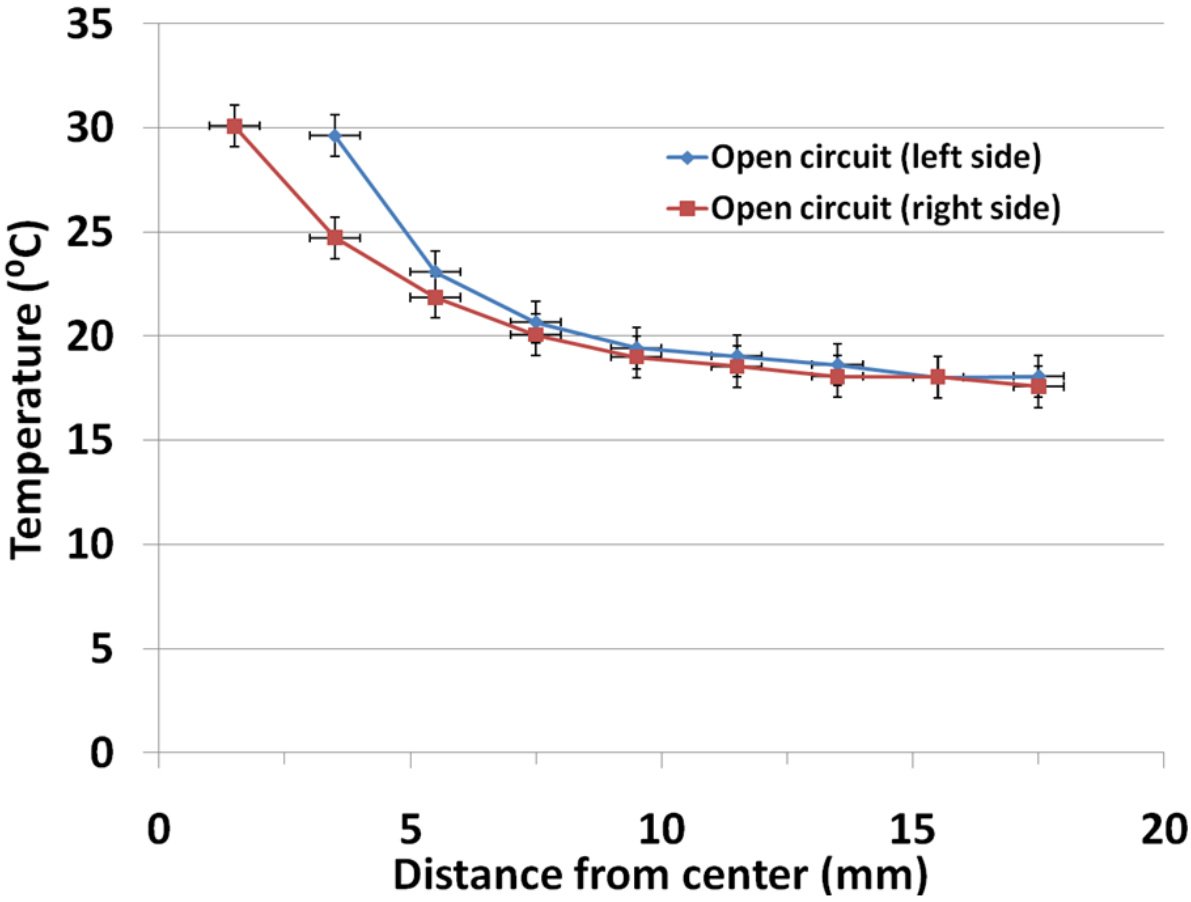

Figure 54 The averaged surface thermal profile of sample B3 is illuminated under 337±10 suns. The results tested under an open circuit condition are illustrated with right side of the carrier as the blue line and left side as the red line.

Figure 55 shows the carrier surface temperature profile of sample A, B and C receiver under ~340±10 sun concentrations. They are displayed as red, blue and green respectively. Both sample A and C are small receivers, therefore the distance between the receiver edge and light mask on the center of the solar cell is very narrow. Only three and two data points are collected by sample A and C respectively, while sample B has nine. The test results show the lowest surface temperature belonging to sample B, followed by sample A and then C.

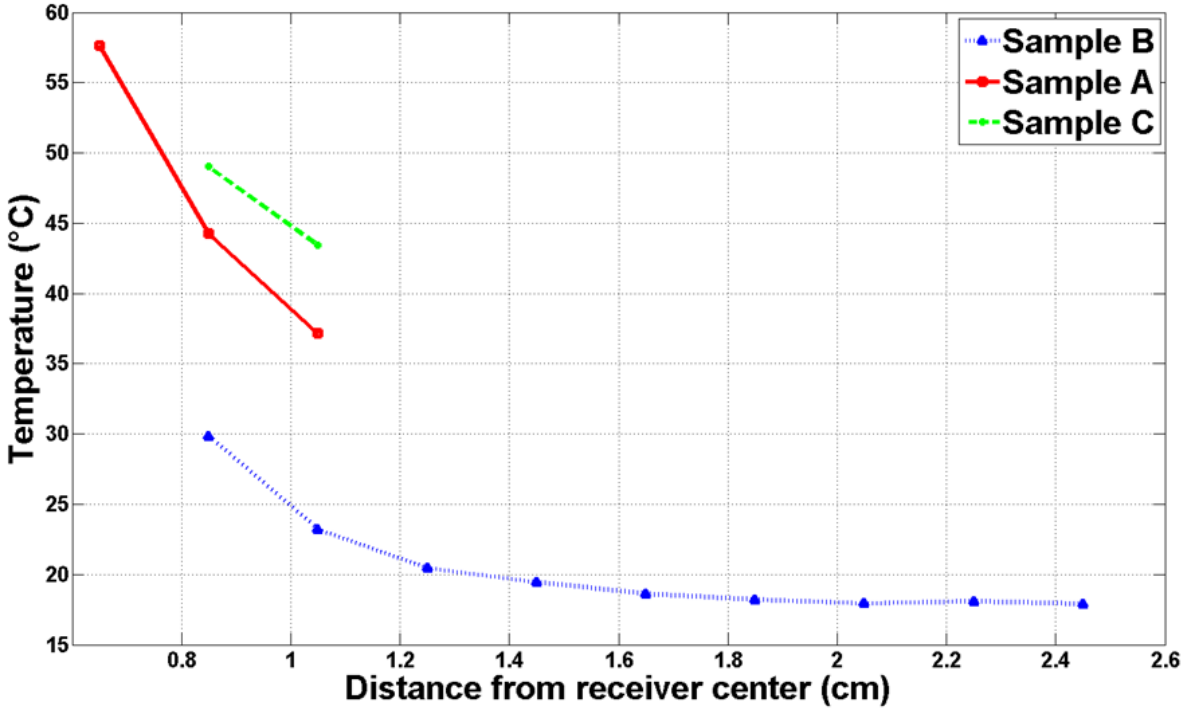

Figure 55 Surface temperature comparison between different samples with various channel geometry and material design.

4.9. Failure mechanism

MJ solar cells under concentration are subject to high current and temperature stress. If a MJ solar cell is unable to sustain continuous operation under concentration, the benefits of cost–cutting and efficiency gain are negated. Concentrator cell failure normally happens shortly after exposure to concentrated light and failure mechanisms include cell shunting, electrical shorts and cell cracking. Failure can be caused by a number of factors, including cell manufacture defects, thermal mismatch between the cell and the carrier, loss of thermal management or moisture on the cell. The loss of thermal management is associated with cracks and voids in the solder layer coupling between the cell and the carrier; this is the most common failure mechanism observed. These voids act as a thermal insulator trapping heat within. The hot spots that result under concentration lead to thermal current crowding and thermal runaway. These hot spot voids increase the cell temperature and decrease the output

efficiency. It can also permanently damage the cell by incinerating the solder or the cell, as shown in Figure 52.

Figure 56 is an example of cell cracking after XT-30 solar simulator illumination at a concentration of ~600 suns. A possible explanation is the existence of a void within the center of the solder layer causing the temperature to rise rapidly. Part of the MJ cell has melted due to high temperature.

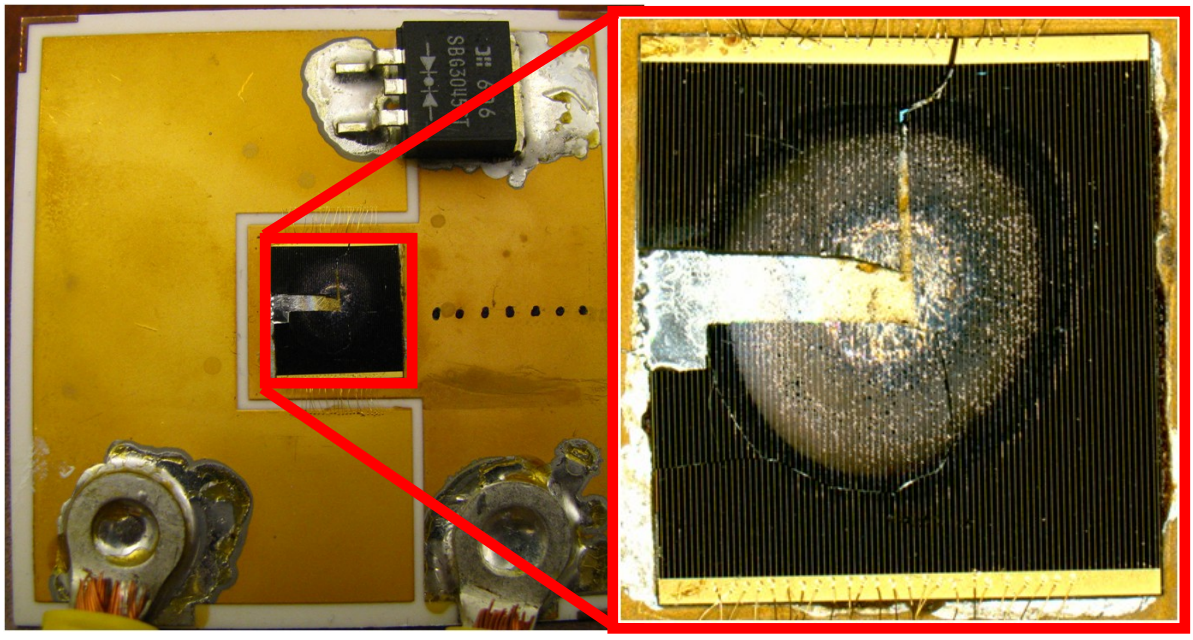

Figure 56 Damaged chip on carrier solar cell.

Part of the chip on carrier process involves soldering a solar cell die onto a carrier. Typically it is done by applying solder paste on the carrier and slowly lowering the solar cell onto it. Heat is applied to the bottom of the carrier to reach the solder melting point, and after placement it is cooled to room temperature. The amount of solder and the application method is crucial to the survival of the receiver. A receiver with excess solder may result in the short circuiting of a solar cell, whereas not enough solder can create voids or gaps between the cell and carrier as displayed in Figure 57.

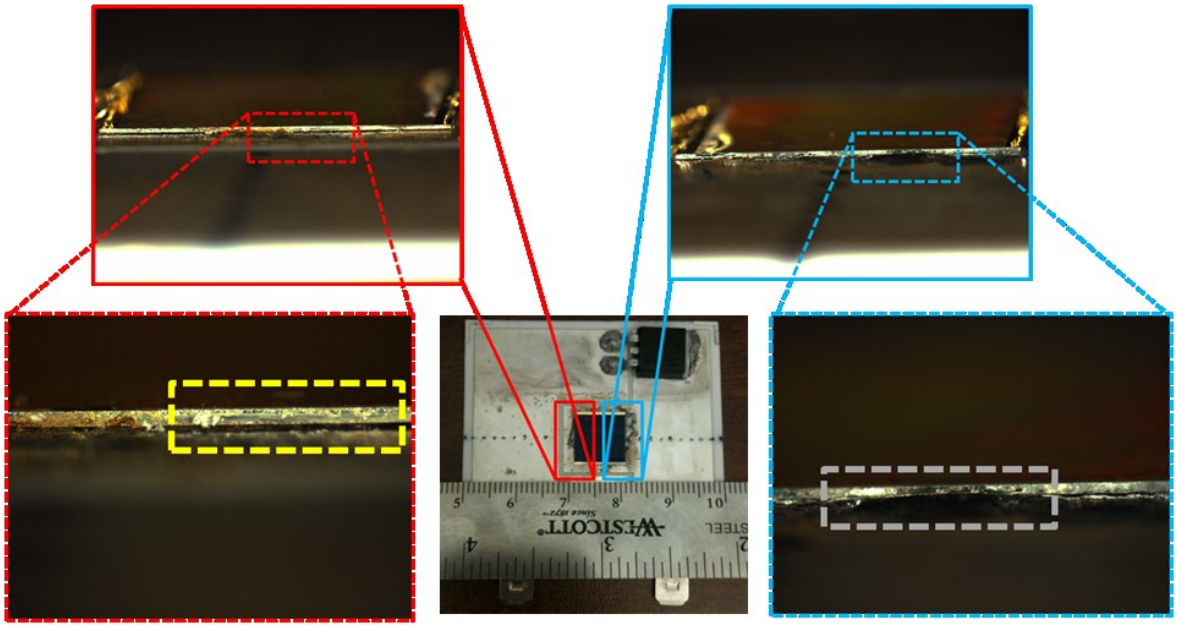

Figure 57 An example of an imperfect chip on carrier process where the air gap (yellow square, left) is found between solar cell and carrier and excess solder (grey square, right) touching the cell edge.

4.10. Conclusion

This chapter presented the experimental results of sample A, B and C types of receiver under the illumination of both flash and continuous simulators. The presented results include current-voltage characterization, V_{oc} and efficiency mapping, cell temperature, carrier surface temperature and receiver failure mechanism. Experimental results demonstrate that the use of thermal conductive paste between the heat sink and the receiver improves the V_{oc} resulting in a gain in conversion efficiency. Sample A has demonstrated an advantage over sample B in efficiency and cell temperature under continuous illumination by the XT-30 solar simulator. Sample C fabricated with a lower thermal conductive material is more suitable for low concentration as it is rendered inoperable under high concentration. More detailed comparison on these carriers designs will be done in the next chapter.

The calibration method named type A and B to determine the solar cell efficiency and the V_{oc} as a function of concentration relies on matching the current density output illuminated by different solar simulators. Type A and type B calibrations for the XT-30 solar simulator employ different current density multipliers. The resulting type B concentrations correspond to the V_{oc} values were lower than type A concentrations and a mismatch in the efficiency by 4%±0.5%. The cause may originate from a different reference sample used by type A and B during calibration, also analysis using spectral mismatch could possibly reconcile the two calibrations. At the time of the measurements done for this thesis, equipment to measure spectral mismatch was not available.

The study on carrier surface temperature focuses on the probing on both left and right sides of the receiver under open circuit illumination and the comparison between all test samples. The temperature change decreases in a logarithmic fashion as the distance from the center of the solar cell increases. Experimental surface temperature probing comparisons between samples reveal sample B has the lowest surface temperature distribution follows by sample A and C. It seems with lower surface temperature should result with a lower cell temperature but this is not true. The copper layer thickness on the receiver directly affects the cell temperature. The copper layer of sample B is not thick enough to spread the lateral thermal current from the solar cell to the receiver edge before cooling. Most of the heat current remains close to the cell. Chapter 5 shall discuss the relationship between the copper thickness and the cell temperature.

The main solar receiver failures resulted from packaging a cell on a carrier where a void or gap existed within the solder layer. This gap was found to have created a thermal runaway, reducing the overall thermal conductivity of the receiver.

Chapter 5 Modelling of thermal effects

5.1. Introduction

This chapter introduces the COMSOL and MATLAB scripted COMSOL numerical simulator for thermal modeling of concentrator cell receivers. A detailed discussion will be given on the simulation background, receiver model design, boundary values for each model and calibrations from experimental value. The simulated average cell temperatures and operating efficiencies are projected up to 2000 solar concentration. A convergence study based on the meshing technique and the approximating elements are conducted. In addition, the input power to cooling power relationship, geometry size, copper thickness and channel shape of the receiver are investigated by simulation and discussed.

5.2. COMSOL software

COMSOL Multiphysics is a graphical interactive numerical simulator for modeling and solving partial differential equation based scientific problems. The numerical simulator employs the finite element method to solve all partial differential equations in the problem. Although other methods such as the finite difference method and the moment method are simpler and easier to apply, finite element method is more powerful in solving complex geometries and inhomogeneous media such as thermal performance of a multi-anisotropic layers designs. The concept of the finite element method is to find the solution of a complicated problem by replacing it with a simpler one. The analysis of any problem using the finite element method requires four basic steps [52]:

- Dividing the solution region into a finite number of sub-regions or elements
- Deriving the governing equations for a typical element
- Assembling all elements in the solution region
- Solving the system of equations obtained

During simulation and modeling, COMSOL undergoes similar steps compared to the four basic steps where geometries are treated as objects and requires the user to plot them in a built-in computer-aid design tool or import the geometries from external source. The object is then divided into smaller pieces of finite dimensions named finite elements and the dividing process is called meshing. The original object is considered to be the assemblage of the finite elements connected at a finite number of nodes where none of the elements are overlapping each other. The properties of each element are formulated individually and combined to obtain the properties of the entire body. The equations of equilibrium for the entire object are obtained by combining the equilibrium equation of each element in such a way that continuity is ensured at each node. After the geometry meshing and the formulation of the entire body, the necessary boundary conditions are imposed on the faces of the object. The equilibrium equation is then solved to obtain the required variables.

5.3. MATLAB-COMSOL software

COMSOL Multiphysis is a model and simulation tool often used in the engineering and scientific fields. It is also a discrete tool where simulating with ranging parameters cannot be automated. To achieve automated simulation, COMSOL provides external functions that can be invoked by other programs such as MATLAB. Scripts written in MATLAB code specifically tackle the analysis that requires continuous simulations while in variation of geometry size, shape and layer thickness. In addition the changing of input heat power, which mimics the concentrate illumination on the solar cell and the cooling power at the bottom of the receiver, is also in the interest of study where script automation is necessary.

5.4. Receiver Design

A basic solar cell receiver requires a ceramic carrier with both electrical transporting (using metal pads) and heat transferring functions. The performance of a solar cell is greatly dependent on the operating temperature since the cell efficiency is reduced under high

operating temperature. Solar cell receivers as tested experimentally are put to investigations through thermal profiling in COMSOL. Experimental receivers from were first plotted and materials were picked for each layer of the receivers. The physics inside the receiver is described by a heat balance where heat flux takes place by conduction. The boundary condition for the receiver follows the heat equation:

$$-k\nabla T \cdot \mathbf{n} = h(T - T_{amb}) \qquad 5\text{-}1$$

where h is the heat transfer coefficient, $\mathbf{n}$ is the normal vector to the boundary, k is the thermal conductivity and T is the temperature. The thermal conductivity values for materials used and the receiver dimensions in COMSOL can be found in Table 1 and Table 2. The boundary conditions for the faces of a receiver are set to the values shown in Table 4. The procedure of implementing a receiver in COMSOL can be found in Appendix A.

Parameters	Top cell face	Bottom face	Others
Inward heat flux (W/m^2)	*	0	0
Heat transfer coefficient (W/(m^{2}K))	25	**	25
External temperature (K)	303.15	291	303.15
Problem-dependent constant (W/(m^{2}K^4))	0	0	0
Ambient temperature (K)	303.15	291	303.15

Table 4 Boundary condition settings for simulation object faces. * Concentration settings where changeable for higher or lower concentration. ** Cooling settings where different for each receiver.

The inward heat flux on the top cell face represents the total power created as heat under solar illumination. As mention earlier the solar concentration is proportional to the solar radiation on the Earth which is approximated to be 1 kW/m^2 at one sun. During COMSOL simulation all solar energy is converted to heat energy for the worst case scenario (efficiency of the cell is 0%). The bottom face depicts the bottom of the receiver where cooling takes place. The cooling power represented by the transfer coefficient, h, is calibrated by actual

experimental results shown in the section 5.5. Each solar receiver design corresponds to a distinct transfer coefficient.

Figure 58 displays the result of three sample receivers each with various concentration and cooling power as part of the boundary conditions in the COMSOL simulations. The simulation receiver geometry matches the physical experimental receiver size and material for each design. The temperatures on the three receivers are represented by the color scale on the right and this scale is different for each figure. Preliminary simulation results show that most of the heat is centered on the solar cell and gradually decreases towards the edge of the receiver. Figure 58 also shows that the thermal distribution pattern differs with various geometry designs, shapes and corresponding materials. One of the design variations is the channel design inside the copper layer. The channel isolates the anode and cathode connection on the receiver. The thermal behavior study of different channel design takes place later in this chapter. The corresponding pattern for a L channel design is displayed in Figure 58a and for the hat channel design is shown in Figure 58b.

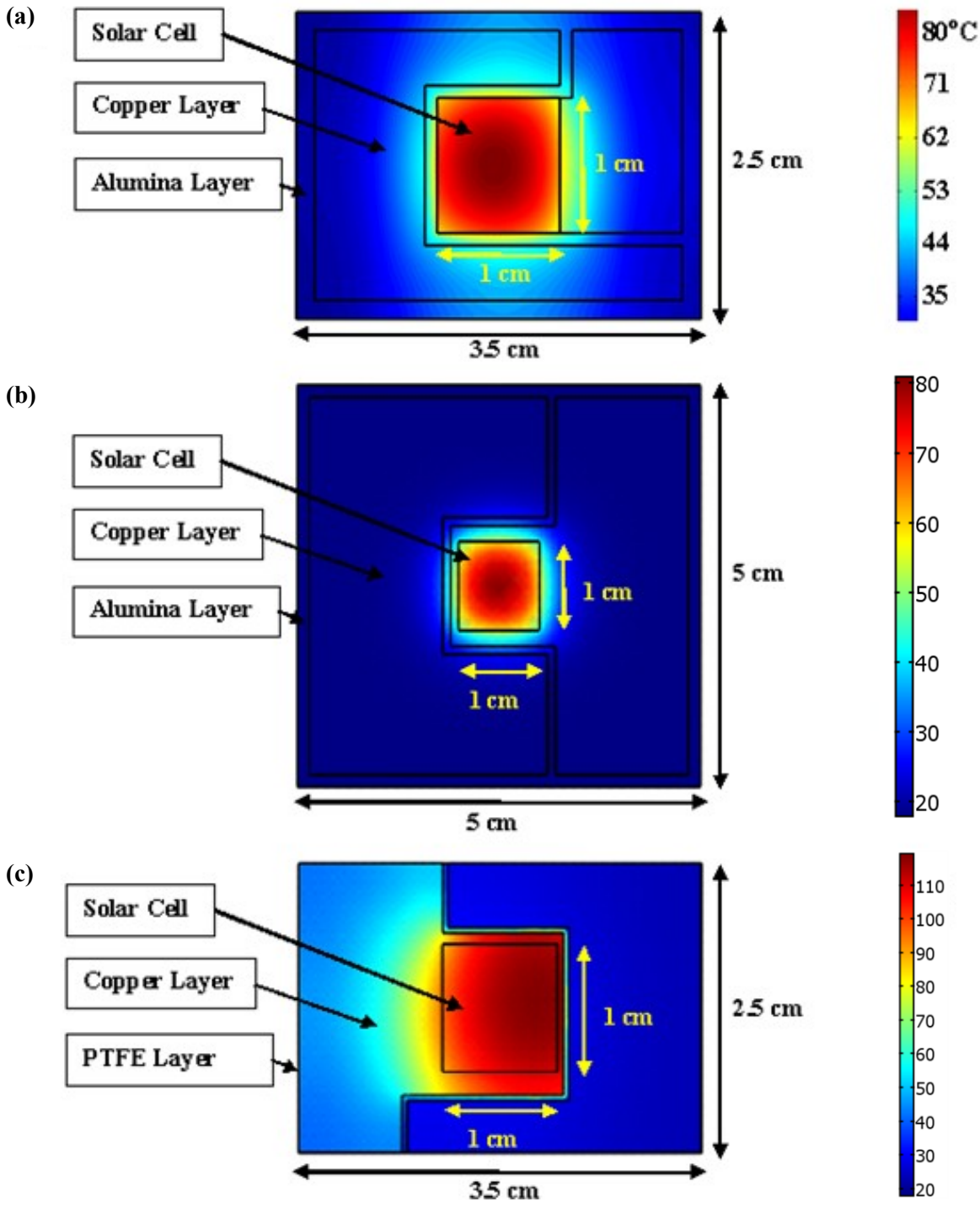

Figure 58 Simulated thermal distribution of solar cell mounted on (a) a type Sample A alumina receiver illuminated at 500 suns concentration without paste, (b) a type Sample B alumina receiver illuminated at 337 suns with no thermal paste, (c) a type Sample C PCB receiver without thermal paste at 50 sun concentrations.

5.5. Simulation calibration

Solar receivers under concentration require cooling to maintain high conversion efficiency. Concentrator solar cells are soldered onto the carrier where the back or the bottom of the carrier is typically used to extract heat from the receiver. For the COMSOL model of a receiver, the cooling power of the receiver back is determined by a heat transfer coefficient, *h*, which is the amount of heat flux per area per second taken away from the back surface. The transfer coefficient is calibrated by matching both experimental with simulated average cell temperature as a function of sun concentration.

Figure 59 is the cell average temperature as a function of concentration for the sample A receiver, comparing the experimental results and the V_{oc} calibrated simulation. Experimental results are presented as symbols and simulation results are shown in lines. The simulation cooling power, *h*, of sample A is calibrated to be 2600 W/(m^{2}K) without thermal paste and 14500 W/(m^{2}K) with thermal paste coupled between the receiver and testing stage. Calibrations between experimental and simulation for both conditions fit closely within the experimental uncertainty of ±2.3°C. The maximum calibrated temperature deviation from 100 to 800 sun concentrations is 3.5°C±1°C without the thermal paste and 2.2°C ±1°C with the thermal paste.

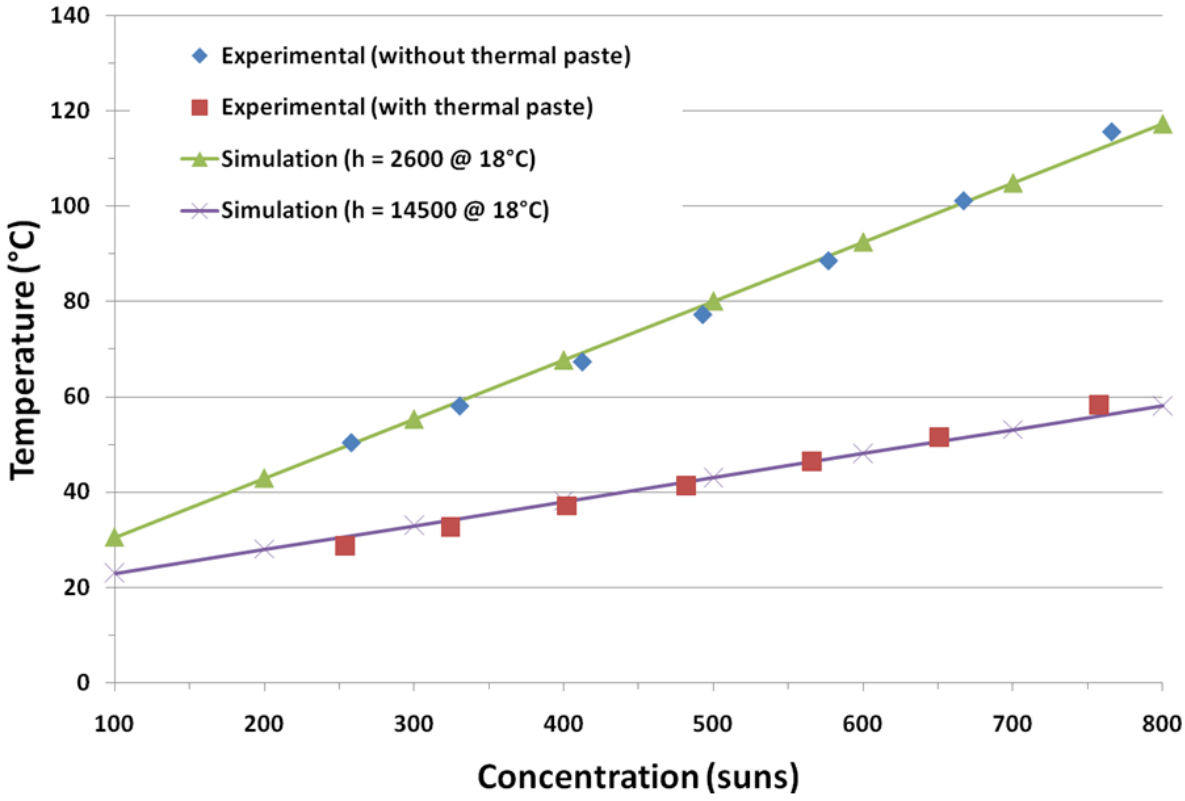

Figure 59 Simulated and averaged experimental temperature of the solar cell mounted on a sample A receiver with/out thermal paste applied between the receiver and the chuck.

Present high concentration PV systems incorporating multi-junction solar cells typically have ~500 suns concentrations, and concentration systems near 1000 suns are being developed to take the advantage of the higher efficiencies available. In the near future concentration could reach 2000 suns, therefore an investigation of such high concentration is required. After the calibration between experiment and simulation, the average cell temperature obtained with the COMSOL receiver models are utilized to project receiver operating temperature at higher concentration. Figure 60 is the average cell temperature and efficiency difference as a function of concentration from 100 to 2000 suns concentration. A calibrated sample A receiver was simulated by COMSOL for thermal paste (red) and non-thermal paste (blue) conditions. Solar receivers with an integrated thermal paste system have a higher heat transfer coefficient and extract more heat from the solar cell, and hence the average cell temperature is lowered compared to the case without the application of thermal paste. The efficiency difference (green) is the difference in cell conversion

efficiency between the paste and no paste condition where the resistive effect beyond 500 suns concentration is ignored. The curves are linearly fitted and the fit equations are displayed in the figure.

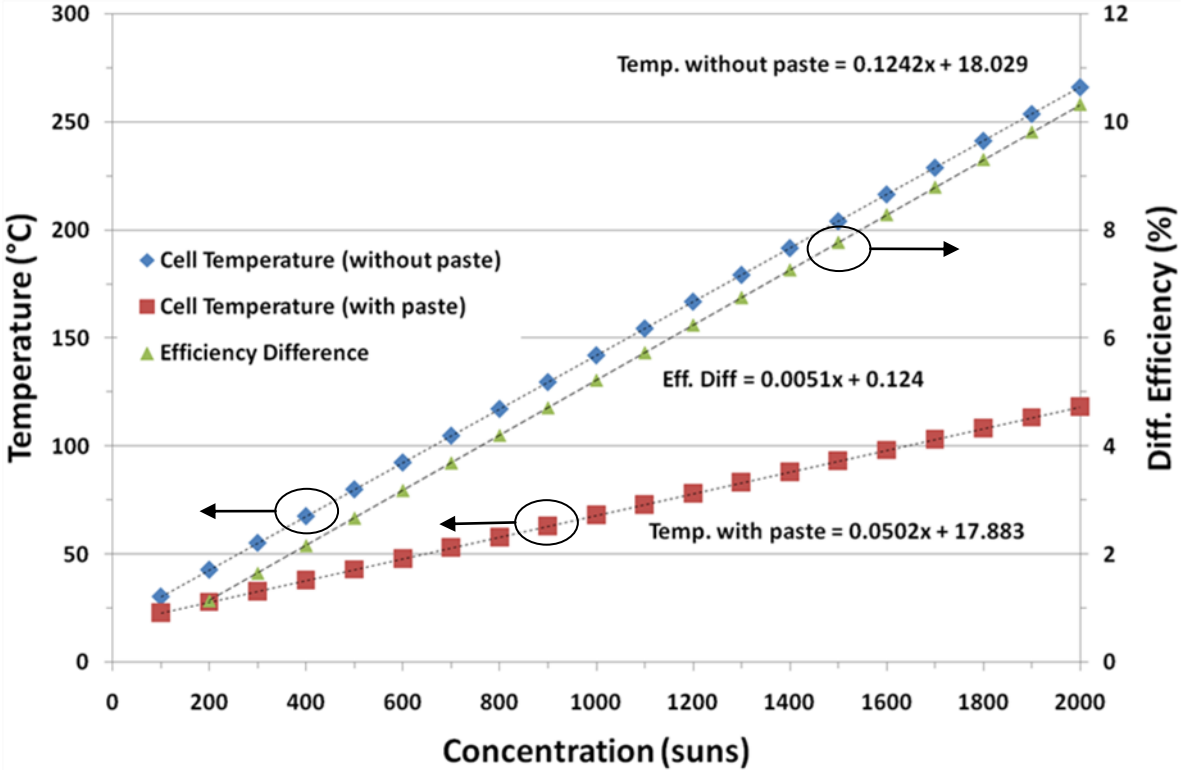

Figure 60 Simulated projection of the average cell temperature and difference in receiver efficiency up to 2000 suns for receiver A design.

Figure 61 presents both experimental and simulated average cell temperature results as a function of concentrations for a sample B receiver. The cooling power on the bottom of the sample B receiver is calibrated to be 1940 W/(m^2K) without paste and 3085 W/(m^2K) with paste applied conditions. The average error between experimental and simulated results is ~0.4°C without and 4°C with thermal paste condition. Sample B receiver possesses a higher thermal characteristic than sample A. The sample B average cell temperature is almost double of sample A under same concentration. In addition the lower cell temperature available when using thermal paste shown in sample A does have less impact with sample B by comparing the slope coefficient of both paste curves.

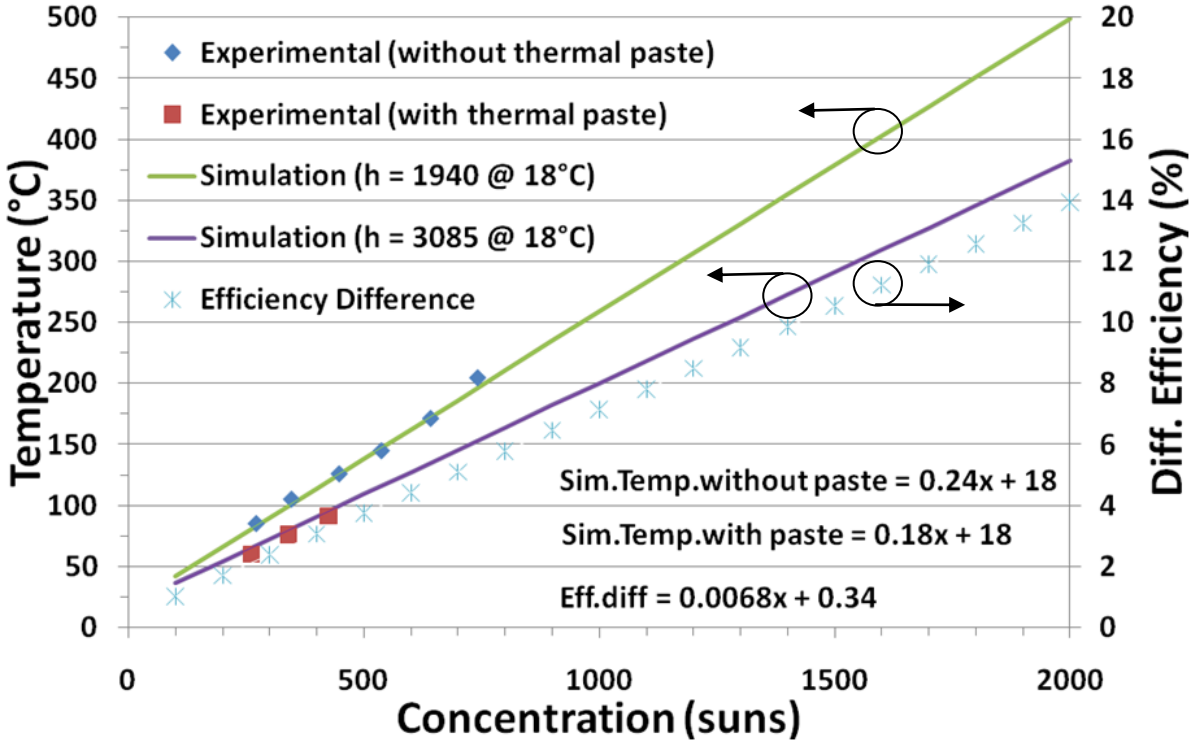

Figure 61 Experimental calculated numerical model and simulated average cell temperature of a sample B receiver as a function of concentration. Thermal paste / no thermal paste conditions is denoted difference in efficiency.

The experimental heat distribution data on the surface of the solar receiver discussed in the previous chapter can also be used to calibrate the cooling power of a simulated solar receiver model as an alternative comparison to this cell-temperature calibration method. The surface heat distribution of a receiver is the result of a combination of input thermal power, edge length, thickness, geometry shape and cooling power. The heat distribution pattern on the receiver is unique given a calibrated constant input thermal power and a fixed geometry while varying the cooling power of the receiver shown in Figure 62. The cell center is located at 0 cm and the edge of the carrier is at 2.5 cm.

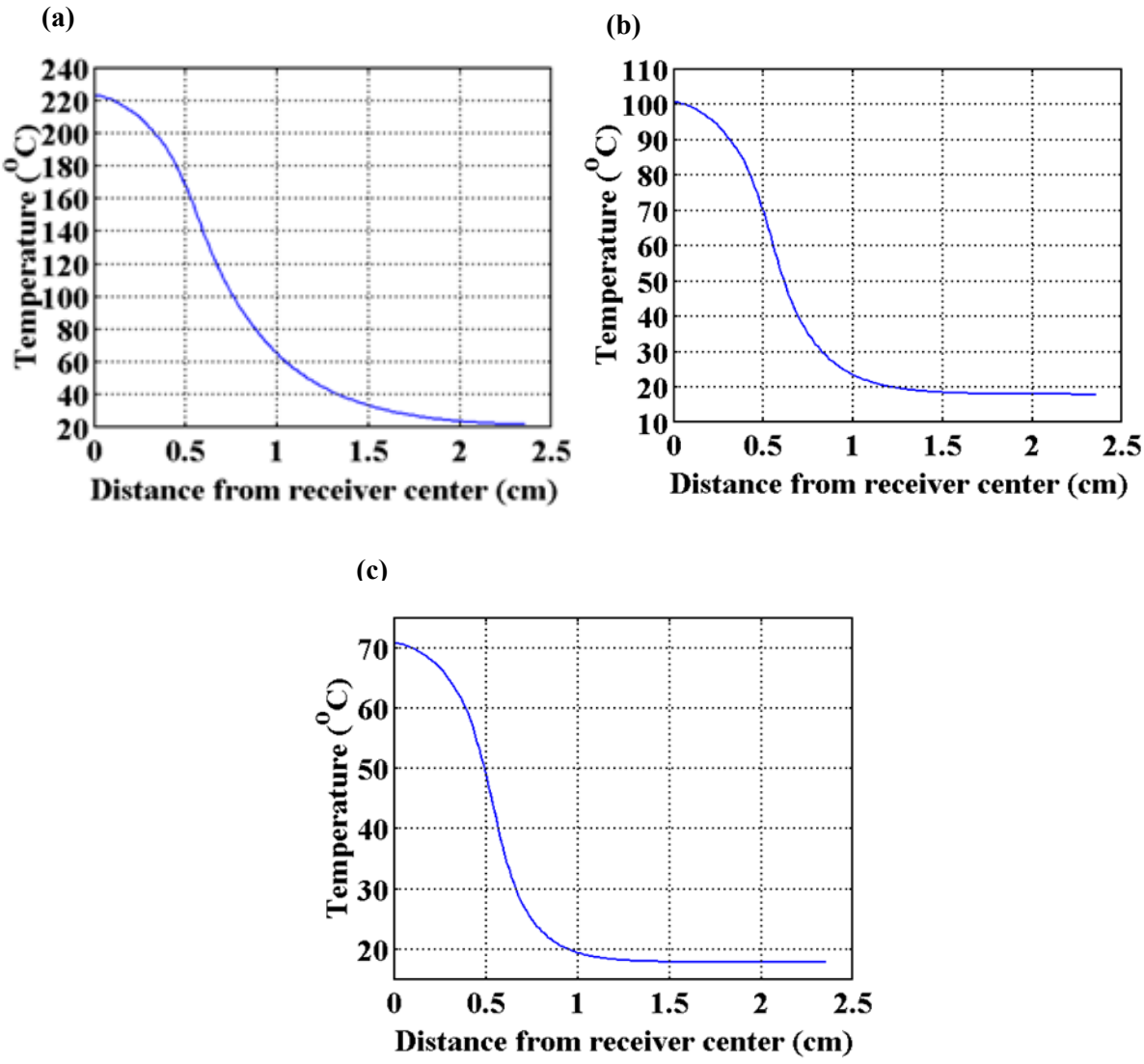

Figure 62 Temperature as a function of distance from center of a solar cell receiver with various cooling power at the bottom of the receiver (a) 1000 W/(m^2°C) (b) 5000 W/(m^2°C) (c) 10000 W/(m^2°C) for sample B receiver.

Figure 63 is the COMSOL simulated and experimental surface temperature distribution of a sample B receiver as a function of distance away from the center. The simulated cooling power of a sample B receiver was calibrated to be 4350 W/(m^2°C) and the input power was 337 suns concentration. Both experimental and simulated thermal data were averaged between the left and right side and subjected to the non-thermal paste condition. The maximum error of the two curves is ±0.5°C.

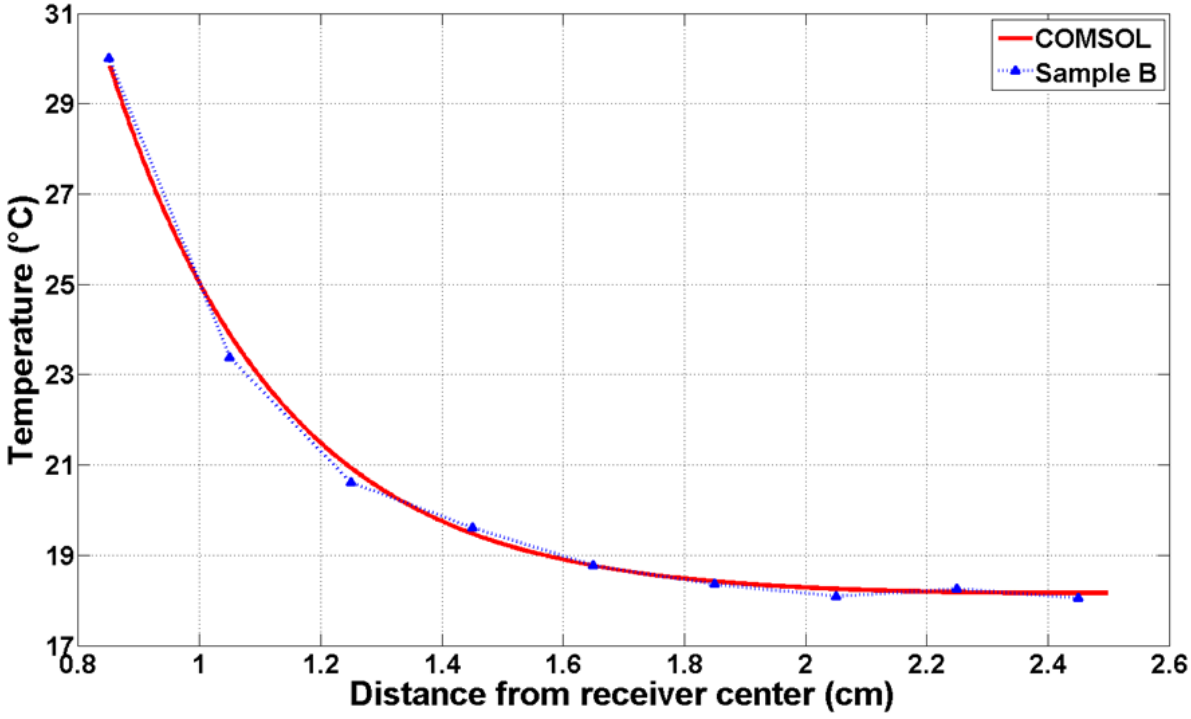

Figure 63 Surface temperature as a function of distance from the center of sample B receiver.

The calibrated value for cooling power performed by the experiments is 1940 W/(m^2°C) which is significantly lower than the surface temperature calibrated value. The discrepancy between the two calibrated values could possibly have errors originating from:

- The V_{oc} and change in cell temperature are based on the general coefficient of -4.3 (mV/°C) which is an averaged from 1 to 2000 sun concentration [51]. In the specific case of 337 sun concentration, the coefficient is ~-4.7 (mV/°C) [51]. Based on the new coefficient, the new cooling power obtained by the cell temperature calibration method shall increase which brings the new cooling power closer to temperature calibrated cooling power.
- The cooling power calibrated by the surface temperature method is based on experimental probing where the thermal probes are horizontally taped on a specific spot on the receiver for temperature readings. A calibrated thermometer can truly reflect the temperature of a substance given the probe is fully encapsulated by the

test substance. In the case of horizontal taped thermal probing, where there were not full contacts between probes and the surface, the temperature results can be assumed to be lower than actual. Hence the calibrated cooling power by surface temperature method is most probably higher than expected.

5.6. Meshing and approximation study

A mesh is a partition of a defined geometry into small units of simplex shapes. Simplex shapes such as prism, hexahedral and tetrahedral are combinations of nodes, faces and vertices, these can be summarized as finite elements. Meshing geometry can be achieved by various methods where a change in the setting can impact the general global mesh density, size of simplex elements and local mesh population. After establishing a suitable geometry, COMSOL Multiphysis provides nine different predefined mesh settings for quick and easy access. The predefined geometry meshing settings begins with extremely fine and ends with extremely coarse. An extremely fine mesh setting offers the densest mesh elements and vice versa for the extremely coarse settings shown in Figure 64. Meshing begins along the boundary edges at a given distance allowance between each node. The allowance distance is determined based on a three dimensional ratio of one axis with the adjacent. Hence three infinite long slabs with a thin middle slab results in more mesh elements created within the thin slab.

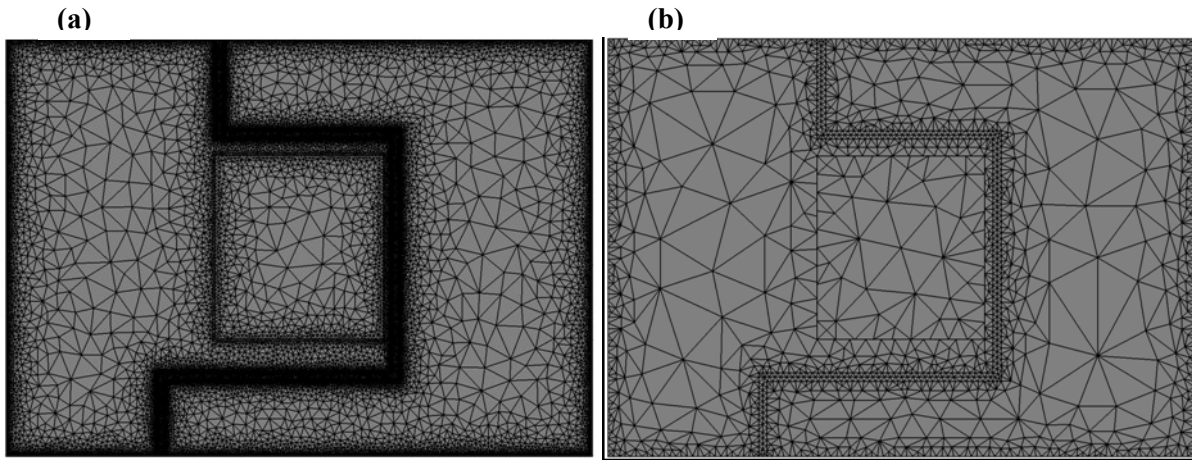

Figure 64 Predefined meshing diagram of sample C solar cell receiver with (a) finer meshing (b) extremely coarse.

Figure 65 demonstrates the number of elements and points created by various predefined mesh density options provided by COMSOL for a sample C solar cell receiver. The number of elements increases with increasing mesh density. For the interest of time saving through simulations the coarser mesh density is chosen throughout entire simulation shown by a broken orange line in the image. However no results can be obtained in the extra fine setting simulation due to physical memory shortage from the simulation computer.

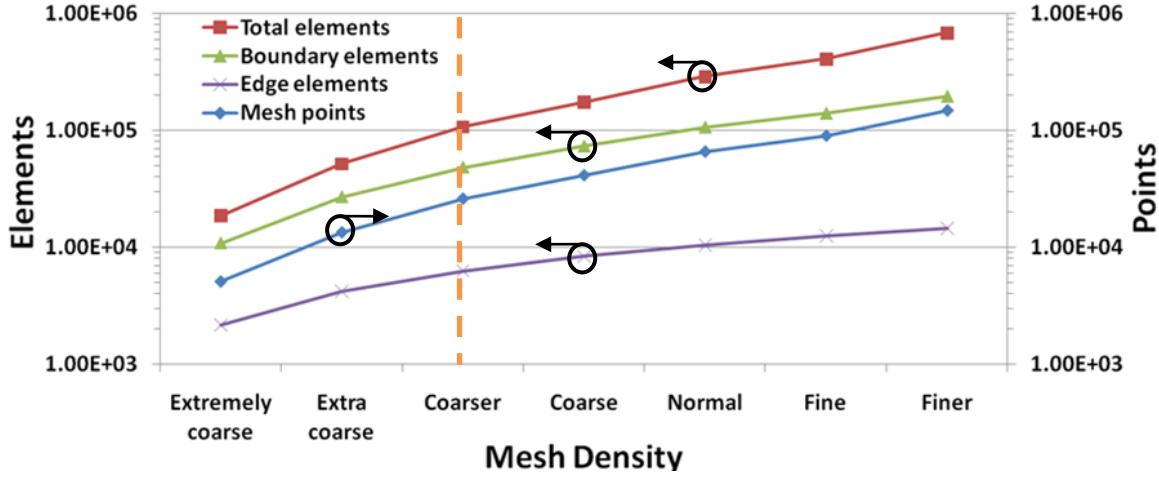

Figure 65 Elements and points as a function of various level of mesh settings. Lines between data points are guide to the eye.

Figure 66 shows the average temperature result of a COMSOL simulation of a 2 cm by 2 cm alumina carrier with copper thickness of 1.6 mm on both sides of the alumina, under 1000 sun concentration. The carrier design is a simpler downgraded version compared to the one used in Figure 65 where memory shortage can be avoided for complete simulation. With the assumption of the predefined extra fine mesh size to be the convergence point, the coarser meshing will have approximately ±0.5 °C variation contributing to error estimates and is therefore deemed sufficient for these simulations. As the mesh density increases the cell temperature decreases and the calculated cell temperature variation (temperature difference in Figure 66) tends to 0 °C. However the error is also geometry dependent where less complex geometry requires less mesh density to converge.

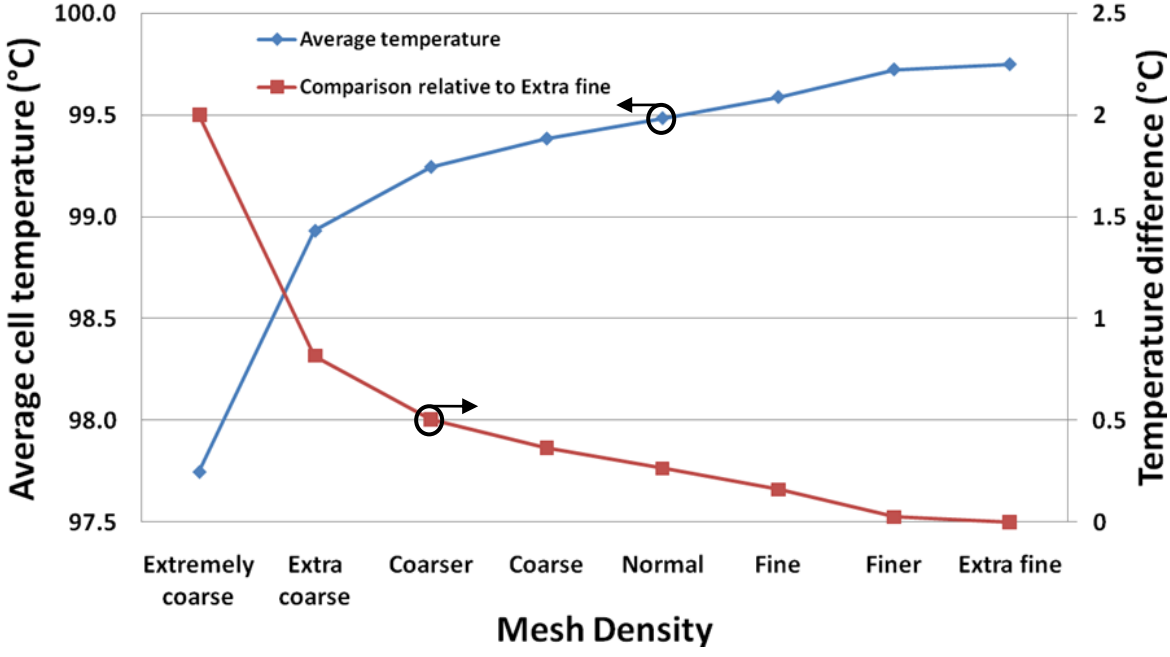

Figure 66 Simulated average solar cell temperature as a function of mesh density (blue) and temperature difference of each mesh option relative to extra fine meshing (red) of a hat channel receiver. Lines between data points are guide to the eye.

As stated earlier the finite element method is a piecewise approximation of complicated problems by partitioning the region of interest into small elements and approximating the solution of each element by a simple function. The functions used to represent the element

behaviour are approximating functions or interpolation models. COMSOL employs polynomial-type approximating functions. Polynomial interpolation functions have the advantages of known integral and differentiation methods. Secondly increasing the order of the polynomials generally improves the result accuracy when there are rapid changes in the gradient of the field variable. In higher order elements, secondary nodes within the element are introduced in addition to the primary corner nodes. The interpolation polynomial in a three dimensional COMSOL simulation begins with linear elements and progresses up to quintic element where linear element is a second order polynomial and quintic is the sixth order polynomial. A discussion on mesh refinements versus higher order elements is given by Desai and Abel [53] and motivation of using higher order element is given by Csendes in [54].

Figure 67 shows the simulated average solar cell temperature on receiver between the approximated Lagrange elements. The simulated receiver is a piece of alumina having 2.3 cm by 2.3 cm and which is 250 μm thick. On top of the alumina is the hat shape copper layer with 2 cm by 2 cm dimension and 1.6 mm in thickness. The difference in calculation between the quadratic interpolation and the linear or cubic interpolation scheme results in a 0.89°C and 0.23°C increase respectively. The linear element interpolation scheme requires less simulation time but the quadratic element interpolation scheme was chosen as it is more accurate. The cubic interpolation scheme was not used as it only improves the value accuracies by a modest amount and would have required going to a more profound computing system.

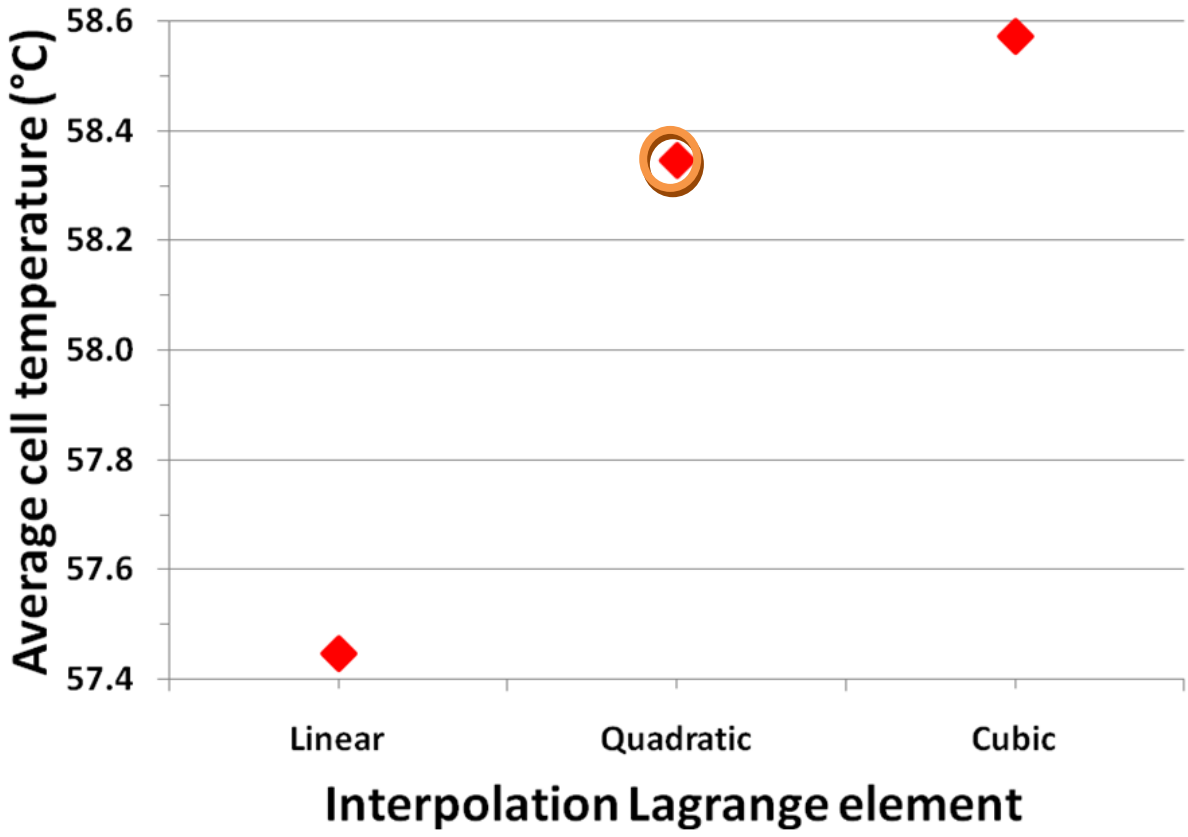

Figure 67 Average cell temperature corresponds to various type of interpolation elements. The orange circle represents the operating point in the simulation.

5.7. Simulation results

The thermal behaviour of a solar cell is mainly determined by the amount of concentration upon the surface of the solar cell and the cooling power at the bottom of the receiver. Other secondary factors including receiver geometry and material used in the receiver also contribute to the changes in cell temperature. The research here is focused on the heat spreading through the solar cell receiver where the receiver is larger than the cell size. The key to study the heat spreading effect is to observe the temperature on various receiver geometries and channel shape patterns.

The study of the concentration and cooling power relationship is tackled for a specific receiver design. This involves determining the specific amount of cooling power required to maintain a pre-determined average cell temperature under a specific concentration.

Figure 68 demonstrate the average temperature of a sample A receiver by the MATLAB-COMSOL simulation. The thermal input on the receiver begins with 100 to 2000 suns concentration and the cooling power begins with 2000 to 30000 W/(m^2 K). The operating points of a sample A receiver is indicated by coloured hollow circles. There is a linear relationship between the input power and cell temperature. As concentration increases, the cell temperature increases by the slope coefficient relative to the cooling power of the receiver.

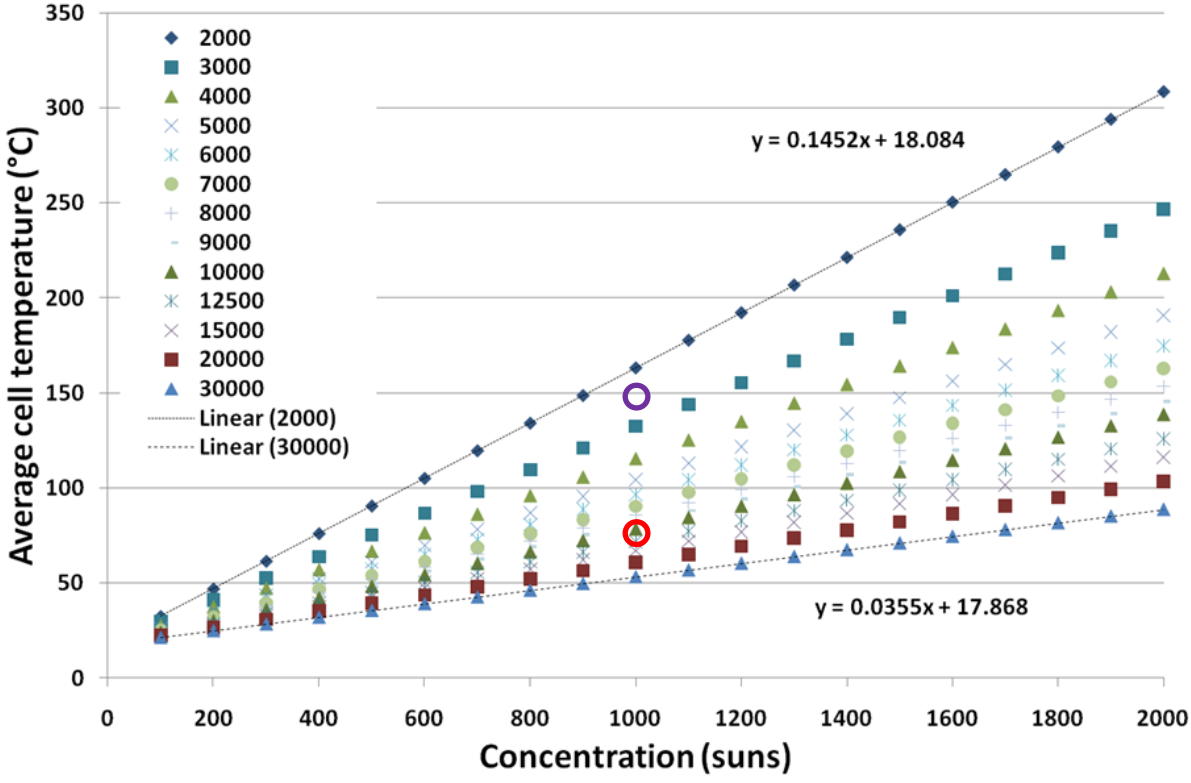

Figure 68 Averaged solar cell temperature as a function of sun concentrations with various cooling power, heat transfer coefficients, *h* (W/m^2/K), at the bottom of a solar cell receiver. The purple and red empty circles show the calibrated experimental value for sample A without thermal paste and with thermal paste, respectively.

Figure 69 shows the average cell temperature of a simulated sample A receiver under various cooling powers. Unlike the previous temperature-concentration behaviour, the temperature-cooling power relationship is not linear. The temperature-cooling power curve resembles an exponential decay line and the rate of temperature decay decreases with decreasing concentration.

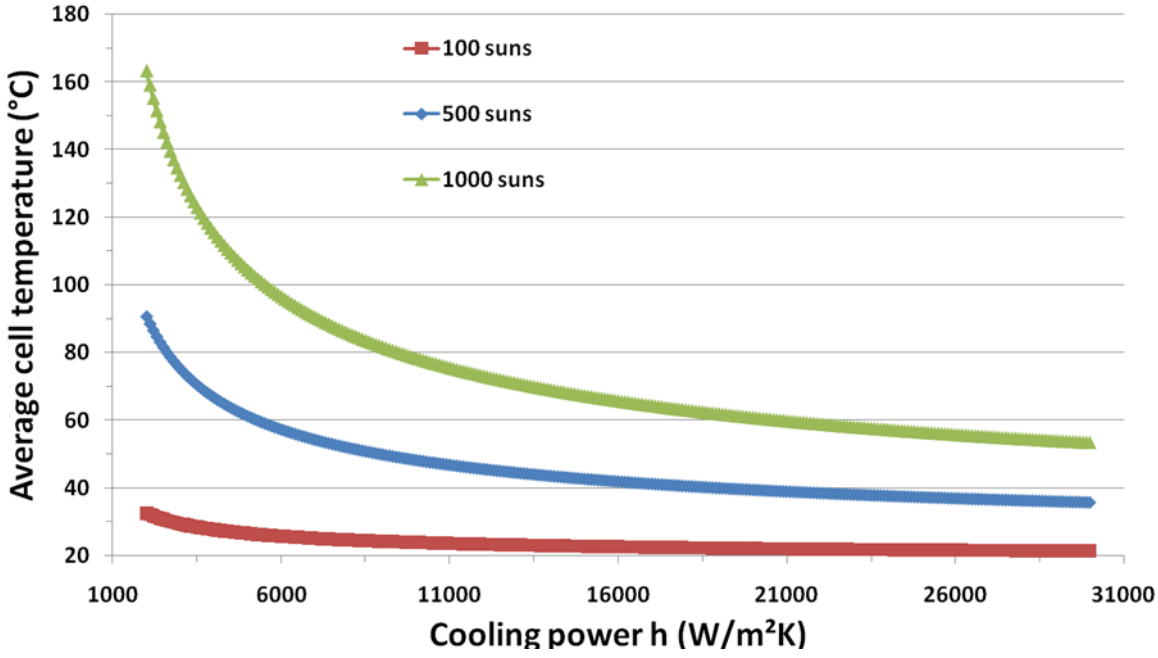

Figure 69 Average solar cell temperature as a function of cooling power with various concentrations of a simulated sample A receiver.

The geometry of a three dimensional receiver is a combination of width, length and thickness. Initially heat is created on the solar cell on the top of the receiver. Then the heat spreads along the surface of the receiver and finally flows through to the bottom of the receiver. The study of heat spreading inside a receiver can be obtained by simulations of cell temperature with variation of the receiver side length and thickness. The thermal mapping of the receiver reveals the relationship between temperature and varying receiver design parameters. The outcome of thermal mapping leads to an optimal concentrator receiver design possessing the maximum heat spreading under solar concentration.

Figure 70 is the simulated thermal mapping of a solar cell mounted on a receiver with a channel design similar to the sample A receiver. The input power upon the solar cell is 1000 sun concentrations. The receiver is composed of an alumina layer having 250 μm thickness sandwiched by a top and a bottom copper layer. The simulation range includes varying both length and width from 1.5 to 5 cm and the copper thickness from 25 μm to 2 mm. From the three dimensional thermal mapping of Figure 70, the following preliminary relationships corresponding to their numerical indicators are observed:

1. For a small receiver with length and width of 1.5 cm each and with more than 2 mm copper thickness, the resulting temperature rises linearly as the thickness of copper is further increased, or vice versa. The increase in temperature is due to longer traveling distance for the heat flux to the cooling and longer traveling distance increase the overall thermal resistance of the receiver.
2. The temperature decreases with increasing of both length and width on a receiver. The rate of temperature decrease is greater for thicker copper where a thicker receiver allows heat to spread further away from the heat source. The result of a greater heat spreading area is a lowering of the cell temperature. The advantage of heat spreading diminishes as the thickness of copper decreases due to an increase in spreading resistance.
3. There is a significant thermal improvement with increase of copper thickness prior to 4 mm with a large receiver of 5 cm on both side lengths. Adding thickness to existing 4 mm of copper increases the thermal resistance of the copper layer similar to the small receiver condition discussed in point 1 just above. However, the rate of temperature increase is not as severe due to the contributing heat spreading effect of a larger receiver.
4. Thermal results from this region can clearly demonstrate the increasing benefit of the heat spreading effect as the thickness of copper increases. However the benefit of heat spreading relies on both copper thickness and receiver size to lower the temperature. It seems increasing one variable without the other can result in no improvement or poorer performance.

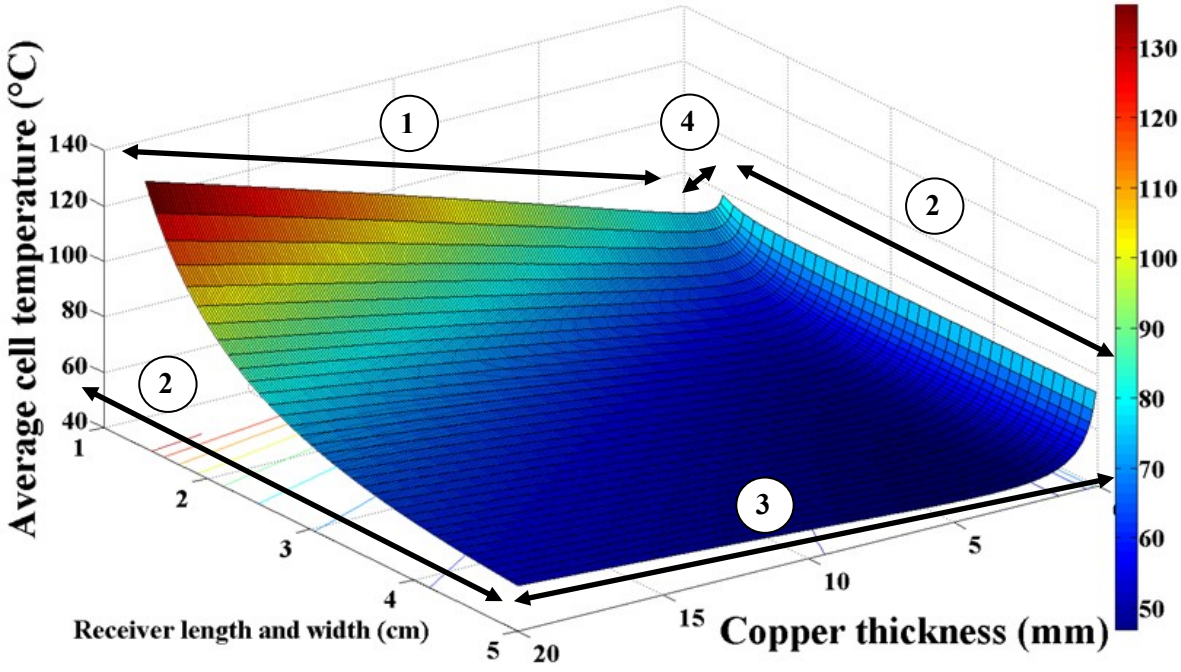

Figure 70 Average cell temperature as a function of receiver size and copper thickness. Here, the length and width have been set equal for all calculations.

A traditional concentrator receiver is composed of a minimum of two different layers. The top layer is the metallic layer which is typically made of copper. The second layer is the ceramic layer where the structural support is needed for the whole receiver. One requirement for the top layer to be metallic is to provide electrical power extraction produced by the solar cell where it is soldered on top of the metallic layer. In order to extract power from the solar cell properly the metallic layer is divided into two pieces by a channel where one for anode and the other for cathode connections. In addition the top metallic layer is also responsible for the heat transport and thermal spreading within a receiver. Ideally, a heat source should be fully encapsulated by conductive material isotropically where the encapsulation provides the most efficient thermal spreading. In the interest of thermal behaviour a study of various channel design is required.

Figure 71 is the average cell temperature for different copper thicknesses corresponding to various designs and geometry sizes. The low density broken line represents a hat channel

design similar to the sample B device and the high density broken line represents the L channel corresponding to the sample A device. The solid line is the ideal situation where a solar cell is soldered on top of a copper block without any trenches and depicted as no channel in Figure 71. The geometry sizes are simulated with 2 cm and 5 cm on both length and width. The simulation results show the ideal no-channel design has the lowest average cell temperature over all thicknesses, followed by the hat and L channel designs, respectively. The optimum design for a receiver depends on its geometry size, thickness and channel. In the interest of best cooling performance the optimum design is chosen at the lowest temperature point and shown in red empty circle. The optimum design comparison reveals the following:

- The performance of a 2 cm by 2 cm receiver shows identical optimum results for hat and L channel designs. However a 2 cm by 2 cm no channel design improves by ~7°C lower in average cell temperature compared to both L and hat channel design. A similar case for a larger receiver of 5 cm by 5 cm the improvement increases to ~11°C.
- The copper thickness increases as the geometry sizes increases. This is the requirement for the copper layer to have sufficient thickness for the heat spreading. After the optimum point the excess copper thickness becomes redundant and contributes to thermal resistance where the thermal accumulation transforms into temperature increase.

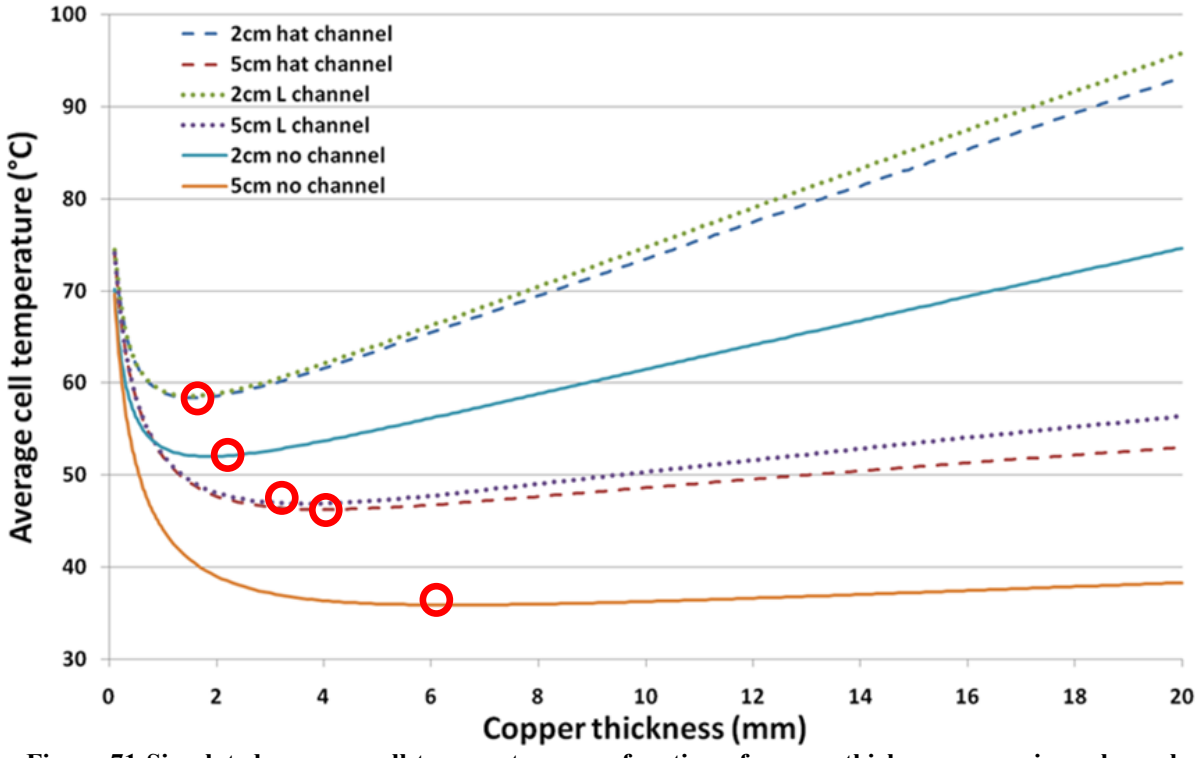

Figure 71 Simulated average cell temperature as a function of copper thickness on various channel geometry designs under 1000 suns concentration.

5.8. Conclusion

This chapter presented the COMSOL thermal simulation results based on the designs of the three experimental receivers described in chapter 4. A detailed discussion was given on the simulated receiver geometry and necessary boundary conditions for COMSOL simulations. Calibrated simulation models were used to project average cell temperature and efficiency differences from 100 to 2000 suns concentration. The relationship between the cooling power of a receiver and the input thermal power was investigated where the temperature of the cell is linearly proportional to concentration given a constant cooling power and the average temperature decay as the cooling power increases with constant concentration. A complete cell temperature thermal map of a calibrated receiver was performed. A thermal efficient receiver design must be balanced between copper thickness and side length for optimum heat spreading. The receiver channel design is another factor contributing to the cell temperature variation and as the contact surrounding area on the heat

source increases the thermal spreading also increases. As simulation convergence study on both meshing and approximation was also performed where the mesh operating point was found to be 0.5°C lower than the assumed convergence point and the approximation quadratic element was 0.2°C lower relative to the cubic approximation.

Two simulation calibrations methods were developed based on the cooling power of the sample receivers. The first method used the cell temperature and the second used the receiver surface temperature method. The two techniques give varying cooling results. This mismatch could be caused by under estimation of the temperature coefficient in the cell temperature method and lower temperature readings when thermal probing the receiver surface.

Chapter 6 Modelling of Fresnel concentrator

6.1. Introduction

In this chapter a Fresnel based concentrator system is modelled using ZEMAX ray tracing software. Through ray tracing of a generic Fresnel lens concentrating system, an increase is observed in the optical efficiency and spatial uniformity of the system using a weighted spectrum over a uniform spectrum illumination. The resultant acceptance angle of this specific concentrator is presented.

6.2. Ray tracing software

ZEMAX's Optical Design Program is a ray tracing software that integrates all of the necessary features required to conceptualize, design, optimize, analyze, and document most optical systems [55]. It is widely used worldwide in the optical industry for many applications, including lens design, light beam propagation, and freeform optical design. The numerical evaluation methods are based on Snell's law where each ray hits on interface is then evaluated in turns of reflection, transmission and absorption for that specific wavelength and the material properties of the environment. ZEMAX is capable of two types of ray tracing; sequential and non-sequential. Sequential ray tracing assumes light travels in a predefined order from surface to surface, whereas non-sequential ray tracing assumes no predefined path for any ray, for example a ray that hits a surface in its path may reflect, refract, diffract, scatter and split into rays.

6.3. Concentrator model

A solar concentrator collects light from a large area and focuses it onto a small plane. The concentrator concept and its components have been discussed in earlier sections 2.15 -

2.20. Figure 72 shows the ray tracing of a 529X, geometric, solar Fresnel concentrator designed in ZEMAX. The ray tracing initiates with a square plane source of ~23 cm^2 at the top, emitting downward normal light with spatially random distribution. The emitted light travels through a circular optical acrylic Fresnel lens of ~32.5 cm in diameter, 2 mm in thickness and 0.2 mm in groove pitch (~127 grooves per inch). Through the Fresnel lens light is focused onto a BK-7 (glass) trapezoid homogenizer with 5 centimetres in height. A virtual detector is located at the bottom end of the homogenizer for light collection and power measurements. Both the Fresnel and the homogenizer are designed to have anti-reflective coating deposited on their surfaces for maximum optical transmission.

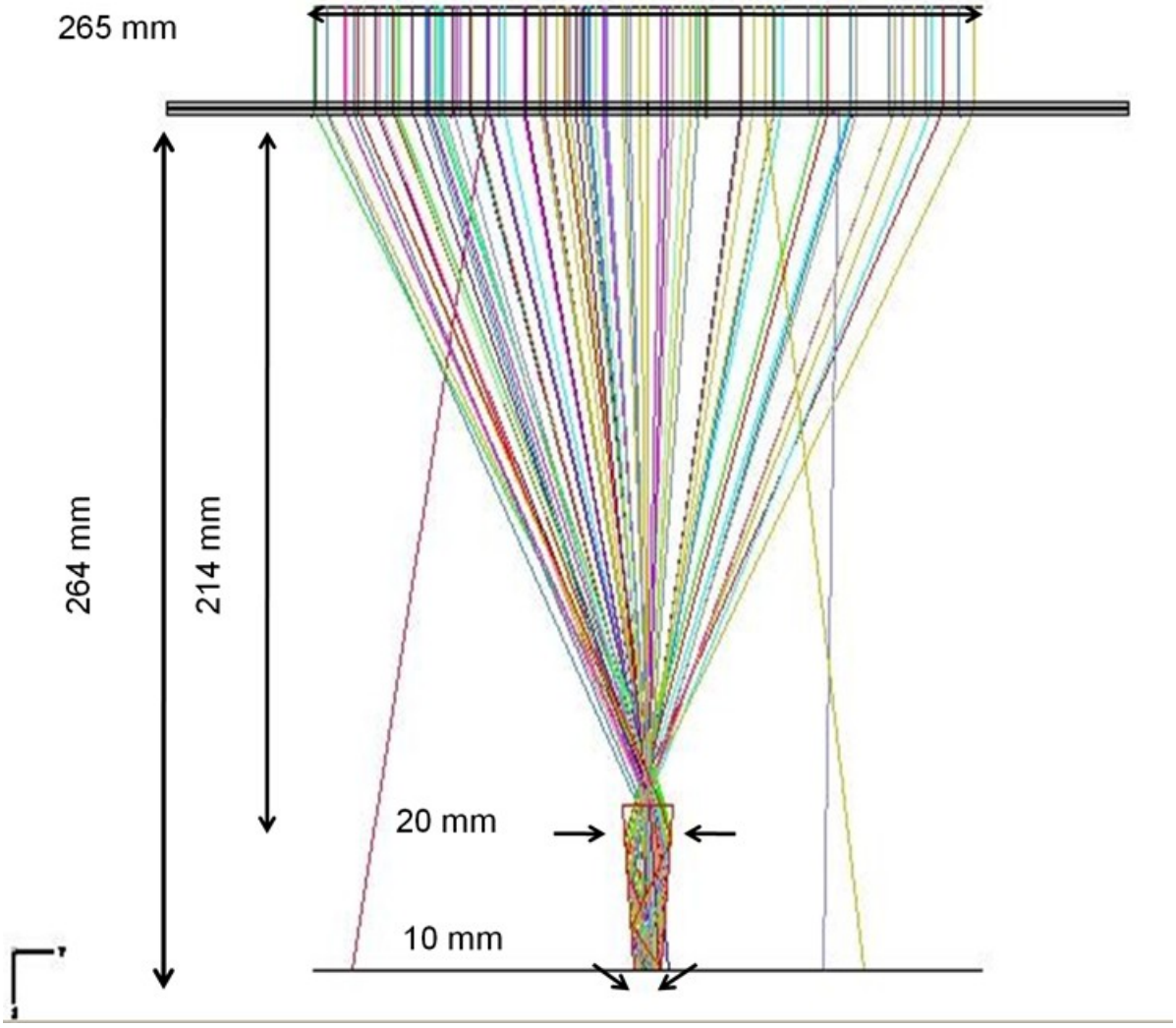

Figure 72 Ray tracing simulation of concentrator optics in side view.

The emitting spectrum in the ZEMAX simulation can be weighted specifically for each wavelength. A new radiating spectrum is created with the combination of direct normal solar irradiance and quantum efficiency of a triple junction solar cell shown in Figure 73. Sampled wavelengths are weighted over the entire new spectrum. They correspond to the total number of photons and are employed in ZEMAX.

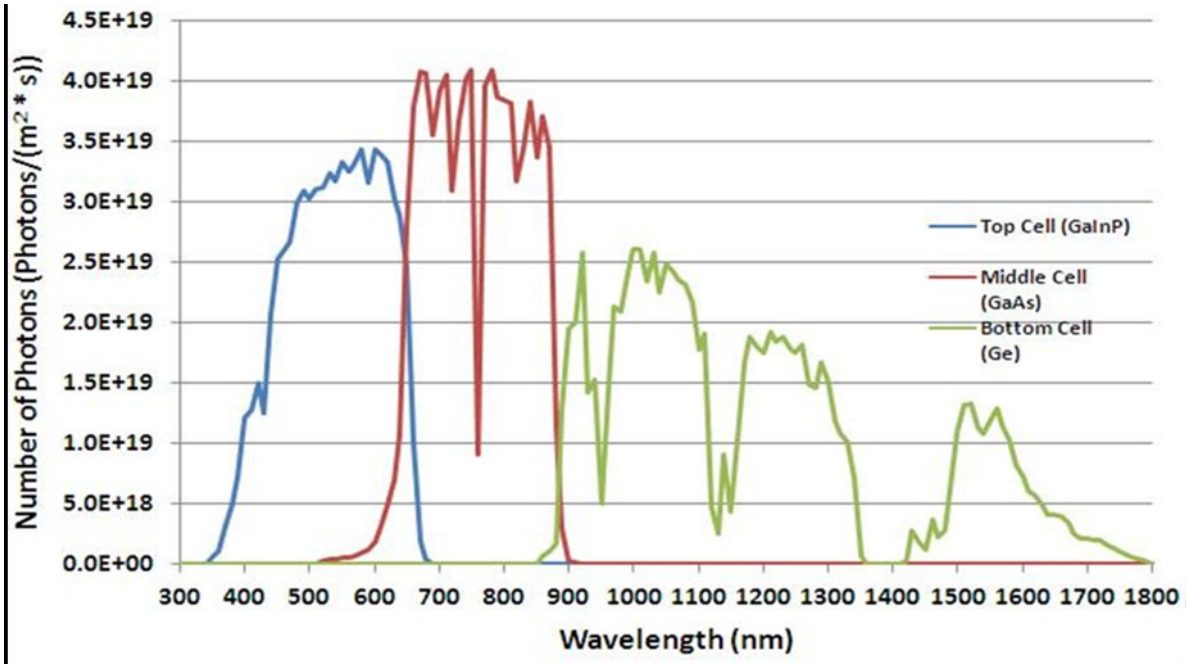

Figure 73 Quantum efficiency of each layer of the triple junction photovoltaic solar cell as a function of wavelength when illuminated by AM1.5D solar radiation. Quantum efficiency obtained from [56].

6.4. Modelling results

The simulation result in this section includes spatial distribution of light on each sub cell of a triple junction solar cell, optical efficiency of the concentrator and the acceptance angle of the concentrator.

Solar concentrator illumination uniformity on a solar cell can be revealed by the virtual detector at the bottom of the homogenizer. Both uniform and AM1.5D quantum efficiency

weighted spectrums are selected for ZEMAX simulation and comparison. The focal points for both models are optimized. The distance from the Fresnel lens, and the homogenizer are fine tuned for total maximum illumination power in the detector. Figure 74 demonstrates the spatial illumination distribution on the virtual detector for the cell and all sub cells. In the figure red represents high light intensity and blue represents low light intensity. All solar cells require as uniform illumination as possible to obtain maximum current production and avoid hot spots being created in the solar cell. The more refined modelling results using the weighted spectrum technique demonstrate a uniformity that is deemed acceptable in view that the solar cell efficiency does not vary by more than 1% over the 300-700 suns concentration range.

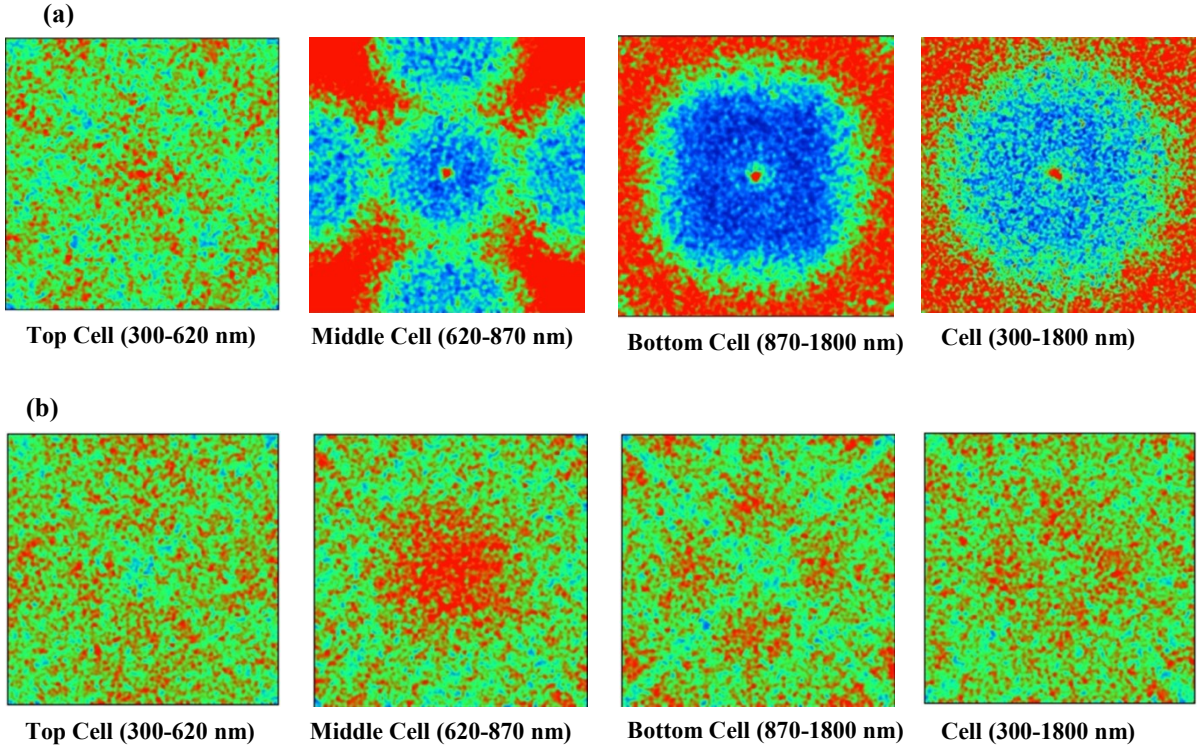

Figure 74 Spatial distribution of light within the different layers of the triple-junction photovoltaic cell. (a) uniform spectrum (b) weighted spectrum.

The optical efficiency is the total incident power on the virtual detector over the emitting power by the square source. The efficiency of each sub cell separately and the

overall cell is shown in Table 5. There is a 3% gain in optical efficiency by a weighed spectrum over the uniform spectrum where the focal length is optimized for both spectrums.

Cell / (λ range)	Efficiency (Uniform Spectrum)	Efficiency (Weighted Spectrum)
Top cell (300-620 nm)	60%	64%
Middle cell (620-870 nm)	69%	65%
Bottom cell (870-1800 nm)	57%	63%
Overall (300-1800 nm)	61%	64%

Table 5 Comparison of typical uniform concentrator optical efficiency with weighted efficiency in a Fresnel system

A Fresnel concentration system made by optical acrylic has typically a narrow acceptance angle [57]. The relationship between the acceptance angles with various Fresnel based concentrator systems were investigated in [58]. Figure 75 is the normalized irradiance as a function of the Fresnel concentrator system pointing angle and it is shown by a blue line. Under the weighted spectrum the concentrator is capable of maintaining 90% of irradiance power with 1.6 degrees from normal, as shown by the intersection of red and blue lines in Figure 75.

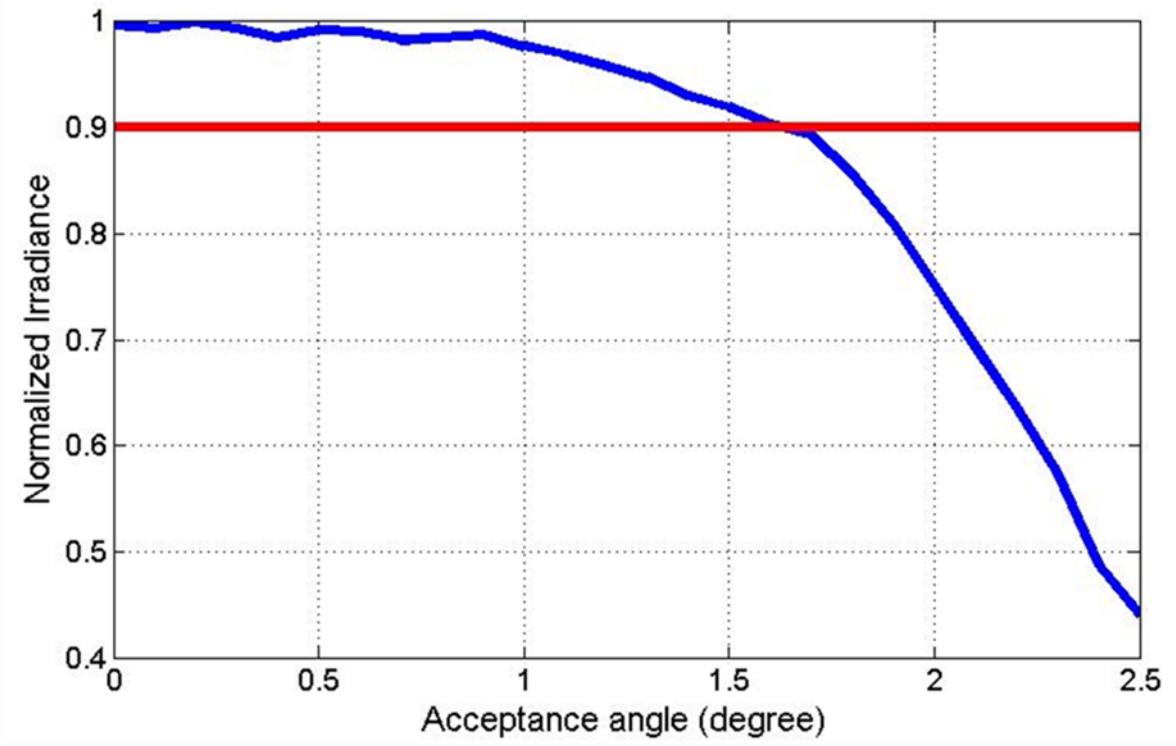

Figure 75 Normalized irradiance as a function of acceptance angle.

6.5. Conclusion

This chapter provides an overview of the modelling process of a Fresnel solar concentrator system by ZEMAX. The resultant illumination on the solar cell shows an improvement on both spatial distribution and optical efficiency using a combination weighted spectrum of quantum efficiency and DNI over a uniform spectrum. The acceptance angle was determined to be 1.6 degrees from normal for this Fresnel concentrator.

Chapter 7 Conclusions and future work

This thesis provides a background on solar energy, its emission spectrum, theory of semiconductors and solar cell operations. An introduction is given on the concentrator where focused on the Fresnel type modules and includes an explanation on the homogenizer, Fresnel lens and the receiver inside the concentrator module. The thermal behaviour of a receiver is also described analytically.

Chapter 3 offers a detailed setup on both the low and high power continuous solar simulators. This section investigates the lamp life time, spatial positioning of the cell with the illumination mask from the lamp, the spectrum of the lamp radiation and the time scale on which the cell temperature reaches equilibrium given a change of illumination. It shows a 0.5 sun/hr decrease in intensity, an allowance of 1.5 mm away from center positioning and a 10s warm up time required for the thermal equilibrium. The emission spectrum for both the Oriel and the XT solar simulator contains Xe spikes in the infrared region from 750 nm to 1000 nm. The Xe spikes potentially induce extra current produced in the middle and the bottom sub cell of a triple junction solar cell. Two methods of lamp intensity calibrations were introduced and then employed in the chapter 4 experiments. However it should be noted that neither method is perfect. There are mismatches in the lamp illumination spectrum between solar simulators, and a variation in the current density at one sun from a solar cell is observed between solar simulators at room temperature. In addition, when calibrating the XT-30 solar simulator the calibration solar cell is not temperature controlled. The temperature of the reference cell used for intensity calibration is expected to have higher operating temperature than room under continuous illumination. The symbiotic relationship between the V_{oc}, temperature and the short circuit current of a solar cell demonstrates an increase of temperature results with a slightly higher current output from the solar cell. Hence the concentration data on the XT-30 is over estimated. Both the spectrum mismatches and over estimated current density at room temperatures above ambient contributes to errors in intensity calibration. It is recommended in the future for more

accurate intensity calibration that the lamp spectrum mismatches and the open circuit voltages should be taken into account during the calibration.

Three types of receivers were experimented on in chapter 4 and the main results included the characterization of V_{oc}, efficiency as a function of concentration by both flash and continuous illumination. The temperature of the solar cell on the receiver was determined using a coefficient of -4.3 mV/°C relative to ambient temperature. However the temperature coefficient is not absolute over all concentrations where a larger coefficient is observed at lower concentration. The chosen temperature coefficient for this thesis is dedicated for ~500 suns concentration. It is recommended to have experimental test devices initially undergo temperature dependent flash testing creating a temperature coefficient profile for a large range of concentrations. This way, when using the temperature profile to determine the cell temperature under continuous illumination, results generated will be more representative of realistic conditions.

Solar receivers experimented on in chapter 4 were thermally modelled in chapter 5. Temperature results obtained in these experiments were used to calibrate the thermal coefficients employed by the simulations. A coefficient calibrated with a thermal paste coupled between the receiver and the chuck in one of the test devices shows 14500 W/(m^{2}K) whereas without the application of thermal paste generate a measurement of 2600 W/(m^{2}K). These results show a significant increase in the cooling power of the receiver with the introduction of thermal paste. It has been demonstrated in chapter 5 that the geometry of a receiver and the channel design also alters the resulting cell temperature given an identical input thermal flux. Simulation results show a for a 5 cm by 5 cm receiver with no channel design, the optimum thickness of the conductive layer is ~6mm where the optimum thickness of an identical 2 cm by 2 cm receiver is ~2 mm A thicker or thinner conductive layer on the receiver leads to higher resistance of the system since these options to either a longer flux travelling path or a lower thermal spreading capability.

Chapter 6 presents a Fresnel concentrator system module modelled by ZEMAX. Ray tracing results show a 3% gain in optical efficiency when the focal length is optimum for the quantum efficiency weighted spectrum over a focal length optimized uniform spectrum. The acceptance angle for a weighed spectrum is 1.6 degrees from normal while maintaining 90% of the irradiance power.

Current commercial CPV modules have surpassed 500 sun concentrations. Modules with thousands of solar concentration are under developing. This can be achieved by increasing the size of the Fresnel lens, or reducing the size of the concentrator cell, or a combination of both. With higher concentration on the solar cell it increases the cell temperature and the cell efficiency is reduced. This thesis offers the optimum ceramic receiver design but it is limited in terms of the receiver size and it conductive copper layer thickness. Current receiver uses alumina in the ceramic layer which has much lower thermal conductivity than copper. The alumina layer becomes the bottleneck in the receiver thermal system. The future work on receiver design should focus on the material used in the ceramic layer.

Appendix A

Application Note

Publish Date | MS-XX-XX.XX.XX-A
CMC-XXXXX-XXXXX

Scope

This application note demonstrates the use of COMSOL Multiphysics in device design and thermal simulation of a solar cell chip-on-carrier (CoC). It includes step-by-step instructions for generating the structure of a CoC device, thermal simulation of the device, the output of post processing data, and the results of a practical experiment.

The intended audiences of this document are the entrance-level COMSOL users who have basic knowledge of solar cell characterization and heat transfer, and wish to set up and model the thermal behavior of a solar cell on a carrier.

Background

Solar energy is one of the leading alternatives for green power generation. Part of the world's solar energy generation comes from solar modules that use concentration of light. Concentrator optics focus light collected over a large area onto a photovoltaic cell of much smaller area resulting in a significant material cost savings. In addition, photovoltaic efficiency increases under concentrated light. In this application, solar cells must be mounted on carriers before being installed into modules. Current state-of-the-art concentrator cells require approximately 500 suns concentration to achieve an efficiency of approximately 40%. The remaining 60% of the energy is converted into heat. If this excess thermal energy is not dissipated, there will be a significant decrease in the conversion efficiency. Therefore, excess heat must be transported through the carrier to achieve efficient cooling. Characterizing CoC solar cell devices through simulation is gaining popularity because it is faster and does not require expensive devices to be fabricated for testing. It also makes the carrier design process easier by providing detailed comparisons between new geometries and new materials. Given different material bases, COMSOL Multiphysics simulator is a finite element modeling software capable of simulating electrical, thermal, and structural characteristics of various geometrical designs.

A typical solar cell receiver requires a ceramic carrier with both electrical transport and heat transfer capability. The ceramic carrier used in this application is composed of three layers—one ceramic layer in between two metallic layers. The concentrator solar cell shown in Figure 76 is a triple-junction GaInP/InGaAs/Ge solar cell. Triple-junction solar cells are

expensive due to the cost of both materials and fabrication. A complete solar receiver with die attached concentrator cell is shown in Figure 77. The ceramic layer in this example is made of Polytetrafluoroethylene (PTFE) and is 1.27-mm thick. The two metallic layers are copper and are 35-µm thick. Other typical receiver materials are available off-the-shelf and their corresponding thermal values are shown in Table 6.

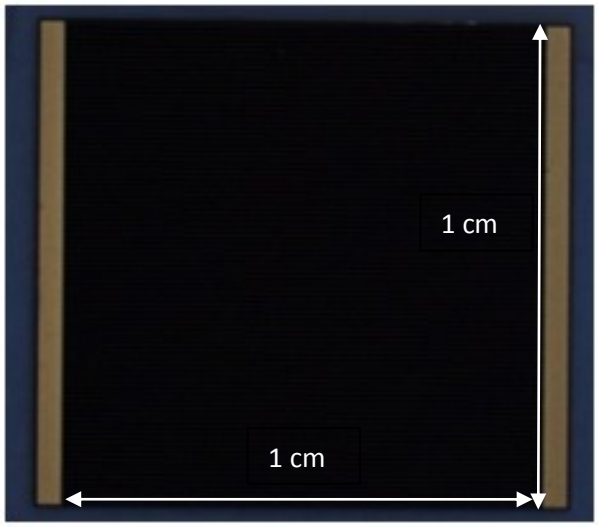

(a) Overview

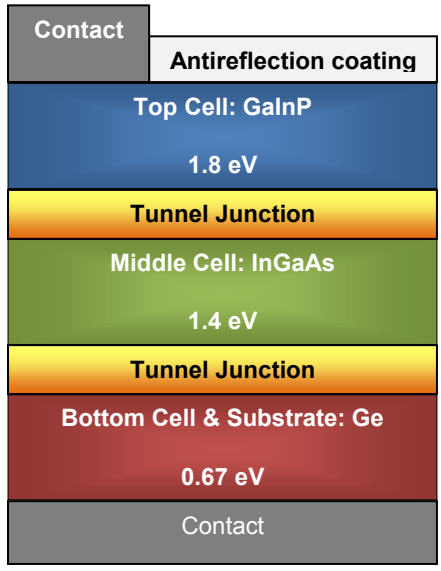

(b) Schematic with Sub-Cells Connected in Series by Tunnel Junctions

Figure 76: Bare III-V Triple Junction Solar Cell

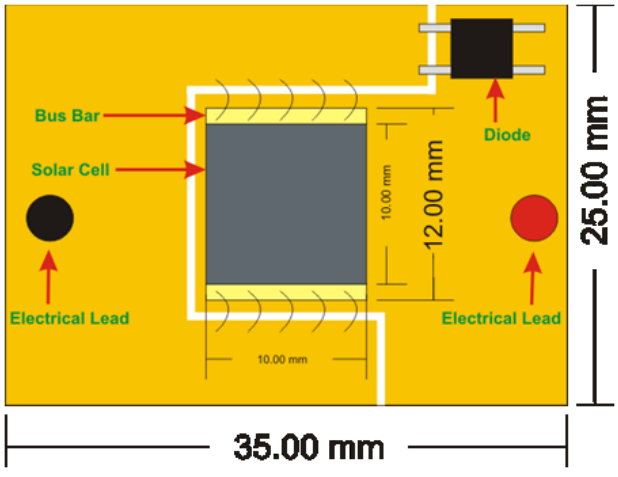

(a) Schematic of a Multi-Junction Solar Cell CoC Receiver

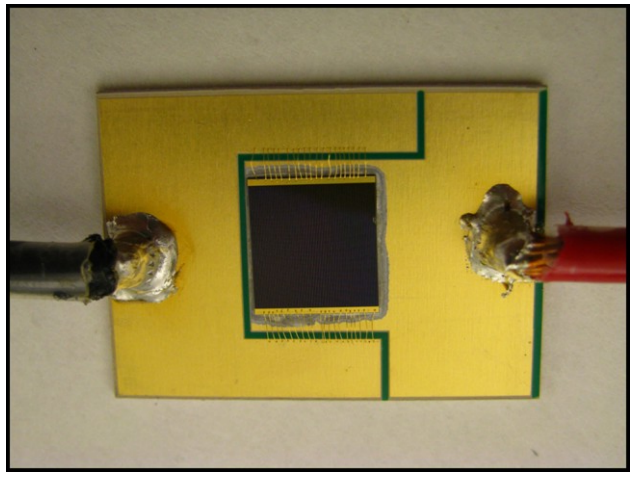

(b) Physical Receiver with No Diode Attached

Figure 77: Complete Solar Receiver with Die Attached Concentrator Cell

Table 6: Thermal Conductivity, Thermal Expansion, and Thermal Resistance for Various Materials and Their Thickness

Substrate and Thickness (µm)	Thermal Conductivity (W/cm/K)	Thermal Expansion Coefficient (K-1)	Thermal Resistance for 1 cm^2 (K/W)
Al_2O_3 (635)	0.24	7.1 * 10^-6	0.26
Al_2O_3 (250)	0.24	7.1 * 10^-6	0.11
AlN (635)	1.8	4.5 * 10^-6	0.035
BeO (635)	2.8	7 * 10^-6	0.023
Cu (30)	4	17 * 10^-6	< 0.001
Cu (100)	4	17 * 10^-6	0.0025
Cu (300)	4	17 * 10^-6	0.0075
Ag (100)	4.3	19 * 10^-6	0.0023
SnAg (100)	0.5	30 * 10^-6	0.02
SnAg (250)	0.5	30 * 10^-6	0.05

A COMSOL simulation begins with the creation of a receiver geometry and the partitioning of the geometry into finite elements. Governing equations are applied for each element and boundary conditions for the equations are those used during validation experiments. Boundary values include the ambient temperature of all faces of the receiver, thermal transfer coefficients, (i.e., the cooling power on each face), and the input intensity power on the solar cell. To properly calibrate the simulation, take the values from the actual experimental results. The measured and simulated temperature performance of similar receivers has been reported in greater detail in **Error! Reference source not found.**. owever, the receiver presented as an example in this application note has failed under high power continuous illumination and therefore the transfer coefficient *h* could not be directly determined experimentally through the current-voltage characteristic of a solar cell. Therefore, an assumption was made based on a calibrated prediction of the carrier surface temperature, which was based on the data collected with a thermocouple probe. To collect the temperature data, thermocouples were taped on the surface of the carrier away from the solar cell while under concentration. Calibrated boundary values are shown in Table 7.

Table 7: Calibrated Boundary Condition Values for a Multi-Junction Solar Cell Receiver

Boundary Face	Ambient Temperature (K)	Input Power (W/m2)	Transfer Coefficient (W/m2/K)
Cell top	303.15	280000	25
Receiver bottom	290	0	1075
Else	303.15	0	25

In this application note, COMSOL Multiphysics is used to design a solar cell CoC and the designed device is then input to a thermal simulation. The output is both plotted on screen and exported to a text file.

Description of Application

Materials Required

- Windows or UNIX equivalent workstation with minimum of 2 GB RAM
- Licensed COMSOL Multiphysics 3.3 or above

Step 1: Creating a Chip-on-Carrier Solar Cell Device Using COMSOL GUI Editor

1. From the dialog **Model Navigator**, select the tab **New**.
2. From the drop-down list **Space dimension,** select **3D**.
3. To start a new design, select **Application Modes | COMSOL Multiphysics | Heat Transfer | Conduction | Steady-state analysis**, as shown in Figure 78.

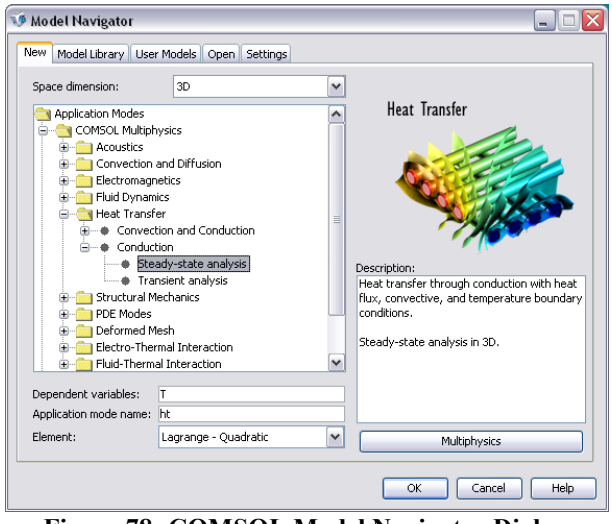

Figure 78: COMSOL Model Navigator Dialog

4. From the drop down list **Element**, select **Lagrange-Quadratic**, as shown in Figure 78.
5. From the main menu, select **Draw** | **Work Plane Settings.**
   The dialog **Work Plane Settings** appears.
6. Select the tab **Quick**, and then select plane **x-y z**, as shown in
7. Figure 79.

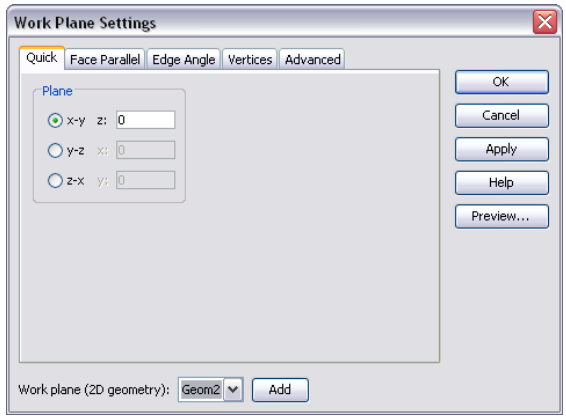

Figure 79: Work Plane Settings Dialog

8. From the main window, select the tab **Geom2** and construct device layers in 2D.
9. Click the icon **Draw Rectangle/Square** (Centered), and on the COMSOL GUI window, use the mouse to draw a random square or rectangle, as shown in Figure 80.

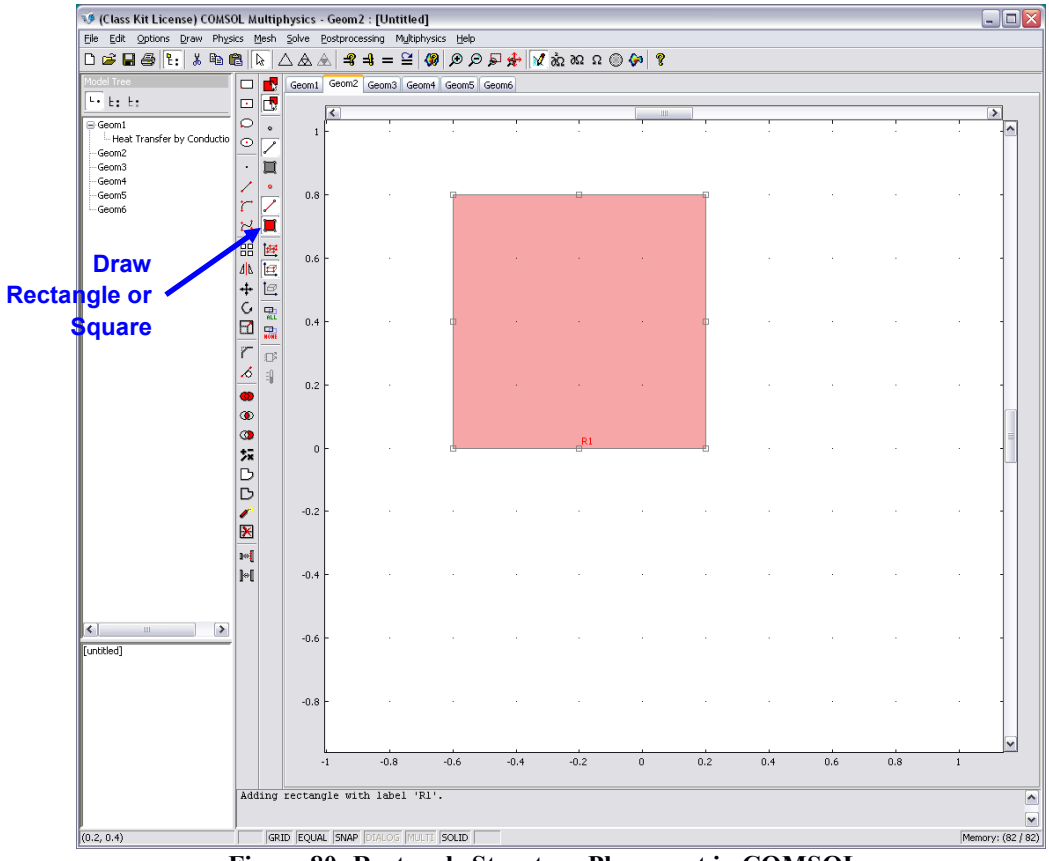

Figure 80: Rectangle Structure Placement in COMSOL

10. Double click on rectangle **R1**.
The dialog **Rectangle** appears, as shown in Figure 81.

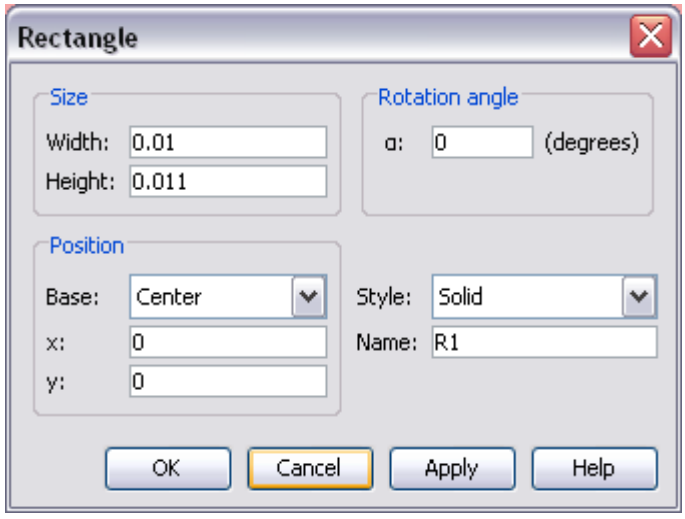

Figure 81: Rectangular Settings Dialog

11. Enter the parameter values of R1 as listed in Table 8.

Table 8: Parameters of Rectangle R1

Width	**Height**	**X:**	**Y:**
0.01	0.011	0	0

12. Repeat steps 8 to 11 for **Geom3**.
13. Create six rectangles with names from **R1** to **R6** in **Geom4** and enter the parameters as listed in Table 9 for each rectangle.

Table 9: Parameters of Rectangles R1 to R6

	Width	**Height**	**X:**	**Y:**
R1	0.035	0.025	0	0
R2	5e-4	0.006	-0.0475	0.0095
R3	0.01	5e-4	5e-4	0.00675
R4	5e-4	0.015	0.00575	-5e-4
R5	0.0135	5e-4	-0.00125	-0.0075
R6	5e-4	0.005	-0.00825	-0.01

14. From the main menu, select the tab **Edit** | **Select All**.

15. Select tab **Geom4,** and then from the toolbar, click the icon **Difference,** as shown in Figure 82.

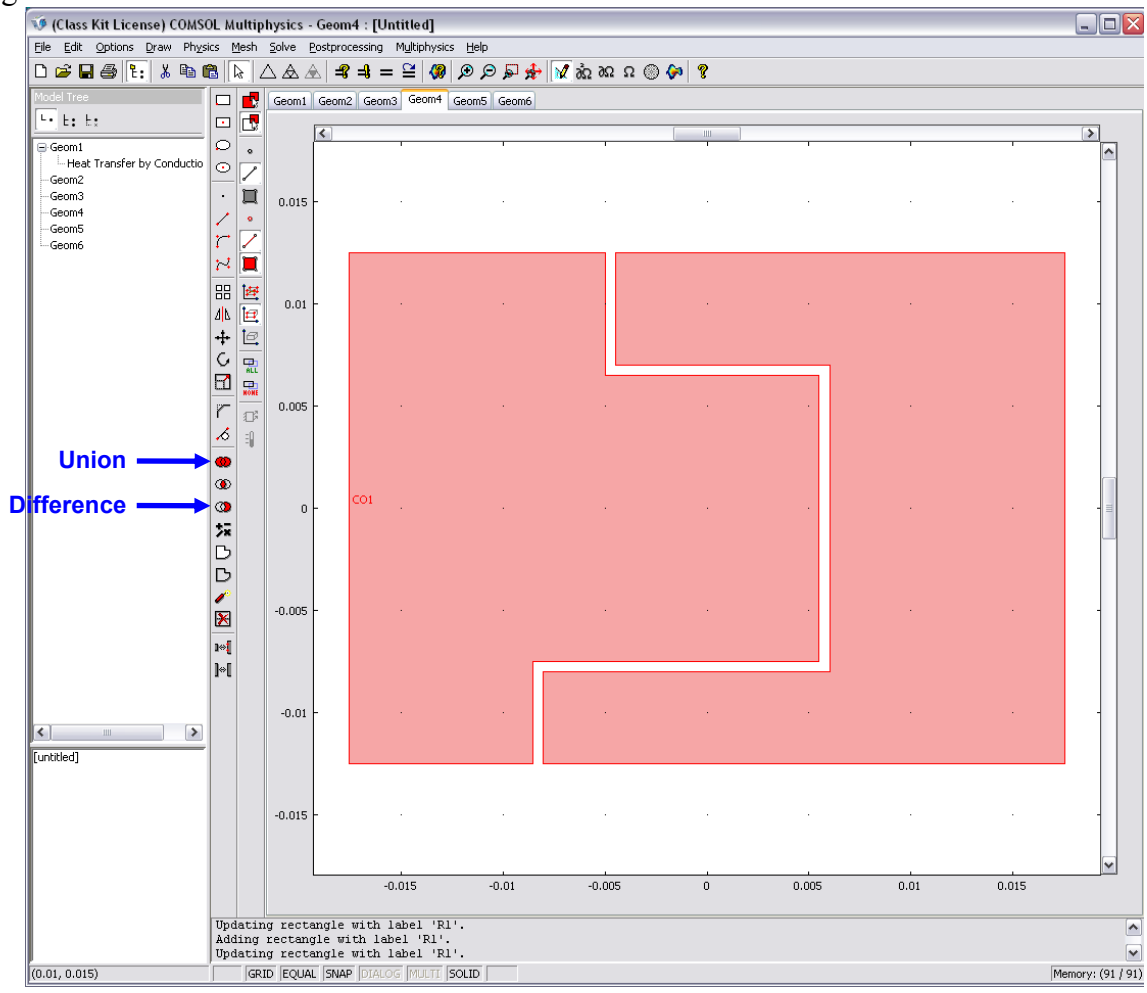

Figure 82: Geom4 Structure

16. In **Geom5**, create a rectangle with the parameters in Table 10.

Table 10: Parameters of Geom5 Rectangle

Width	**Height**	**X:**	**Y:**
0.035	0.025	0	0

17. Repeat step 16 in **Geom6.**
18. To create a 3D structure using a 2D figure, in the main window, select the tab **Geom2**.
19. Select the tab **Extrude** | **Draw**.
    The dialog **Extrude** appears, as shown in Figure 83.

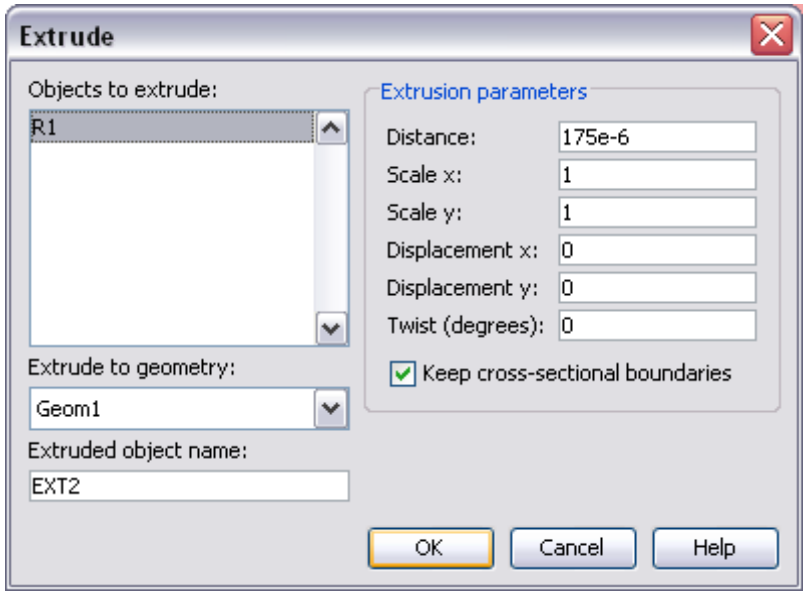

Figure 83: Extrude Dialog

20. From the text box **Distance,** enter **175e-6**, as shown in Figure 83.
21. From the in toolbar, click the icon **Move.**
    The dialog **Move** appears, as shown in Figure 84.

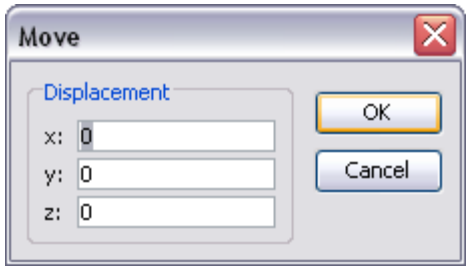

Figure 84: Moving Objects in 3D

22. From the text box **Displacement z:**, enter **0**, as shown in Figure 84.
23. Repeat steps 18 to 22 for **Geom3** to **Geom6,** and with the parameter values listed in Table 11.

Table 11: Distance and Displacement Values

Geom#	**Distance:**	**Z: Displacement**
Geom3	-100e-6	0
Geom4	-35e-6	-100e-6
Geom5	-625e-6	-135e-6
Geom6	-35e-6	-760e-6

24. To merge all extruded objects in **Geom1** into one device, from the main menu, select the tab **Edit | Select All**.
25. From the toolbar, click the icon **Union** (see Figure 82).

Step 2: Configuring Values for Subdomain and Boundary Settings

Subdomain Settings

1. From the main menu, select **Physics | Subdomain Settings**.
   The dialog **Subdomain Settings** appears, as shown in Figure 85.

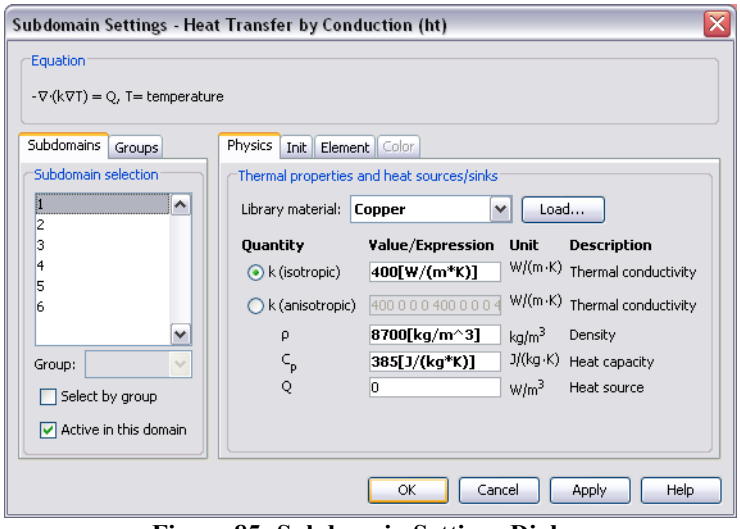

Figure 85: Subdomain Settings Dialog

2. Select the tab **Subdomains**, and then select the first subdomain **1**.
3. Select the tab **Physics**.
4. From the drop-down list **Library material,** select the material as listed in Table 12.

Table 12: Library Material Setting

Subdomain Selection Number	Library material:
1	Copper
2	PTFE
3	Copper
4	Copper
5	Solder, 60Sn-40Pb
6	Ge

5. Repeat steps 2 to 4 for the remaining subdomains.

Note: The actual solder used in the experiment was AuSn alloy. However, because it is not in the material library, SnPb solder is chosen instead, assuming similar thermal properties. The solar cell is grown on Ge substrate. The GaInP/GaAs layers account for less than one tenth of the overall substrate thickness of about 200 μm. We have thus chosen to use only Ge for the cell in the COMSOL simulation. The bottom of the cell is coated with a few microns of gold and is also neglected in the simulation.

6. Select the tab **Init**.
7. For each subdomain, from the text box **Temperature**, enter **298.15**.

Boundary Settings

1. From the main menu, select **Physics** | **Boundary Settings**.
   The dialog **Boundary Setting** appears, as shown in Figure 86.

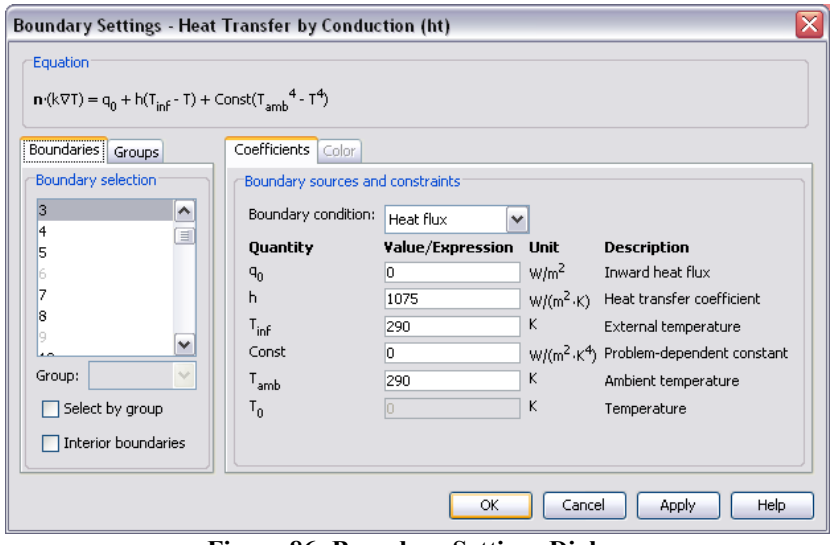

Figure 86: Boundary Settings Dialog

2. Select the tab **Boundaries**, and then select boundary number **3**.
3. Select the tab **Coefficients**.
4. Enter the coefficient values as listed in Table 13.

Table 13: Boundary Selection Coefficients

Boundary Selection number	**Boundary Condition**	**q_0**	**h**	**T_{inf}**	**Const**	**T_{amb}**	**T_0**
3	Heat flux	0	1075	290	0	290	0
29	Heat flux	280000	25	303.15	0	303.15	0
Note: **q_0** is the incident illumination power on the top surface of the solar cell in the form of heat energy; **h** is the thermal transfer power on a designated face;							

Boundary Selection number	Boundary Condition	q_0	h	T_{inf}	Const	T_{amb}	T_0
T_{inf} is the temperature external to the designated face corresponds to **h**; T_{amb} is the temperature of the correcting **Const** of a designated face; and T_0 is the initial temperature of the designated face.							

5. Repeat steps 2 to 4 for boundary number **29**.
6. Select the tab **Groups,** and then select the group **unnamed1**.
7. Select the tab **Coefficients**.
8. Enter the coefficient values as listed in Table 14.

Table 14: Group Selection Coefficients

Group Selection number	Boundary Condition	q_0	h	T_{inf}	Const	T_{amb}	T_0
(unamed1)	Heat flux	0	25	303.15	0	303.15	0

Step 3: Constructing Mesh

1. From the main menu, select **Mesh | Free Mesh Parameters**.
   The dialog **Free Mesh Parameters** appears, as shown in Figure 87.

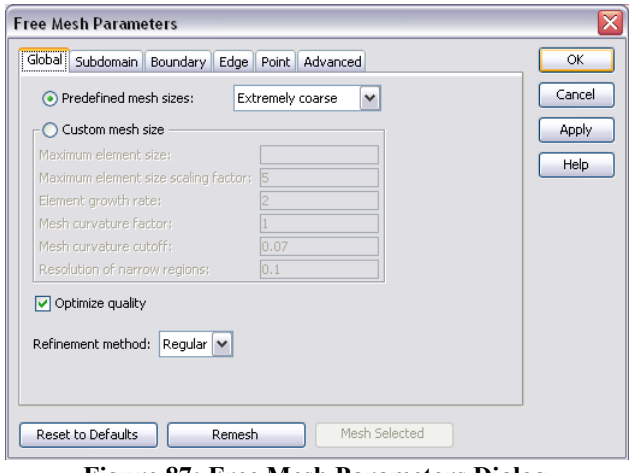

Figure 87: Free Mesh Parameters Dialog

2. From the drop-down list **Predefined mesh sizes,** select **Extremely coarse**.
3. From the drop-down list **Refinement method,** select **Regular**.
4. Select the tab **Advanced**.
5. From the text box **Resolution to geometry,** enter **1**.
6. From the main menu, click the icon **Initialize Mesh**, then click the icon **Refine Mesh**.

Step 4: Solving

1. From the main menu, select **Solve | Solver Parameters**.
   The dialog **Solver Parameters** appears, as shown in Figure 88.

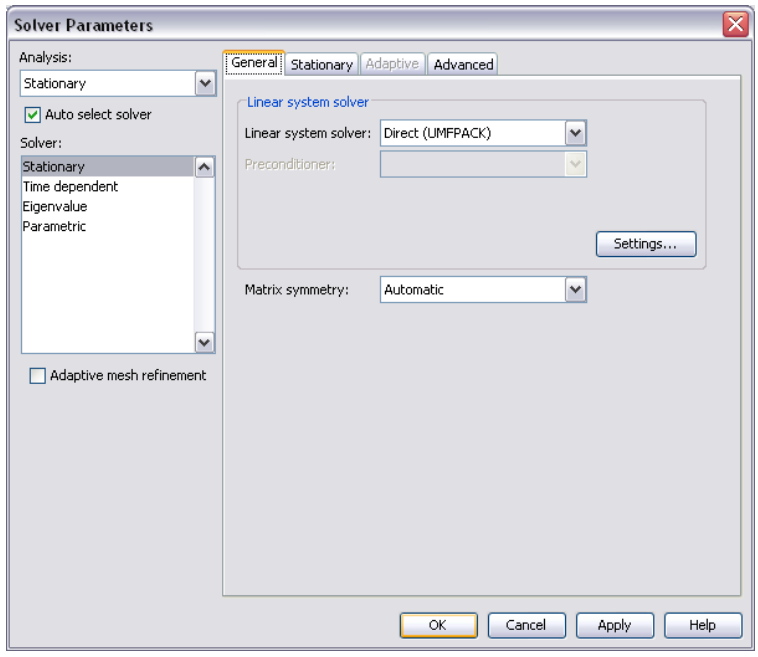

Figure 88: Solver Parameter Dialog

2. From the drop down list **Linear system solver,** select **Direct (UMFPACK)**.
3. From the main menu, select the tab **Solve**.
   The results are displayed, as shown in Figure 89.

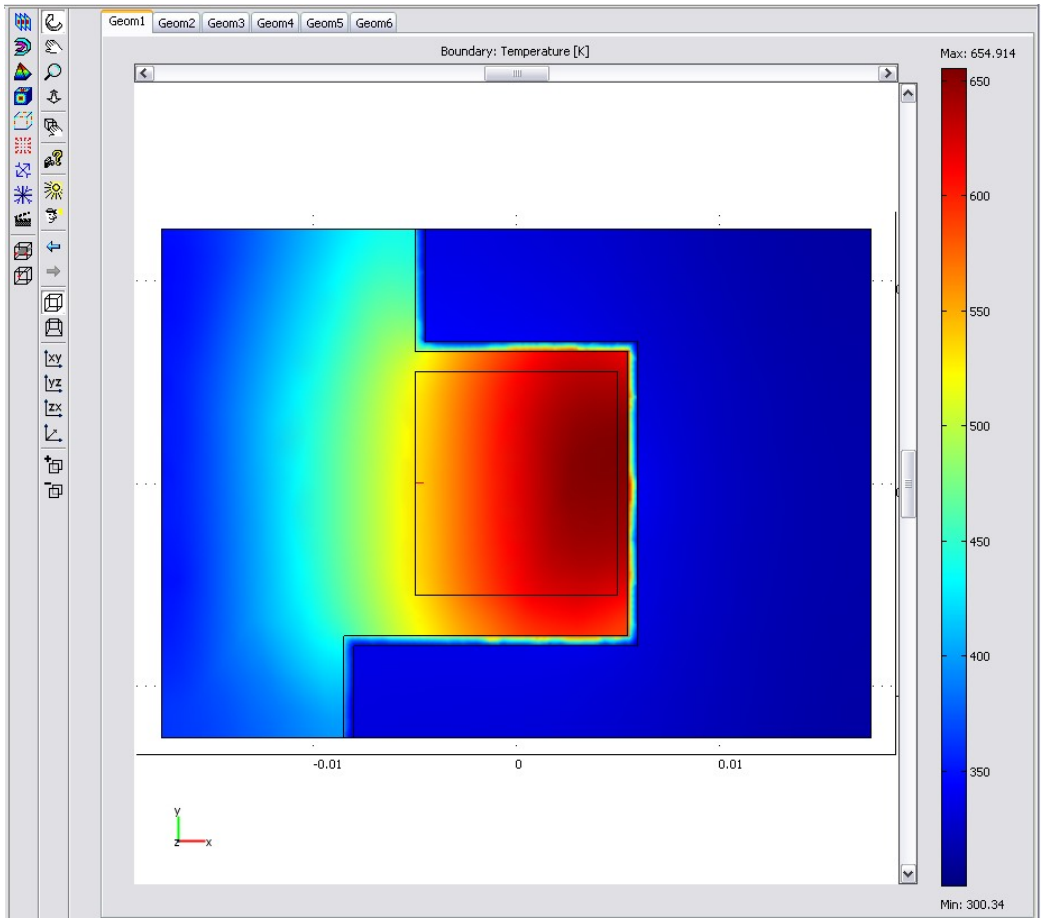

Figure 89: Thermal Simulation Boundary Results under 280 Suns Concentrations

Step 5: Postprocessing

Slice Plot

1. From the main menu, select **Postprocessing | Cross-Section Plot Parameters**.
2. Select the tab **Line/Extrusion**.
   A dialog appears.
3. From the drop down list **Predefined quantities**, select **x-coordinate**.
4. From the drop down list **Unit**, select **mm.**
5. From the section **x-axis data**, click the icon **Expression**.
6. From the section **Cross-section line data**, enter the parameters listed in Table 15.

Table 15: Parameters of Cross-Section Line

x0	x1	y0	y1	z0	z1
-0.005	0.005	0	0	175e-6	175e-6

7. Click **Apply**.

Results are plotted, as shown in Figure 90.

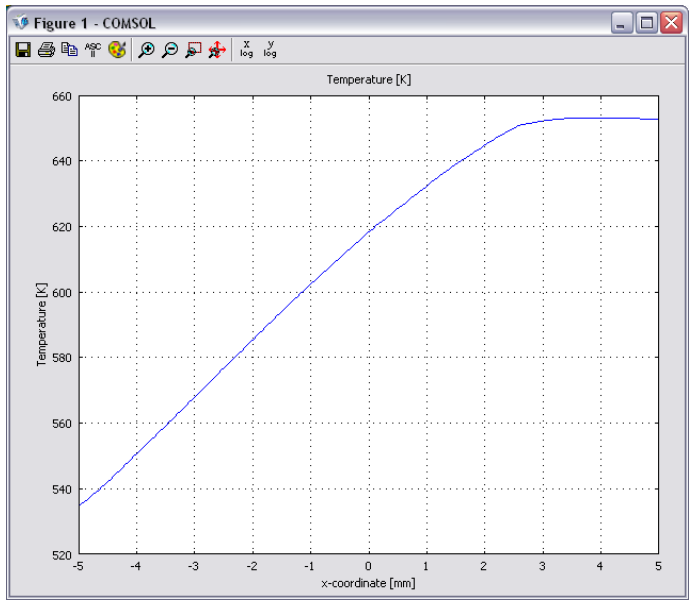

Figure 90: Cross Section Temperature Plot of the Solar Cell Device

Exporting Simulation Data

1. From the main menu, select **File | Export | Postprocessing Data**.
   The dialog **Export Postprocessing Data** appears, as shown in Figure 91.

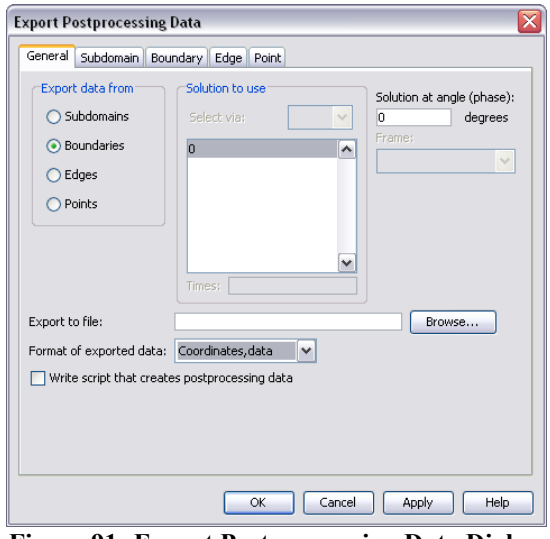

Figure 91: Export Post-processing Data Dialog

2. From the section **Export data from,** select **Boundaries**.

3. From the drop down list **Format of exported data**, select **Coordinates**, **data**.
4. From the text box **Export to file**, enter a file name.
5. Click **OK**.
   The postprocessing data is exported.

Results and Discussions

The experimental results demonstrated that the test receiver could not survive high intensity illumination under a continuous power solar simulator. The concentration on the solar cell was approximately 300 suns. The solar cell mounted on top of the carrier was almost incinerated (see Figure 92) due to the lack of thermal conduction through the carrier. Low thermal spreading on the copper layer and high thermal resistance of the PTFE layer were suspected to be the cause of the high temperatures. In addition it was possible that physical voids or bubbles might be caught in the solder layer cell mounting process. When the cell was under illumination, a void or a bubble did not allow conduction of heat through the carrier thus trapping excess heat. With enough thermal accumulation, the hot spot melted resulting in the failure of the cell.

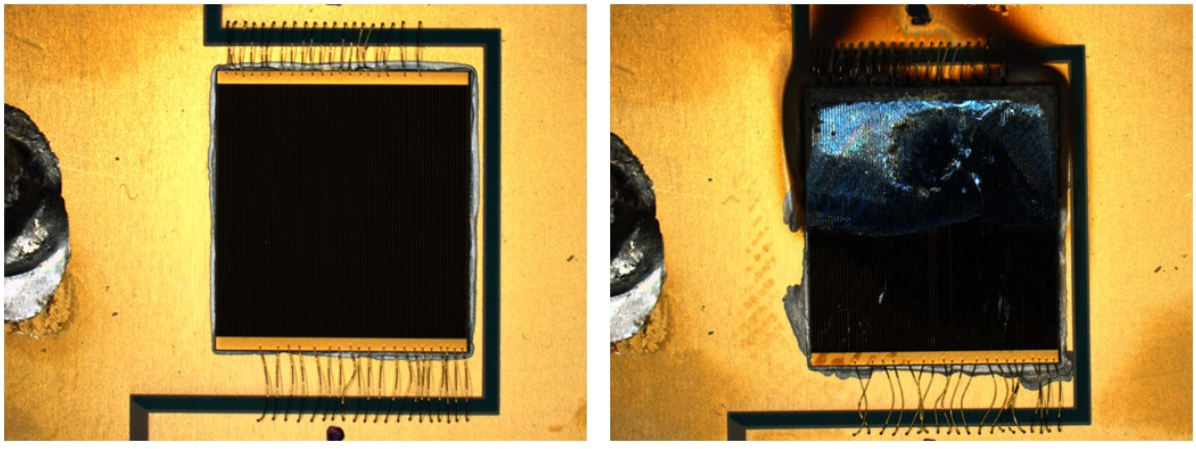

(a) Before **(b) After Continuous High Solar Illumination**

Figure 92: A Receiver

Thermal simulation results show that the maximum temperature on the receiver is 655K with 280 suns concentration as shown in Figure 89. Typical solder melting temperatures range from 363K to 723K so the type of solder must be considered carefully. In addition, the temperature distribution is thermally higher on the left side than the right side. The difference is caused by the heat spreading that takes place only on the left side. There is no heat spreading on the right side because of the trench. Heat spreading helps to cool down the solar cell temperature by transporting the heat flux away from the cell laterally and then

through the carrier over a larger area. The effect of heat spreading on a receiver is an ongoing investigation.

Conclusion

This application note presents the design and thermal simulation of a CoC solar cell using COMSOL Multiphysics simulator. The experimental results show that the receiver is inoperable under high concentration; and simulation results demonstrate that the heat spreads on a receiver while under concentration. In addition, simulation results show that the solar cell temperature is about 650K, which is within the range of the solders melting point. It confirms the possibility of the incineration of the receiver under similar concentration.

The calibrated h for the receiver used in this application is determined to be 1075 $W/m^2/K$ by temperature probing on the surface of the receiver. A more accurate calibration method is determined by the current-voltage characteristic of the solar cell on the receiver shown in [1]. The surface temperature probing method on the receiver may not truly reflect the h used in this application.

Appendix Reference

[1] S. Chow, C. E. Valdivia, J. F. Wheeldon, R. Ares, O. J. Arenas, V. Aimez, D. McMeekin, S. Fafard, and K. Hinzer, "Thermal test and simulation of alumina receiver with high efficiency multi-junction solar cell for concentrator systems", *to appear in SPIE Proceedings of Photonics North,* 2010.

Reference

[1] F. Dimroth and S. Kurtz, "High-efficiency multijunction solar cells", *MRS Bulletin-Material Rresearch Society*, vol. 32, pp. 230-235, 2007.

[2] K. Butti and J. Perlin, *A Golden Thread: 2500 Years of Solar Architecture and Technology*, Van Nostrand Reinhold, pp. 68, 1981.

[3] http://www.energylan.sandia.gov/sunlab/overview.htm, SunLab – NREL/Sandia, [retrieved Jan. 2010].

[4] W. Stolte, *Engineering and Economic Evaluation of Central-Station Photovoltaic Power Plants*, TR-101255, Electric Power Research Institute, Palo Alto, CA, 1992.

[5] F.L. McDonnel, "High power density photovoltaics", *Renewable Energy World*, September-October, 2002.

[6] http://photovoltaics.sandia.gov/docs/PVFarraysConcentrator_Collectors.htm, Photovoltaic Systems Tesearch & Development, Sandia National Laboratories, [retrieved Aug. 2009].

[7] V.M. Andreev, V.P. Khvostikov, V.R. Larionov, et al, "5800 suns AlGaAs/GaAs concentrator solar cells", *Technical Digest of the 11th International Photovoltaic Science and Engineering Conference*, Sapporo, Japan, pp. 147-148, 1999.

[8] C. W. Allen and A. N. Cox, *Allen's Astrophysical Quantities*, Springers, ch.14, pp. 340-351, 1999.

[9] C. Hu, and R.M. White, *Solar Cells: From Basic to Advanced Systems*, McGraw-Hill, New York, 1983.

[10] ASTM Standard E490-00a, "Standard solar constant and zero air mass solar spectral irrandiance tables", 2006.

[11] N.R.E.L. 1992. American Society for Testing and Material Reference Spectra for Photovoltaic Performance Evaluation (ISO 9845-1) [Online]. Available: http://rredc.nrel.gov/solar/spectra/am1.5/ASTMG173/ASTMG173.html.

[12] M. Green, *Solar Cells: Operating Principles, Technology, and System Applications,* Prentice Hall, Englewood Cliffs, NJ, ch.1, pp. 1-12, 1982.

[13] S. M. Sze and K. N. Kwok, *Physics of Semiconductor Devices*, 3rd ed. NJ, Wiley, pp. 8-12, 2007.

[14] J. F. Gibbons, *Semiconductor Electronics*, McGraw-Hill, pp. 51-54, 1966.

[15] J. Nkanta, "Characterization and simulation of long wavelength InAlGaAs/InP laser", M.S. thesis, Dept System Science, University of Ottawa, Ottawa, ON, pp. 7-8, 2008.

[16] W.H. Strehlow and E. L. Cook, "Compilation of energy band gaps in elemental and binary compound semiconductors and insulators", J Phys Chem Ref Data, vol. 2, pp. 163-199, 1973.

[17] R. J. Komp, *Practical Photovoltaics: Electricity from Solar Cells*, 2nd ed. Aatec, pp. 11-13, 2002.

[18] S. R. Wenham, M. A. Green, M. E. Watt, et al, *Applied Photovoltaics*, ch. 2, pp. 38-40, 2007.

[19] J. Nelson, *The Physics of Solar Cells, Imperial College Press*, pp. 9-12, 2009.

[20] http://pvcdrom.pveducation.org/index.html, [retrived Feb 2010].

[21] W. Shockley and H. J. Queisser, "Detailed balance Limit of efficiency of p-n junction solar cells", *Journal of Applied Physics,* vol. 32, pp. 510-519, 1961.

[22] G. Arbez, J.Wheeldon, A. Walker and et al, "Modeling and simulation of triple junction solar cells", *Proc Spie*, pp. 7750-775032, 2010.

[23] P.R. Sharps, M.A. Stan, D.J. Aiken, et al, "High efficiency multi-junction solar cells: past, present and future", *Proc 19th European Photovoltaic Solar Energy Conference*, Paris, France, pp. 3569-3574, 2004.

[24] A. Luque and S. Hedgedus, *Handbook of Photovoltaic Science and Engineering,* pp. 449-450, 453-454, 485-487, 2006.

[25] D.M. Murphy, M.I. Eskenazi, "SCARLET: design of the Fresnel concentrator array for new millennium deep space1", *Proc. 26th IEEE Photovoltaic Specialists Conf*., Anaheim, CA, pp. 861-864, 1997.

[26] B. Todorof, "A 450 suns concentrator module design", *Proc. 20th IEEE Photovoltaic Specialist Conference*, Las Vegas, NV, pp. 1347-1352, 1988.

[27] S.R. Kurtz, "Estimating and controlling chromatic aberration losses for two-terminal devices in refractive concentrator systems", *26th IEEE PVSC*, pp. 361-364, 1996.

[28] M. J. O'Neill, "Line-focus optics for multi-junction cells in space power arrays", *26th IEEE PVSC*. pp. 349-352, 1996.

[29] L. W. James, "Effects of concentrator chromatic aberration on multi-junction cells", *25th IEEE PVSC*, vol. 2, pp. 1799-1802, 1994.

[30] K. Araki, R. Leutz, A. Akisawa, et al, "Development of a metal homogenizer for concentrator monolithic multi-junction-cells", *29th IEEE Photovoltaic Specialists Conference*, pp. 1572-1575, 2002.

[31] A. L. Luque and V. M. Andreev, *Concentrator Photovoltaics*, pp. 136-139, 2007.

[32] R.R. King, R. A. Sherif, G.S. Kinsey, et al, "Bandgap engineering in high-efficiency multijunction concentrator cells", *Proc. 2nd International Conference on Solar*

Concentrators for the Generation of Electricity of Hydrogen, Scottsdale, Arizone, May 2005.

[33] J. Nelson, *The Physics of Solar Cells, Imperial College Press*, pp. 24-28, 2009.

[34] A. Luque, A. Marti and A. J. Nozik, "Solar cells based on quantum dots: multiple exciton generation and intermediate bands", *MRS Bulletin*, vol. 32, pp. 236-241, 2007.

[35] http://nptel.iitm.ac.in/courses/Webcourse-contents/IISc-BANG/Heat%20and%20Mass%20Transfer/pdf/M2/Student_Slides_M2.pdf, [retrived Feb 2011].

[36] Y.S. Muzychka, M.M. Yovanovich and J.R. Culham, "Influence of geometry and edge cooling on thermal spreading resistance", *AIAA Journal of Thermophysics and Heat Transfer*, vol. 48, no. 15, pp. 3119-3127, 2005.

[37] C.C Lee, A.L. Palisco, Y.J. Min, "Thermal analysis of integrated circuit devices and packages", *Components, Hybrids, and Manufacturing Technology, IEEE Transactions on*, vol. 12, pp.701-709, 1989.

[38] C. Lasance, "Computer analysis of heat transfer problems to check the validity of engineering formulae", *Proc. 8th IHTC*, San Francisco, pp. 325-330, 1986.

[39] M. M. Yovanovich, Y. S. Muzychka and J.R. Culham, "Spreading resistance of isoflux rectangles and strips on compound flux channels", *Journal of Thermophysics and Heat Transfer*, vol. 13, no. 4, pp. 495-500.

[40] J. R. Culham and M. M. Yovanovich, "Factors affecting the calculation of effective conductivity in printed circuit boards", *Thermal and Thermal Phenomena in Electronic Systems,*pp 460-467, 1998.

[41] http://www.kohsieh.com.tw/PDF_Files/HAAKE/NeslabThermoFlex.pdf, Neslab ThermoFlex recirculating chiller operating manual.

[42] F. Nagamine, R. Shimokawa, M. Suzuki, et al, *Conf. Rec. IEEE Phototvoltaic Spec. Conf. 22*, pp. 1393, 1991.

[43] K. Emery, *Sol. Cells* 18, 251-260, 1986.

[44] K. Emery, D. Myers, Rummel S, "Solar simulation – problems and solutions", *Proc. 20th IEEE Photovoltaic Specialist Conf*., pp. 1087-1091, 1989.

[45] http://www.spectrolab.com, Spectrolab, 12500 Gladstone Ave, Sylmar, CA, USA, 91342.

[46] J. F. Wheeldon, C. E. Valdivia, D. Masson, et al, "High-efficiency commercial grade 1 cm^2 AlGaInP/GaAs/Ge solar cells with embedded InAs quantum dots for concentrator demonstration system", *SPIE Proceedings of Photonics North,* vol. 7750, pp. 77502Q-1 – 77502Q-9.

[47] H. B. Serreze, "Optimising solar cell performance by simultaneous consideration of grid pattern design and interconnect configurations", *Proc. 13th IEEE Photovoltaic Specialists Conference*, Washington, DC, pp. 609-614, 1978.\

[48] C. E. Valdivia, S. Chow, S. Fafard and et al, "Measurement of high efficiency 1 cm^2 AlGaInP/InGaAs/Ge solar cells with embedded InAs quantum dots at up to 1000 suns continuous concentration*", 35th Photovoltaic Specialists Conference 2010*, Proc. IEEE, Honolulu, USA, June 2010.

[49] C. R. Osterwald, T. Glatfelter, J. Burdick, "Comparison of the temperature coefficients of the basic I–V parameters for various types of solar cells", *Proc. 19th IEEE PVSC*, pp. 188-193, 1987.

[50] G. S. Kinsey, P. Hebert, K. E. Barbour, et al, "Concentrator multijunction solar cell characteristics under variable intensity and temperature", *Progress in Photovoltaics Research and Applications*, vol. 16, pp. 503-508, 2008.

[51] G. S. Kinsey, P. P. Hebert, R. A. Sherif, "Operating characteristics of multijunction solar cells", *Proc 17th International Photovoltaic Science and Engineering Conf.*, vol. 93, Issues 6-7, pp 950-951, June 2009.

[52] M. N.O. Sadiku, "A simple introduction to finite element analysis of electro-magnetic problems," *IEEE trans. Educ*., vol.32, pp. 85-93, May 1989.

[53] C.S. Desai and J.F. Abel, *Introductionto the Finite Element Method: A Numerical Approach for Engineering Analysis*. New York, Van Nostrand Reinhold, 1972.

[54] M. V. K. Chari and P. P. Silvester, *Finite Element for Electrical and Magnetic Field Problems*. Chichester: John Wiley, pp.237-244, 1980.

[55] http://www.zemax.com, ZEMAX Development Corporation, 2001 112th Avenue NE, Suite 202, Bellevue, WA, USA, 98004.

[56] R. R. King, "Advance in high-efficiency III-V multijunction solar cells", *Advance in OptoElectrontonics*., v.2007, pp. 29523, 2007.

[57] A. R. Kost, K. X. Liu and C Qian, "Acceptance angle and illumination uniformity for overfilled optical concentrators", *Optics for Solar Energy*, Tucson, pp. STuE3, 2010.

[58] P. Benitez, J. Minano, P. Zamora and et al, "High-performance Fresnel-based photovoltaic concentrator", *Opt. Express*, vol. 18, no. S1, pp. A25-A40, 2010.